Universität Stuttgart
Institut für Gebäudeenergetik, Thermotechnik und Energiespeicherung

Deutsches Zentrum für Luft- und Raumfahrt e.V.
in der Helmholtz-Gemeinschaft

Metal Hydrides for Hydrogen Boil-off Recovery

(Metallhydride für die Aufwertung von Boil-off Wasserstoff)

Bachelor thesis

presented by:
Eskens, Annika
Umweltschutztechnik (Environmental Engineering)
Matr.-Nr.: 3540334

Issuing date:
Friday 15th November, 2024

University of Stuttgart,
Institute for Building Energetics, Thermotechnology and Energy Storage (IGTE)

1. examiner: Prof. Dr.-Ing. Annelies Vandersickel
2. examiner: Dr.-Ing. Inga Bürger

Institute of Engineering Thermodynamics of the DLR, Stuttgart
(Deutsches Zentrum für Luft- und Raumfahrt e.V.)

Period: 01.06.2024 - 01.12.2024

Erklärung

Hiermit versichere ich, dass ich die vorliegende Arbeit selbständig verfasst und keine anderen als die angegebenen Quellen und Hilfsmittel benutzt habe, dass alle Stellen der Arbeit, die wörtlich oder sinngemäß aus anderen Quellen übernommen wurden, als solche kenntlich gemacht sind und dass die Arbeit in gleicher oder ähnlicher Form nicht Gegenstand eines anderen Prüfungsverfahrens war.

Stuttgart, den ....

Annika Eskens

Universität Stuttgart

Institut für Energiespeicherung
Pfaffenwaldring 31
70569 Stuttgart

Universität Stuttgart
Fakultät 4 ● IES ● Pfaffenwaldring 31 ● 70569 Stuttgart

Ansprechpartner/in
Frau Dr.-Ing. Inga Bürger
E-mail
Inga.buerger@dlr.de

‚Adresse des Studenten

Annika Eskens
Allmandring 24D, 21002
70569 Stuttgart

10.06.2024

Bachelorarbeit
für Frau cand. Annika Eskens

Titel:
Metal hydrides for hydrogen boil-off recovery

Aufgabenstellung

Wasserstoff gilt als vielversprechender Energieträger für die Energiewende, da er emissionsfrei verbrennt und eine hohe Energiedichte besitzt. Die Speicherung und der Transport von Wasserstoff stellen jedoch eine Herausforderung dar, insbesondere bei Verwendung von flüssigem Wasserstoff, der aufgrund seiner extrem niedrigen Temperatur (-253 °C) verdunstet und Boil-off-Gas erzeugt. Dieses Boil-off-Gas stellt einen Verlust von wertvollem Wasserstoff und ein Sicherheitsrisiko dar, da es zu einem Druckanstieg in den Lagerbehältern führen kann.

Ziel dieser Abschlussarbeit ist es, das Potenzial von Metallhydridsystemen zur Rückgewinnung von Boil-off-Gas bei der Speicherung von flüssigem Wasserstoff zu untersuchen. Dabei werden folgende Aspekte betrachtet:

1. Analyse des Boil-off-Phänomens:
    - Untersuchung der Faktoren, die die Boil-off-Rate beeinflussen (z. B. Tankgröße, Isolierung, Umgebungsbedingungen).
    - Quantifizierung der Boil-off-Verluste unter verschiedenen Bedingungen.
2. Evaluierung von Metallhydridsystemen für die Boil-off-Rückgewinnung für einen Anwendungsfall:
    - Darstellung der Funktionsweise von Metallhydridsystemen zur Wasserstoffabsorption und -desorption.
    - Auswahl geeigneter Metallhydride für die Boil-off-Rückgewinnung auf Basis ihrer thermodynamischen Eigenschaften und Sorptionskapazität.
    - Experimentelle Bestimmung der Kinetik und/oder Thermodynamik der Wasserstoffabsorption und -desorption eines ausgewählten Metallhydrids.
    - Erste Abschätzung zu Masse und Volumen eines Prototypen für den gewählten Anwendungsfall.

Änderungen, die im Verlauf der Arbeit als notwendig erscheinen sind vorbehalten; sie werden in einem Nachtrag zur Aufgabenstellung nachgereicht.

Die Arbeit wird am Institut für Technische Thermodynamik des DLR ausgeführt.

Betreuer/in: Dr.-Ing. Inga Bürger

Tag der Ausgabe: 01.06.2024

Tag der Abgabe: 01.12.2024

Arbeit abgegeben am: 15.11.2024

Mit freundlichen Grüßen

Inga Bürger

Digital signiert von Inga Bürger
DN: OU=Institut für Technische Thermodynamik, O=DLR, CN=Inga Bürger, E=inga.buerger@dlr.de
Grund: Ich bin der Verfasser dieses Dokuments
Ort:
Datum: 2024.06.12 10:25:55+02'00'
Foxit PDF Reader Version: 2024.1.0

Dr.-Ing. Inga Bürger

Abstract

When Liquid Hydrogen (LH2) is heated above its boiling point, it evaporates. This phenomenon is called boil-off, and the generated Gaseous Hydrogen (gH2) is called Boil-Off Hydrogen (BOH). Normally, it is released to the environment, resulting in economical and energy-related losses. The aim of this study is to identify sources of boil-off in real applications, to determine potential use cases for a thermal compression using Metal Hydrides (MH), and to demonstrate the corresponding concept of BOH-recovery in the lab.

The representative use case identified for this study is Long Term Storage (LTS). In LTS, BOH is released at $1.5 - 2$ bar and room temperature. However, this is too low for further utilization. Therefore, the option to compress the boil-off up to $8 - 10$ bar using a MH-reactor to enable further utilization in a fuel cell, is examined.

For the experimental demonstration $LaNi_5$ is selected as a suitable material for the given boundary conditions based on an analysis of Van't Hoff diagrams and their corresponding Pressure-Concentration-Isotherms (PCI).

Several experiments with different parameter settings show the reproducibility, possibilities, and the limits of thermal compression using metal hydrides. Pressure ratios between $2 - 6$ are reached with an available temperature range of $\Delta T = 50 - 90$ K. With $\Delta T = 90$ K a maximum pressure ratio of 6 was reached and with $\Delta T = 50$ K a ratio of 2 was possible. The dynamics of the reaction strongly depend on the distance of the measured points from the Van't Hoff equilibrium graph.

Based on the reactor and the determined LTS application, initial characteristic values were derived. Based on the lower heating value of hydrogen and a hypothetical fuel cell with 50 % efficiency, the potential waste heat utilization to drive the compression and desorption is calculated. The waste heat produced after one full desorption is 525 kJ, while the thermal energy required for $\Delta T = 70$ K is 156 kJ, which is only 30 % of the available energy. This indicates that the waste heat is sufficient to provide for the required desorption energy, enabling an efficient alternative option for BOH recovery.

Kurzfassung

Wenn flüssiger Wasserstoff (LH2) über seinen Siedepunkt erhitzt wird, verdampft er. Dieses Phänomen wird als Boil-off (Abdampfen) bezeichnet, und der dabei entstehende gasförmige Wasserstoff (gH2) wird als Boil-Off Wasserstoff (BOH) bezeichnet. Normalerweise wird er an die Umgebung abgegeben, was zu wirtschaftlichen und energiebezogenen Verlusten führt. Ziel dieser Arbeit ist es Boil-off Quellen in realen Anwendungen zu identifizieren, um potenzielle Anwendungsfälle für eine thermische Kompression mit Metallhydriden (MH) zu ermitteln, mit dem Ziel BOH zu recyclen und das entsprechende Konzept im Labor zu demonstrieren.

Der für diese Arbeit identifizierte repräsentative Anwendungsfall ist eine Langzeitspeicheranwendung (LTS). Bei LTS wird BOH bei $1,5-2$ bar und Raumtemperatur freigesetzt. Dies ist jedoch zu niedrig für weitere Verwendung. Daher wird untersucht, den Boil-off mithilfe eines MH-Reaktors auf $8-10$ bar zu komprimieren, um eine weitere Nutzung in einer Brennstoffzelle zu ermöglichen.

Basierend auf einer Analyse von Van't-Hoff-Diagrammen und den dazugehörigen Konzentrations-Druck-Isothermen (PCI) wird für die experimentelle Demonstration $LaNi_5$ als geeignetes Material für die gegebenen Randbedingungen ausgewählt.

Mehrere Experimente mit unterschiedlichen Parametereinstellungen zeigen die Reproduzierbarkeit, die Möglichkeiten und die Grenzen der thermischen Kompression mit Metallhydriden. Bei einer verfügbaren Temperaturspanne von $\Delta T = 50 - 90$ K werden Druckverhältnisse zwischen $2-6$ erreicht. Mit $\Delta T = 90$ K wurde ein maximales Druckverhältnis von 6 erreicht und mit $\Delta T = 50$ K war ein Verhältnis von 2 möglich. Die Dynamik der Reaktion hängt stark vom Abstand der eingestellten Punkte von der Van't Hoff-Gleichgewichtskurve ab.

Ausgehend vom Reaktor und der LTS-Anwendung wurden erste charakteristische Kennwerte abgeleitet. Ausgehend vom unteren Heizwert von Wasserstoff und einer hypothetischen Brennstoffzelle mit Wirkungsgrad von 50 %, wird die Abwärmenutzung zum Antrieb der Kompression und Desorption berechnet. Die nach einer vollständigen Desorption anfallende Abwärme beträgt 525 kJ, während die für $\Delta T = 70$ K benötigte thermische Energie 156 kJ beträgt, was 30 % der gesamten verfügbaren Energie entspricht. Dies deutet darauf hin, dass die Abwärme ausreicht, um die erforderliche Desorptionsenergie zu liefern, was eine effiziente und vielversprechende Alternative für BOH-Recycling darstellt.

Contents

List of Figures

List of Tables

Nomenclature

Latin Letters

Symbol	**Unit**	**Designation**
A		Frequency Factor
c_p	$\frac{\mathrm{J}}{\mathrm{mol \cdot K}}$	Specific Heat Capacity
E_a	$\frac{\mathrm{kJ}}{\mathrm{mol}}$	Activation Energy
$\Delta_{\mathrm{R}} H$	$\frac{\mathrm{J}}{\mathrm{mol \cdot K}}$	Reaction Enthalpy
k		Reaction rate coefficient
m	kg	Mass
M	$\frac{\mathrm{g}}{\mathrm{mol}}$	Molar Mass
n	mol	Amount of Substance
p	bar	Pressure
P	W	Power
Q	J	Heat
R	$\frac{\mathrm{J}}{\mathrm{mol \cdot K}}$	Ideal gas constant
$\Delta_{\mathrm{R}} S$	$\frac{\mathrm{J}}{\mathrm{K}}$	Reaction Entropy
t	s	Time
T	K	Temperature
V	m^3	Volume
$w\%$, w_t or x	% or $\frac{\mathrm{g}}{\mathrm{g}}$	Conversion rate
$\dot{m}$	$\frac{\mathrm{kg}}{\mathrm{s}}$	
$\dot{n}$	$\frac{\mathrm{mol}}{\mathrm{s}}$	
$\dot{Q}$	$\frac{\mathrm{J}}{\mathrm{s}}$	

Greek Letters

Symbol	**Unit**	**Designation**
η	%	Efficiency
ρ	$\frac{\mathrm{kg}}{\mathrm{m}^3}$	Density

Subscripts

Symbol	**Designation**
abs	Absorption
act	Activation
atm	Atmosphere
cr	Critical
des	Desorption
eq	Equilibrium
exh	Exhaust
FC	Fuell Cell
fl	Fluid
(g)	Gaseous
H_2	Hydrogen
m	Mass
max	Maximum
min	Minimum
R	Reaction
(s)	Solid
tot	Total
void	Void volume
WHE	Water-Heat-Exchanger
x	Placeholder for atom number
y	Placeholder for atom number

Abbreviations

Abbreviation	**Designation**
Abs	Absorption
Atm	Atmosphere
Aus	= Out
BOG	Boil-Off Gas
BOH	Boil-Off Hydrogen
CAPEX	Capital Expenditure
Des	Desorption
DLR	Deutsches Zentrum für Luft- und Raumfahrt (German Aerospace Centre)
DS	Druck Sensor (= pressure sensor)

Ein	= In
FC	Fuel Cell
gH2	Gaseous Hydrogen
H or H_2	Hydrogen
HV	Hand Valve
ICT	Institute for Combustion Technology
IRAS	Integrated Refrigeration And Storage
$LaNi_5$	Lanthanum Pentanickel
$LaNi_{4.75}Al_{0.25}$	Lanthanum Nickel 4.75 Aluminum 0.25
$LaNi_{4.8}Al_{0.2}$	Lanthanum Nickel 4.8 Aluminum 0.2
$LaNi_{4.85}Al_{0.15}$	Lanthanum Nickel 4.85 Aluminum 0.15
$LaNi_{4.9}Al_{0.1}$	Lanthanum Nickel 4.9 Aluminum 0.1
LHV	Lower Heating Value
LH2	Liquid Hydrogen
LTS	Long Term Storage
M	Metal
max	Maximum
MFC	Mass Flow Controller
MFM	Mass Flow Meter
MFM (Flgr)	Mass Flow Meter (Flügelrad = impeller)
MGT	Micro Gas Turbine
MH	Metal Hydride
min	Minimum
OPEX	Operating Expense
PCI	Pressure Concentration Isotherm
R	Reactor
sLH2	Subcooled Liquid Hydrogen
SOC	State Of Charge
SPS	Speicherprogrammierbare Steuerung = Programmable logic controller
T0X	Thermosensor
T1OX	Thermosensor with PT100 unit
$FeTi_xMn_y$	Titanium Iron Manganese Alloy
UI	User Interface
ÜV	Überdruckventil (= pressure relief / safety valve)
V	Valve
VP	Vacuum Pump
WHE	Water-Heat-Exchanger
WinCC	Windows Control Center
ZBO	Zero-Boil-Off

1 Introduction

1.1 Motivation

On their way to climate neutrality, countries undertake several measures to reduce greenhouse gas emissions. With its high gravimetric energy density of $120.1\frac{\mathrm{MJ}}{\mathrm{kg}}$, and carbon-free production and combustion [1], green hydrogen as an energy carrier seems promising in various fields of research as an energy system of the future, such as in mobility as an alternative fuel or industrial processes e.g., steel production or the chemical industry.

For example, Germany has appointed a National Hydrogen Council which has published the National Hydrogen Strategy presenting a plan for the handling of hydrogen until 2030. It states how green H_2 can be implemented into the German economy and promotion strategies to reach that goal [2]. However, with the value of $0.01\frac{\mathrm{MJ}}{\mathrm{m}^3}$, the specific energy density of hydrogen under ambient conditions is comparably low [1], which leads to difficulties in storage and transport due to its immense volume. To counteract that problem, hydrogen is most commonly stored in a gaseous compressed or in cryo-cooled liquid state.

Liquid hydrogen at its boiling point of 20 K has a density of $70.79\frac{\mathrm{kg}}{\mathrm{m}^3}$. Hydrogens' density in the gaseous state under normal conditions of 0 °C and 1013 mbar is $0.0899\frac{\mathrm{kg}}{\mathrm{m}^3}$ [3]. The liquid state, due to its higher density, can take up more hydrogen in less space than compressed gaseous hydrogen. However, other problems emerge from liquid storage and transport. The boiling temperature of LH2 under ambient pressure is 20 K or -253.15 °C [1]. Since no insulation is perfect, it is not possible to fully avoid heat flow into the storage vessel, which inevitably rises the temperature of the liquid, resulting in the evaporation of LH2. The evolving gaseous hydrogen has a higher volume, which leads to a rise in pressure in the vessel, with the risk of rupture when not being dealt with. This evaporated gas is called Boil-off Gas (BOG). Most commonly, the BOG is released to the environment, which is a significant loss and waste of resources, considering the economic value of hydrogen. Boil-off rates often vary around 1 %. However, studies imply that sometimes up to 15 % boil-off is lost in a day, depending on the tank size [4]. Regarding the state-of-the-art, active measurements, such as the implementation of cryo-coolers and heat exchangers, and passive methods such as insulating layers of the vessel, are already used to mitigate boil-off losses [5].

An alternative approach is to collect the boil-off gas and process it for further utilization.

This can be done by compressing or reliquefying the BOH. However, these processes are accompanied by extra costs and difficulties of implementation [5]. Another promising alternative to capture and compress hydrogen boil-off is the utilization of MH [6, 7].

Metal hydrides possess the ability to absorb hydrogen gas and store it in their metal lattice. During this process, heat is released, making it an exothermic reaction. When the heat is provided back to the hydride, hydrogen is discharged from the system, making it a reversible process. The special part about metal hydrides is, that depending on the release temperature of hydrogen, its pressure changes and vice versa [8]. Therefore, depending on the MH properties, hydrogen of various pressures and temperatures can be absorbed at low pressures and desorbed at desired elevated pressure levels for utilization in potential further applications, such as storage, buffer, purification, or recycling.

1.2 Goals

The goal of this research project is to evaluate thermal compressions using metal hydrides for re-use of BOH. Therefore, first, representative boil-off sources with their corresponding temperature and pressure boundary conditions need to be identified. Then, based on a reference case, the operation principle should be demonstrated experimentally, and finally characteristic values need to be derived, to evaluate the feasibility of the concept in future applications.

2 Fundamentals

In this chapter, two fundamentally important topics for this work are going to be presented: Boil-off hydrogen and metal hydrides. For boil-off, an introduction to the characteristics, occurrence and state-of-the-art of boil-off recovery solutions will be given. Regarding metal hydrides, the basic thermodynamic behaviour, including the fundamental thermochemical equation, the relationship between Van't Hoff diagrams and their corresponding PCIs, and the kinetics, will be introduced.

2.1 Boil-off hydrogen

With the continuous growth of the hydrogen infrastructure, the demand for LH2, is rising as well. However, when dealing with LH2, a phenomenon called boil-off has to be considered. Liquid hydrogen is stored at cryogenic temperatures of 20 K, and even though tank insulation measurements are already quite developed, heat inflow from the environment is inevitable, resulting in an increase in temperature above hydrogen's boiling point. LH2 evaporates and changes to the gaseous phase. This process is called boil-off and the corresponding gas boil-off gas or as in this case: boil-off hydrogen. When LH2 is stored in tanks, and BOH builds up, the pressure in the tank rises due to the increased volume of gaseous hydrogen, up until it becomes a safety hazard. Therefore, boil-off hydrogen, BOH, has to be vented to the environment and is considered as a loss. However, since the liquefaction of hydrogen is energy consuming, with about $13.83 \frac{\mathrm{kWh}}{\mathrm{kg_{LH2}}}$ [9], the release of the BOH, equals to economical losses and moreover, poses a safety hazard at the point of release. Therefore, methods of boil-off mitigation and capture have to be found.

2.2 BOH occurrence

Boil-off appears due to intrinsic reasons of H_2 such as ortho-para conversion, thermal stratification and self pressurization and external reasons such as heat leaks, sloshing, and flashing [10]. It occurs during every step of the hydrogen pathway, however, the severity depends on the step. The LH2 pathway by Petitpas [4] can be divided into four major steps: the liquefaction, the transport, the fuelling process, and the storage. The first three steps are depicted graphically in figure 2.1.

The first boil-off source occurs during the liquefaction process. However, this BOH can be recycled to the liquefaction plant, and can be reliquefied. Therefore, there are no vented losses during the liquefaction at the liquefaction plant. Moreover, the loss during the filling of the transportation trailer can also be reliquefied.

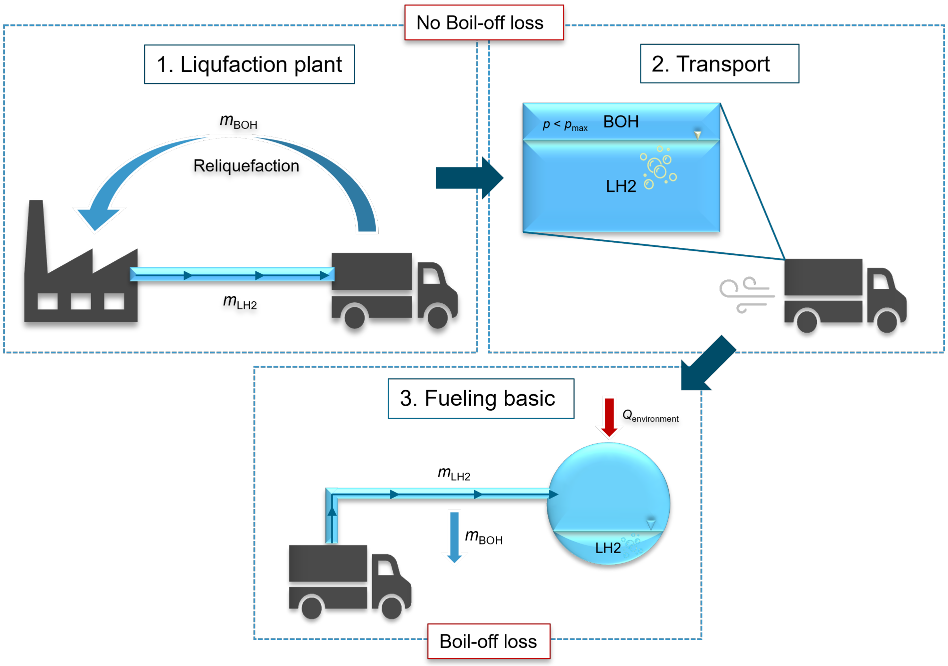

Figure 2.1: Process chain of hydrogen from the liquefaction plant until the fuelling process with boil-off sources [4]

Further boil-off also occurs during the transport. However, when considering average trailer delivery times, the pressure within the tank does not surpass the maximum pressure of the safety valve, therefore, no H_2 is vented during the delivery. However, to transport the liquid hydrogen from trailer to tank, a pressure gradient has to be established. To do so, some of the LH2 from the trailer is vaporized to increase pressure. Moreover, the BOH that was built-up during the transport can be used for that purpose as well. However, the total BOH utilized to establish the pressure gradient is counted as loss.

The most significant loss of hydrogen occurs during fuelling of the stationary tank by the trailer. According to Rosso [6] these losses are based on several reasons. Since the transfer pipes to the tank are at room temperature, they have to be pre-cooled to the temperature of liquid hydrogen, by purging them with LH2. The same applies to the inner skin of the dewar. The biggest source of boil-off during the fuelling process appears due to the flashing of the system. Flashing describes the process of inserting high-pressure LH2 into a low-pressure system, in this case the dewar. Another reason for venting, is the displacement of gaseous hydrogen with liquid hydrogen in the transfer lines and the tank, leading to a rise in pressure. BOH occurring during the fuelling process can potentially be captured [4].

In a research article concerning the Space Shuttle Program of Kennedy Space Center, estimations of LH2 losses over the range of 30 years were determined. Of the total amount of LH2 purchased over the years, 12.6 % was lost due to replenishment, 12.2 % due to normal evaporation and 20.7 % is based on load losses. This leaves 54.6 % as actual onboard quantity. [11]

The average boil-off rate of a LH2-tank strongly depends on its design and implemented mitigation methods. As for the tank shapes, the most commonly found design shapes are cylindrical and spherical shape. Spherical shaped LH2-tanks are the most efficient, since the surface-to-volume-ratio is the least, and therefore heat inflow is the least significant [5]. Prevalent boil-off mitigation methods during storage are improved insulation, such as the double walled tanks with a vacuum interspace and the utilization of baseline perlite or glass bubbles as an additional insulation layer. Glass bubbles are reported to be more efficient than perlite [12, 13, 5]. Moreover, the amount of boil-off changes with the application of the tank. For example, high-H_2-demand industrial applications need comparatively less insulation measurements, since H_2 is utilized often and boil-off becomes less of a problem. On the other side, bulk storage tanks or low demand hydrogen-tanks are made to keep high amounts of H_2 for a longer time, therefore, insulation measurements have to be advanced to keep boil-off to a minimum [13]. An overview about several applications with different insulation measurements and their respective boil-off rates is attached to this study in appendix A.1.

2.3 State-of-the-art: Boil-off recovery solutions

An often used practice of decreasing pressure in the LH2 tank is releasing the BOH to the ambient. However, this approach is accompanied by large H_2-losses and therefore potentially usable energy and capital-loss. Hence, minimizing the BOH-rate with state-of-the-art measurements should be the first step of mitigating losses. R. Morales-Ospino Et al. [5] conducted a study, reviewing state-of-the-art of boil-off hydrogen mitigation methods. The results of the following section are based on their research. Prominent methods are the Zero Boil-Off (ZBO) concept, reliquefication and compression of the boil-off gas. Utilized strategies depend on the industry, the location and the application hydrogen is going to be used in. From an economic perspective, factors such as the Operational and Capital Expenditure (OPEX and CAPEX) need to be considered, i.e. the cost of recycling BOH should not exceed its own value.

2.3.1 Zero Boil-Off

The ZBO concept from NASA [14] implements passive and active cooling technologies within a single system to ensure long term storage with optimally no boil-off losses. Passive technologies, are multilayer insulation sheets with alternating layers of reflective and low conductivity material to insure insulation or cooled shields. Active technology uses so-called IRAS-Heat Exchanger, Integrated Refrigeration and Storage. These are cryocoolers, refrigerators that work on cryogenic temperatures to remain the tank at a desired temperature. Additionally, heat exchangers can be implemented to remove radiation heat. This concept is currently being used and is continuously developed for the aerospace industry, to ensure long term savings of hydrogen for aeronautical missions.

2.3.2 Reliquefication

H_2 liquefaction plants are already existent in several countries, producing rates up to $30\frac{\mathrm{t_{H_2}}}{\mathrm{d}}$. The processes are in a well-studied state, with ongoing development. The question that arises is: how to implement the liquefaction to reduce the BOH-losses. Reliquefication is a process, which consists of the same steps as liquefaction of H_2, that is H_2 -compression, pre-cooling, cryocooling and liquefaction, the only difference being that the feed gas, BOH is collected and undergoes the upper steps to be reliquefied. The advantage of BOH reliquefication is that there is no pre-cooling necessary, therefore requires less energy. However, due to the high gas volume, the system needs to be prepared for the incoming boil-off mass to prevent further boil-off losses.

2.3.3 Compression

Hydrogen compression can be used for boil-off recovery as well. There are already a number of companies that offer such compressors commercially. To utilize gH2, it must be at a certain pressure level. However, compressing BOH at cryogenic temperatures of 20 K is a difficult operation, that must be considered in the construction process. A differentiation is made between mechanical and non-mechanical compressors, such as reciprocating, diaphragm, linear, ionic liquid or rotary and cryogenic, electrochemical, metal hydrides or adsorption compressors. Some examples of mechanical options are Linde's ionic liquid compressor 90, and non-mechanical options include the cryogenic hydrogen compressor of Air Products or HyET Hydrogen that uses electrochemical compressors that achieve flow rates up to $2000\frac{\mathrm{kg}}{\mathrm{d}}$.

2.3.4 Conclusion - BOH

The introduced measurements already suit several sizes and durations of systems, however, there is always space for improvement and innovation. Here, metal hydrides come into play. A detailed description of metal hydrides will be given in the following section.

2.4 Metal Hydrides

A metal hydride is formed by a thermochemical absorption reaction or more precisely dissociative chemisorption [15], of hydrogen, H, into the interstitial sites of a metal lattice or that of a metal alloy, M. The metal hydride reaction is represented by equation 2.1 and is depicted graphically in figure 2.2.

$$\mathrm{M}_{(\mathrm{s})} + \frac{\mathrm{X}}{2}\mathrm{H}_{2(\mathrm{g})} \xrightleftharpoons[\mathrm{Des}]{\mathrm{Abs}} \mathrm{MH}_{x(\mathrm{s})} + \Delta_{\mathrm{R}}H \qquad (2.1)$$

Figure 2.2: Concept of the metal hydride reaction depicted graphically

The basic metal or metal alloy appears in solid state, often in the form of powder. Hydrogen is absorbed in the gaseous state, and the MH is formed in the solid state. During the absorption, since the reaction is exothermic, the reaction heat, $\Delta_{\mathrm{R}}H$, is released. As this reaction is reversible, to initiate the desorption process, and therefore, to separate hydrogen from the metal, the reaction energy, $\Delta_{\mathrm{R}}H$, has to be provided to the metal hydride [16].

The absorption in detail proceeds as follows [17, 18]: At first, during a process called physisorption, H_2 is adsorbed at the metal's surface in molecular state. The actual dissociation occurs during the chemisorption process, where the molecular bonds break accompanied by a release of thermal energy. After that, hydrogen in elemental form enters the material and aggregates in the metal lattice.

Metal hydrides can be classified by either a) their elemental composition or b) their operational temperature range at 1 bar [15, 16].

The most common elemental compositions of metal hydride alloys contain one part of a strong hydride building component, A, with a high affinity to build a hydride, and a part of a weaker component, B, that provides the metal hydride with certain desired thermodynamic characteristics. Some example compositions are AB_5, AB_2 or AB. The various compositions show different distinctive characteristics, during the metal hydride reaction. $LaNi_5$, for example, that is used in this study is an AB_5-alloy. The maximal conversion rate is based on the amount of hydrogen-molecules that can be absorbed by the metal hydride.

The temperature based distinction is categorized by the hydrogen dissociation temperature at a pressure of 1 bar. There are three temperature based categories: high-, middle- and low-temperature hydrides. The dissociation temperatures are $T_{\text{high}} \geq 200$ °C, 100 °C $\leq T_{\text{middle}} \leq 200$ °C and $T_{\text{low}} \leq 50$ °C, respectively. The higher the operating temperature frame is, the higher is the bond-dissociation energy and, therefore, the more stable the hydride.

2.4.1 Van't Hoff and PCI

[19, 16] The special part about metal hydride reactions is the distinct relation between the temperature, T, the pressure, p and conversion rate of hydrogen, w_t, in the MH. This relationship is distinct for each material and is used to characterize the metal hydrides. The graphical depiction is given in the so called "Pressure-Concentration-Isotherm"-graph (PCI) shown in figure 2.3 on the left. The x-axis represents the conversion rate of hydrogen, w_t and on the y-axis the natural logarithm of the pressure over a reference pressure, most often the atmospheric pressure, is plotted.

To determine the PCIs, isothermic experiments are carried out, with step by step addition of hydrogen. After each addition, the metal hydride is left to reach a stable pressure [8]. This leaves the pressure as the only free variable, resulting in the distinctive PCI-diagrams. The isotherms temperatures appear in the following order: $T_n < T_{n+1}$.

During the exothermic absorption, three phases of metal hydride formation are observed in the PCI: α, $\alpha + \beta$, and β. In the first phase α, hydrogen co-exists with the metal in different states, forming an interstitial solid solution with the metal matrix [19]. Whereas the conversion rate at this point is still remaining low, the pressure rises following the Sieverts-law. That is, the concentration of hydrogen rises with the square root of the partial pressure of hydrogen, shown in equation 2.2.

$$w_t \approx \sqrt{p_{\mathrm{H}_2}} \tag{2.2}$$

When the concentration of hydrogen in the metal matrix is saturated, the second phase, $\alpha + \beta$, is reached, characterized by a pressure plateau, where the actual formation of the metal hydride begins. In this phase, gas, metal, and metal hydride coexist in unknown

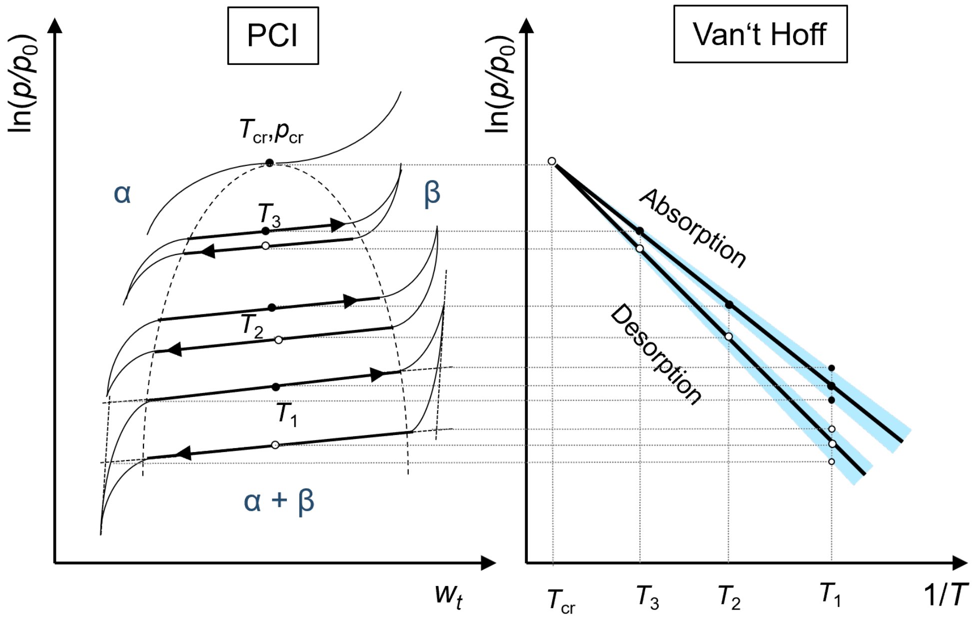

Figure 2.3: A representative PCI on the left with its corresponding Van't Hoff plot on the right

concentrations. The beginning and the end points of different isotherms of the plateau form a distinctive bell-curve, circumscribing the boundaries of the second phase. With increasing temperatures, the dissociation pressure of hydrogen rises as well. This results in a shortened plateau, up until a critical pressure, p_{cr}, and temperature, T_{cr}, above which the formation of a stable hydride is not possible any more and the metal and hydrogen co-exist separately.

After further supply of hydrogen and an increase of the conversion rate, the β-phase is reached, discernible by an exponential rise in pressure, following the Sieverts-law. At this point, the absorption of hydrogen is completed. The reversible capacity that can be reached, is presented by the plateau width of the pressure plateau. The maximum conversion rate, however, is marked by the actual end of the absorption process, and can be significantly higher, than the reversible capacity.

The reversible capacity is either defined as $\frac{\mathrm{H}}{\mathrm{M}}$ in $\frac{\mathrm{mol}_{\mathrm{H}_2}}{\mathrm{mol}_{\mathrm{M}}}$ based on the molar mass or in w_t in $\frac{\mathrm{g}_{\mathrm{H}_2}}{\mathrm{g}_{\mathrm{M}}}$ or weight% based on the mass.

When the reaction heat is provided back to the MH, the pressures of the desorption isotherms can be measured, following the same path as the absorption in reverse.

The difference between absorption and desorption isotherm pressures is called hysteresis. Hysteresis occurs due to the deformation of the metallic matrix during the hydriding and dehydriding process. The energy loss results from the energy that is necessary to create space in the metal lattice [20, 21].

Another significant impact on the pressures and temperatures has the pressure plateau slope. The origin of the slope differences is found in random substitutions of the A- or B-component of the hydride due to impurities, or in fluctuations of the stoichiometry in the homogeneous region [19].

Directly derived from the PCI, the so-called Van't Hoff graph can be generated, depicted on the right side in figure 2.3. A linear approximation of the pressures of the plateau midpoints of the isotherms is plotted over the reciprocal of the absolute temperature. The Van't Hoff graphs provide a graphical depiction of the absorption and desorption pressures at certain temperatures, however, with a certain uncertainty frame, due to the plateau slope. The different inclines of the absorption and desorption graphs, are rooted in the hysteresis phenomenon. The mid-points of the plateaus are described by the Van't Hoff equation, shown in equation 2.3.

$$\ln\frac{p_{\mathrm{eq}}}{p_0} = \frac{\Delta_{\mathrm{R}}H}{RT} - \frac{\Delta_{\mathrm{R}}S}{R} \tag{2.3}$$

p_{eq} is the pressure at the plateau mid-point and p_0 a reference pressure, often the atmospheric pressure. R is the ideal gas constant, $\Delta_{\mathrm{R}}H$ the reaction enthalpy, or the bond-breaking/ -building energy, and $\Delta_{\mathrm{R}}S$ the reaction entropy.

Above the absorption curve in the Van't Hoff diagram the metal hydride is in hydrogenated state, whereas, below the desorption graph, the MH is in dehydrogenated state.

The relationship between temperature and pressure is the basis to conduct a thermal compression with metal hydrides. E.g., with controlled heat supply to the system, to change the temperature and to provide the reaction heat, higher pressures of hydrogen in the MH can be reached and made available after the desorption.

2.4.2 Kinetics and activation

The dynamics of the metal hydride reaction in general are influenced by two major factors, the intrinsic kinetics in dependence on the pressure and the temperature [18] and the heat transfer during the absorption and desorption process [19].

Since the thermal conductivity of metal hydrides is rather low, a continuous supply and removal of heat, during desorption and absorption, respectively, is necessary to provide a full reaction.

The kinetics of the metal hydride reaction can be described by equation 2.4. It defines the three major influences on the reaction rate, $\frac{\partial x}{\partial t}$, the temperature, the pressure and the intrinsic reaction characteristics [22].

$$\frac{\partial x}{\partial t} = \underbrace{\overbrace{-A \cdot e^{-\frac{E_a}{RT}}}^{\text{Arrhenius}} \cdot f(p)}_{k} \cdot f(x) \tag{2.4}$$

The temperature influence is depicted by the Arrhenius equation. A is the frequency factor, E_a the activation energy, R the ideal gas constant, and T the absolute temperature. Therefore, if the absorption temperature is decreasing, the kinetics are decreasing as well.

The pressure function can be described by, for example, the equations presented in equation 2.5. An important aspect regarding the possible pressure functions is that if the equilibrium pressure p_{eq} is equal to the reference pressure p_0, the kinetics become zero. Together with the temperature function, the pressure functions forms the reaction rate coefficient k.

$$(1) \quad f(p) = \left(\frac{p_0 - p_{\text{eq}}}{p_{\text{eq}}}\right) \qquad (2) \quad f(p) = \ln\left(\frac{p_0}{p_{\text{eq}}}\right) \tag{2.5}$$

The last influence on the kinetics, $f(x)$, is determined by the intrinsic reaction mechanism. In other words, if all H_2 is converted, the reaction is terminating and therefore, the kinetics approach 0. In the form of an equation, this could look as followed (2.6):

$$(1) \quad f(x) = x_{\max} - x \qquad (2) \quad f(p) = \ln\left(\frac{x}{x_{\max}}\right) \tag{2.6}$$

Other influences on the kinetics are a proper activation and impurities in the hydride. Before the material can be utilized, the surface has to be cleansed by all adsorption and oxide layers, since they inhibit hydrogen diffusion into the MH. This involves, several steps of heating the hydride on high temperatures under vacuum conditions, and reduction of the surface with hydrogen as a reduction agent. These steps are repeated until the maximum conversion rate is reached for the first time. [16]

The dynamics of the system later determine the duration and efficiency of hydrogen absorption and desorption during the thermal compression. Moreover, it influences the size and therefore, the cost of the reactor.

2.4.3 Applications

Metal hydrides have several applications, such as mobile and stationary H_2 storage, hydrogen purification, separation or recovery or for a thermal compression [15]. On the first gaze at the MH-reaction 2.1, metal hydrides only seem to function for hydrogen applications. However, since heat is applied to the hydride during the dehydrogenation, it actually can serve as a thermal heat storage as well. This enables other areas of application, such as heat pumps [23], or refrigeration [8, 15]. In this study, however, the main focus will be on hydrogen boil-off recovery and the thermal compression using metal hydrides.

Thermal compression

The general concept of a thermal compression with metal hydrides is shown in figure 2.4. Hydrogen is absorbed at lower pressures and therefore lower temperatures, while releasing exothermic absorption energy. Thermal energy is supplied to heat the system to the desorption temperature which provides the desired high pressure. As a last step, the reaction enthalpy is provided to drive the desorption, and hydrogen is released on a high pressure, completing the thermal compression with metal hydrides.

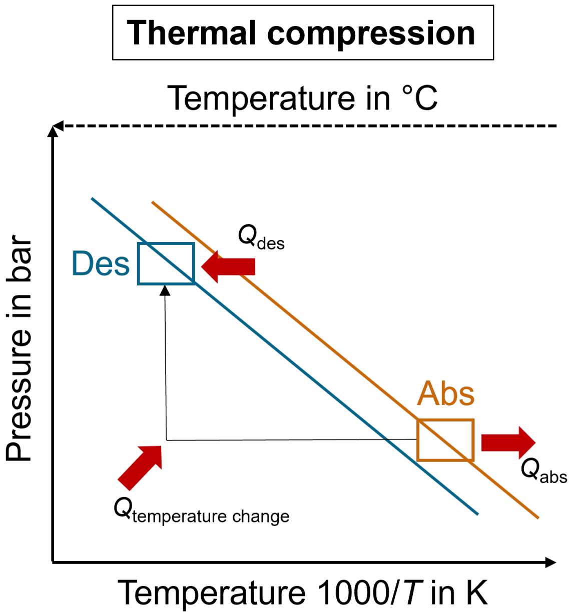

Figure 2.4: Schematic depiction of a compression process with metal hydrides based on the Van't Hoff diagram

The simplest concept for conducting a thermal compression is based on one reactor with one MH, as used in this study. However, in real applications it is more likely, that several reactors with different metal hydrides that are connected in series, are used to enable step by step compressions to higher pressure levels [19] or two reactors with the same material, to provide a quasi-continuous operation.

The MH-materials used for thermal compressions have to fulfil certain characteristics regarding their material properties. At first, the reaction temperatures and plateau pressures of each MH have to be selected carefully with regard to the other materials, to secure full desorption and absorption processes. The reversible hydrogen storage capacity should be high and there should neither be a high plateau slope nor a severe hysteresis. The kinetics should be sufficiently fast and the activation performance of the hydride high. Moreover, it should be tolerant against impurities to prevent MH-poising, which inhibits the performance of the hydrogenation process. As a last aspect, the cycle efficiency should not increase over time, providing a high cycle time. The metal alloys most commonly used are of the AB-, AB_2-, and AB_5-type. [24]

After introducing the basics regarding boil-off and the metal hydride reaction, in the main part of the study, a proof of concept of a thermal compression with a metal hydride reactor for H_2 boil-off recovery will be presented.

3 Application and Materials

Thermally driven hydrogen compression using metal hydrides is a well-known field, and the general boil-off concept has been proven for example in research carried out for NASA in 1987 [6]. However, with increasing hydrogen infrastructure, the demand for boil-off capture methods is increasing and potential new applications beyond spacecraft are established. To identify such applications and their boundary conditions, several interviews and a small research study were carried out. In the second part of this chapter, based on the interview results, a material discussion is presented to identify a suitable material for the consecutive experimental part of the study.

3.1 Interviewer Profiles

This section presents the profiles of different possible applications identified by interviews and literature study. This includes a summary of important data, a short description of the application, and an analysis of the process chain with boil-off sources.

Before conducting the interviews, some initial requirements for the applications suitable for thermal compression using metal hydrides were determined. For the absorption, the in flowing hydrogen has to be at low pressure, thus the absorption has to be performed at low temperature levels, aligning with the Van't Hoff curves. Moreover, it should be possible to release the absorption heat to the ambient without additional cooling, in order to avoid additional energy input and therefore extra costs. With regard to the desorption, since high H_2 pressures are required for most applications, and high pressure corresponds to high temperatures, external waste heat sources or the temperature of the environment should be utilized to minimize external energy consumption.

3.1.1 MGT - Profile

Profile 1 - MGT

Application:	Micro gas turbine
Application identification:	MGT (Micro Gas Turbine)
Hydrogen source	gH2
Further H_2 utilization:	MGT
Affiliation:	DLR, Institute for Combustion Technology
Location:	DLR, Stuttgart

The data in this subsection were established during discussions with the colleagues from the Institute of Combustion Technology (ICT) at DLR.

Figure 3.1 depicts a flowchart with a simplified MGT-cycle and a coupled MH-reactor. The MGT-cycle works as follows: an air mass flow, marked with yellow arrows, at a low temperature is sent through a recuperator, where its temperature is increased. The hot air flow is then provided to a combustion chamber, where it is burned together with a fuel gas.

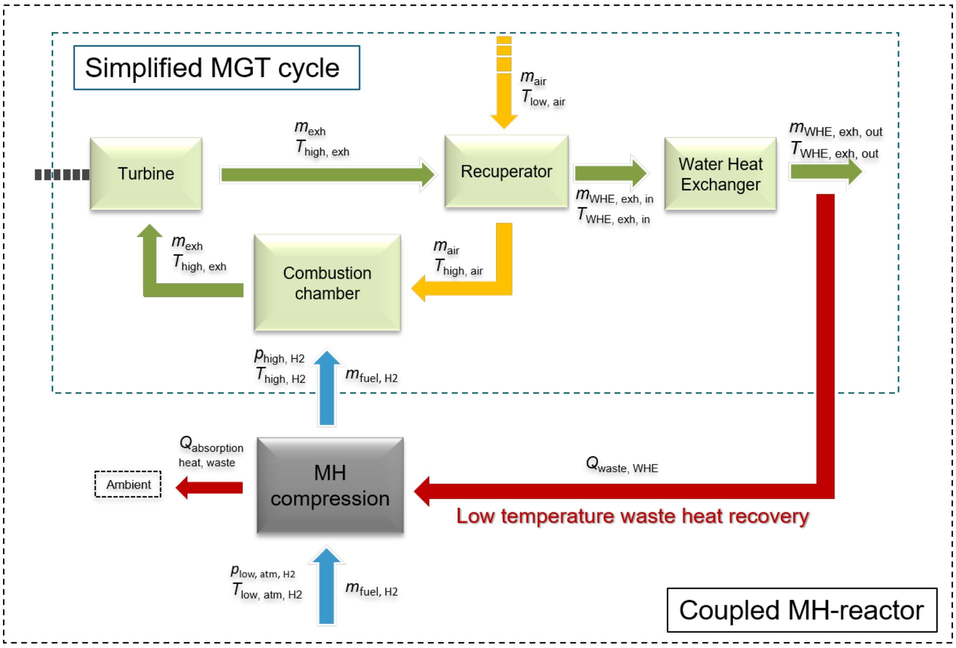

Figure 3.1: Process chain of MGT

The exhaust mass flow on a high temperature leaving the combustion chamber, marked with green arrows, reaches a turbine, which utilises the mass flow to generate energy. After that, the still hot exhaust mass flow is sent back to the recuperator where it is used to heat the air mass flow. It leaves the recuperator on a lower temperature level and enters a Water Heat Exchanger (WHE) where the temperature is further reduced.

In some cases, due to pressure differences hydrogen is provided at pressure levels that are too low for a mass flow to occur. Here, the MH-reactor comes into play. Normally, a compressor would be utilized to prepare the inflowing hydrogen, however, as an initial application the substitution of the compressor with a MH-reactor was determined. Low pressure hydrogen, hydrogen mass flows are coloured blue, is provided to the reactor at room temperature and the exothermic absorption heat is released to the environment. The compression is initiated by heating the reactor to desorption temperature. The compressed H_2 on a higher temperature is sent to the combustion chamber, where it is mixed with the air and combusted as a fuel-air mixture. To drive the thermal compression with the metal hydride, the energy from the exhaust mass flow leaving the water-heat exchanger, $T_{\text{WHE, exh, out}}$, can be provided.

The application in this case is not necessarily designed to capture BOH, it is rather a method to compress fuel hydrogen before it enters the combustion chamber of the MGT. However, the principle of a thermal driven metal hydride compression remains.

The following conditions were identified during the interview with the researchers from ICT, and are summarised in table 3.1.

Table 3.1: Results of the interview with the researchers from ICT

Variable	Unit	Value
$m_{\text{fuel, H}_2}$	$\frac{\text{g}}{\text{s}}$	2.79
m_{air}	$\frac{\text{g}}{\text{s}}$	800
$T_{\text{WHE, exh, in}}$	°C	280
$T_{\text{WHE, exh, out}}$	°C	82
p_{abs}	bar	1
p_{des}	bar	4
T_{abs}	°C	15-30
T_{des}	°C	60-80
$\frac{p_{\text{des}}}{p_{\text{abs}}}$ (min-max)		4
ΔT (min-max)	K	30-65

3.1.2 LTS - Profile

Profile 2 - LTS

Application:	Long term storage
Application identification:	LTS (Long Term Storage)
Boil-off source	LH2 storage
Further H_2 utilization:	Fuel cell
Affiliation:	DLR, BALIS
Location:	DLR innovation campus, Empfingen

BALIS is a test facility of DLR with the location in Empfingen. The main goal is to develop a fuel cell powertrain for aircraft in the megawatt range for short range regional aircraft [25].

During the interview, several steps with boil-off losses were identified, which are presented graphically in figure 3.2 and figure 3.3. Before the tank is fuelled for the first time, the pipelines and the empty tank have to be brought to operating temperature of 20 K, which is the temperature of LH2. For this purpose, several flushing and purging steps with nitrogen and hydrogen are undertaken. Here, the first source of boil-off is identified. If the tank was to be decommissioned, more losses would occur.

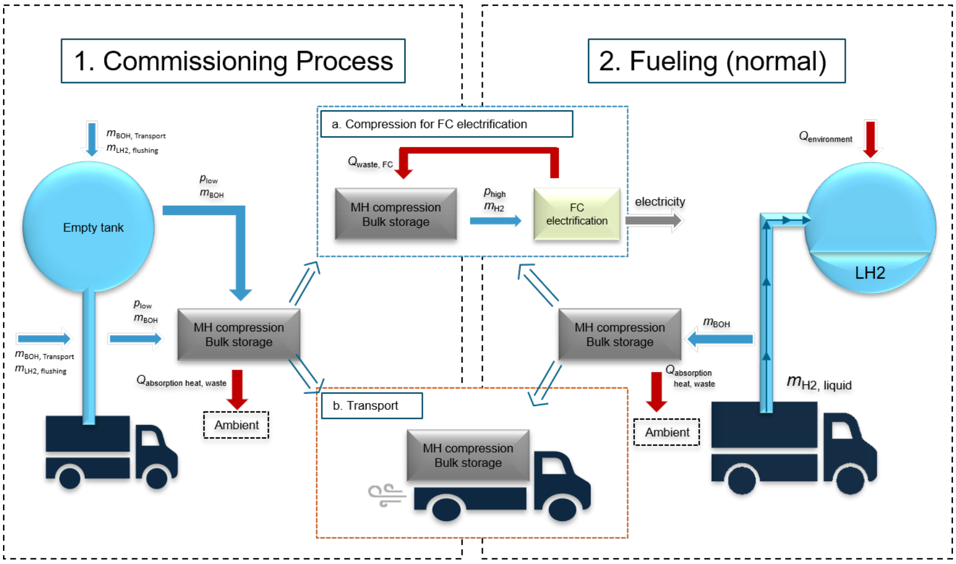

Figure 3.2: Process chain of LTS

After the system is cooled down to the operating temperature, the fuelling process can be initiated. However, due to incoming heat from the environment, the pipelines and the tank are heated. This results in BOH production during the fuelling process and this BOH needs to be released.

For the commissioning process as well as the fuelling, the first integration option for a MH-reactor with the application arises. The BOH can be captured by the reactor and for further usage can a) either be connected to a fuel cell, where hydrogen is compressed to fit the fuel cells requirements to produce electricity, for example to drive small vehicles or b) transported within the site to other potential operational locations for hydrogen consumption.

After the LH2 tank is fully fuelled, depending on the hydrogen demand, the liquid hydrogen is stored for a presumably long duration. However, as explained in section 2, due to heat input from the environment, the liquid hydrogen will become eventually gaseous. Normally, that boil-off is released to the environment.

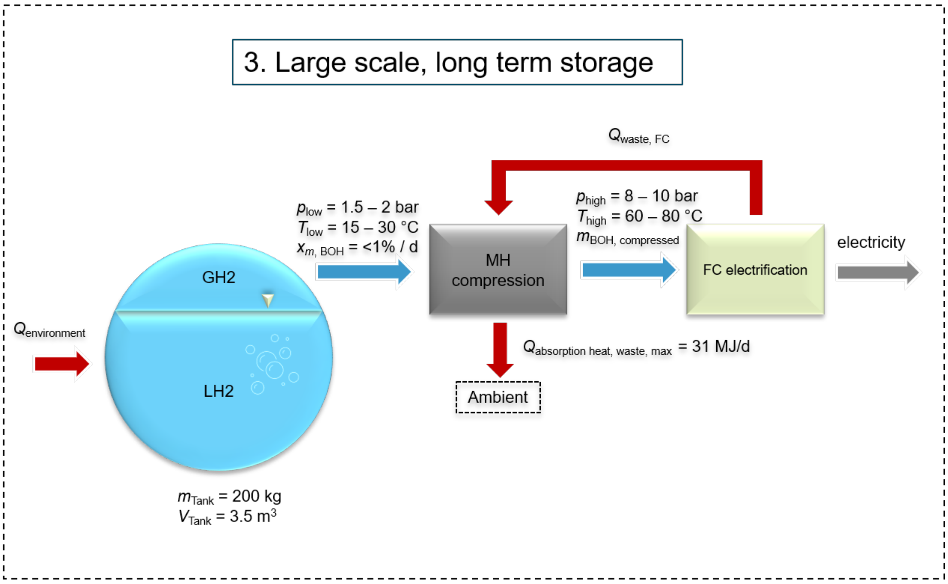

Figure 3.3: Storage application of LTS

Thus, the second possible application for coupling with a MH-reactor can be identified. The reactor is linked to the LH2-tank and captures the low pressure BOH. During the absorption at room temperature, thermal energy is released to the environment. The H_2 then is compressed to a higher pressure and can be further used to feed a fuel cell. The special part about this application is that during the desorption process, the fuel cell's waste heat can be utilized for the compression of hydrogen. The desorption temperature, therefore, needs to be below the temperature at which the waste heat can be provided. In this case, no additional energy input would be required.

In the discussion with the BALIS researchers the following boil-off conditions, noted in table 3.2, were determined:

Table 3.2: Results of the interview with the BALIS researchers

Variable	Unit	Value
m_{Tank}	kg	200
V_{Tank}	m^3	3.5
$x_{m,\text{ BOH}}$	$\frac{\%}{\text{d}}$	< 1
p_{abs}	bar	1.5-2
p_{des}	bar	8-10
T_{abs}	°C	15-30
T_{des}	°C	60-80
$\frac{p_{\text{des}}}{p_{\text{abs}}}$ (min-max)		4-6.68
ΔT (min-max)	K	30-65

3.1.3 sLH2 - Profile

Profile 3 - sLH2

Application:	High pressure storage application
Application identification:	sLH2 (Subcooled Liquid Hydrogen)
Boil-off source	sLH2
Further H_2 utilization:	Introduction to gas pipelines
Affiliation:	Daimler Truck, Linde Engineering

sLH2 is short for subcooled liquid hydrogen. It is produced by using 3 bar LH2 from a stationary LH2 storage tank that is compressed by a special cryopump during the fuelling process. It is cooled down in the vehicle tank, condensed and compressed to a pressure of 16 bar. Therefore, the temperature of sLH2 can be 26 K instead of 20 K. The most common utilization of sLH2 tanks is found in trucks [26].

The unique feature of sLH2 is the fuelling process. Whereas the normal process presented in section 2.1 results in boil-off losses every time, due to cryopump technology the hydrogen stays liquid and no BOH is found during the fuelling process [27], visualized in figure 3.4. However, during storage, due to external heat in-flow, boil-off is still inevitable. Here, with similar pressure ratios as the storage application of BALIS, presented in subsection 3.1.2, a metal hydride reactor can be linked to the tank to capture the BOH.

The more significant boil-off source, however, is the vehicle tank itself. Despite prelim-

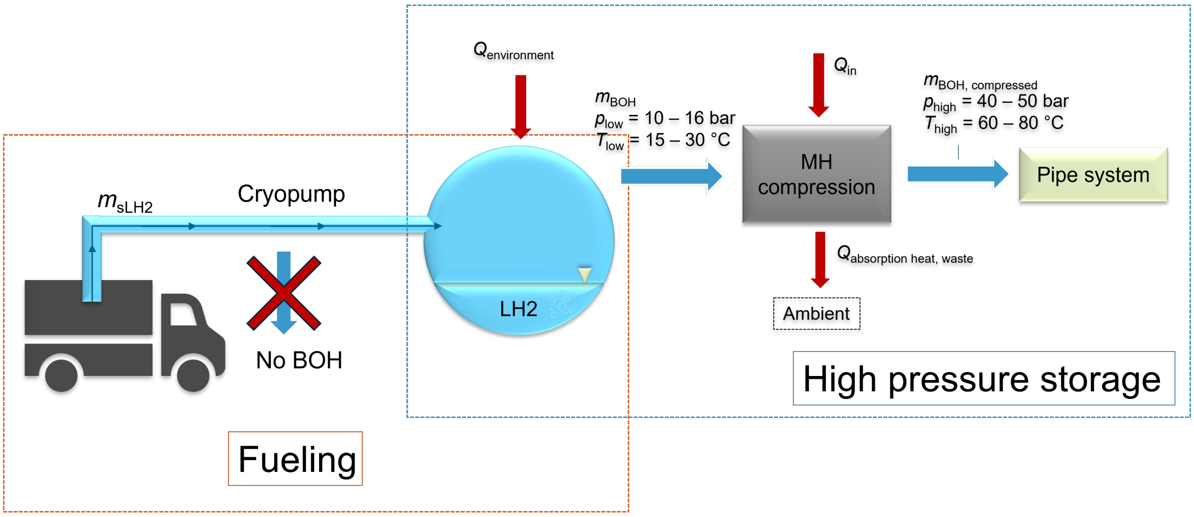

Figure 3.4: Flow chart of the fuelling and storage process of sLH2

inary insulation measurements, if the original State Of Charge (SOC) is 100 %, after 8 h boil-off starts exceed the safety pressure. After 160 h only 50 % of hydrogen remains in the tank [28]. The boil-off, detected here, leaves the system at pressures of approximately 16 bar. The MH-reactor could be implemented in the vehicle, to capture the BOH as a puffer storage. Concluding that, not only near atmosphere pressure boil-off is found, but also cases where the pressures reach 16 bar.

This enables another use case for MH-based thermal H_2 compression. Utilizing sLH2 in vehicle tanks is a relatively new technology, and if in the future more sLH2 applications will spread, high pressure boil-off needs to be expected. Representative for this BOH, as an example, a sLH2-storage application will be presented in the following and graphically in figure 3.4. The MH-reactor is linked to the storage tank and captures the boil-off at an estimated pressure range of $10 - 16$ bar. After that, the compression is undertaken as normal and the compressed hydrogen can be recycled by sending them back for further application into, for example, gas pipelines. Since the average pressure in the pipelines is approximately $40 - 50$ bar, the compressed hydrogen has to be provided at the same level. As absorption and desorption temperatures, $T_{\text{abs}} = 15 - 30$ °C and $T_{\text{des}} = 60 - 80$ °C can be estimated.

In total, three potential thermal compression scenarios were analysed, with several potential metal hydride coupling opportunities. For each application, the boundary conditions were identified. The available temperature range appears to be identical for all use cases, whereas the absolute pressures vary. However, the pressure ratios are quite similar. A summary of these conditions is given in the next section in table 3.4.

Table 3.3: Results of the research regarding sLH2

Variable	Unit	Value
p_{abs}	bar	10-16
p_{des}	bar	40-50
T_{abs}	°C	15-30
T_{des}	°C	60-80
$\frac{p_{\mathrm{des}}}{p_{\mathrm{abs}}}$ (min-max)		2-5
ΔT (min-max)	K	30-65

3.2 Material discussion

After identifying use cases for a thermal compression with metal hydrides, suitable materials for each application are determined, to conduct further experiments. In the following sections, pre-selected materials available in the DLR database will be discussed and compared in terms of applicability for the applications presented in section 3.1. In the first step, a preliminary selection based on the interview profiles and corresponding Van't Hoff plots is performed. As a final step, a more detailed look at the materials is undertaken by analysing the PCIs to gather more precise information about real absorption/desorption pressures as well as associated temperatures. The overall aim of this section is to determine a material for conducting experiments to demonstrate the concept of a thermally driven metal hydride compressor.

3.2.1 Van't Hoff

The materials chosen for a suitability check for MGT and LTS are $\mathrm{LaNi_5}$, $\mathrm{LaNi_{4.75}Al_{0.25}}$, $\mathrm{LaNi_{4.85}Al_{0.15}}$, $\mathrm{LaNi_{4.9}Al_{0.1}}$ and $\mathrm{TiFe}_x\mathrm{Mn}_y$ ($x = 44-47$ and $y = 4-7$) and the Hydralloys C1, C2 and C5 for sLH2. The corresponding Van't Hoff plots, depicted in figures 3.5, 3.6 and 3.7, show the desorption (solid lines) and absorption characteristics (dashed lines) for each material. The boundary conditions for the different applications are marked with black horizontal and vertical lines. An overview of the absorption and desorption pressures and temperatures taken from the interviews in section 3.1 is shown in table 3.4. Additionally, the pressure ratios $\frac{p_{\mathrm{des}}}{p_{\mathrm{abs}}}$ are included. The average ratio, that has to be overcome, is similar for all applications and centred around 4.

Since the absorption occurs under near ambient conditions, temperature fluctuations during the year need to be considered while investigating the material's applicability. Higher temperatures will be assumed during summer and lower temperatures during

Table 3.4: The required pressure ranges for each application at $T_{\mathrm{abs}} = 15 - 30$ °C and $T_{\mathrm{des}} = 60 - 80$ °C with $\Delta T = 30 - 65$ K

Application	MGT	LTS	sLH2
p_{abs} in bar	1	$1.5 - 2$	$10 - 16$
p_{des} in bar	4	$8 - 10$	$40 - 50$
$\frac{p_{\mathrm{des}}}{p_{\mathrm{abs}}}$ (min-max)	4	$4 - 6.7$	$2.5 - 5$

winter. Generally speaking, to decrease additional energy input, it is desirable to utilize the thermal energy of the ambient. Therefore, a metal hydride that is applicable regardless of seasonal variations would be beneficial. That means, for the absorption higher temperatures are desirable, so that, regardless of the ambient conditions, the heat resulting from the exothermic reaction can be removed, without additional cooling.

For the desorption temperatures, the same principle applies in reverse: Lower temperatures are desired to be able to utilize waste heat of accompanying applications without much extra effort.

MGT

Following the introduction of MGT in subsection 3.1.1, requirements for the application were found to be $T_{\mathrm{abs}} = 15 - 30$ °C at a pressure $p_{\mathrm{abs}} = 1$ bar and $T_{\mathrm{des}} = 60 - 80$ °C at a pressure $p_{\mathrm{des}} = 4$ bar.

The variety of available metal hydrides at DLR can be seen in figure 3.5. To determine suitable materials, the intersection points of the abs/des curves with the lines marking the boundary conditions are noted in table 3.5. Temperatures within the range are marked bold, italic presents below the range values and standard font above the required temperature range.

As previously mentioned, in order to represent as broad ambient conditions as possible, a material that can *absorb* close to 1 bar in a higher temperature range is aimed for. In this case, meeting the given temperature requirements are met by $\mathrm{LaNi_{4.85}Al_{0.15}}$ and $\mathrm{LaNi_{4.9}Al_{0.1}}$ whose absorption curves intersect the 1 bar mark at around 22 °C and at 17.5 °C, respectively. $\mathrm{LaNi_{4.75}Al_{0.25}}$ absorbs at 34 °C, which is higher than the given range, however, as previously explained, higher temperatures are of advantage for the absorption procedure. $\mathrm{FeTi}_x\mathrm{Mn}_y$ and $\mathrm{LaNi_5}$ both absorb below range, excluding them from further discussion for MGT.

Regarding the *desorption*, for the materials at hand, $\mathrm{LaNi_{4.85}Al_{0.15}}$ cuts the 4 bar mark at 71 °C, therefore meeting the requirements. $\mathrm{LaNi_{4.9}Al_{0.1}}$ with its T_{des} of 59 °C closely misses the lower end of the range. However, for the desorption lower temperatures are desired, therefore it can be still be seen a good fit. $\mathrm{LaNi_{4.75}Al_{0.25}}$ desorbs at 82 °C which

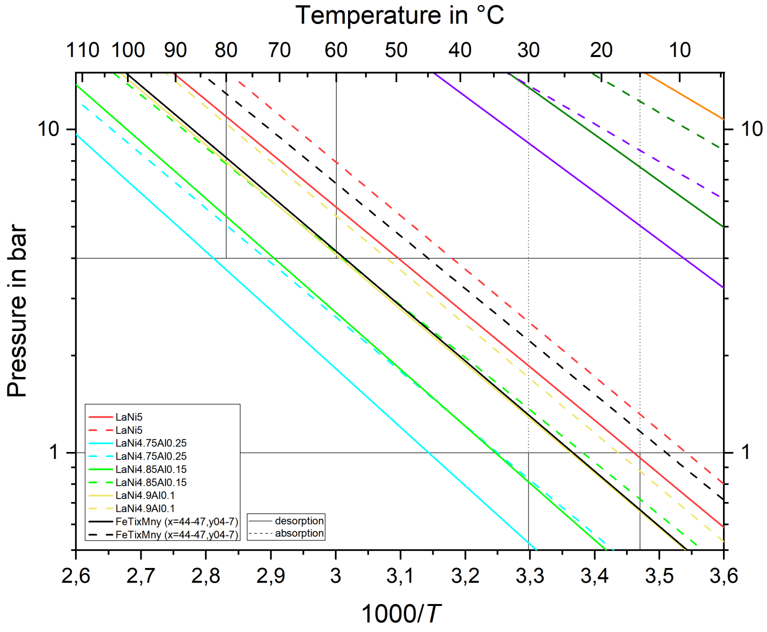

Figure 3.5: Van't Hoff diagram for the MGT application

Table 3.5: MGT temperature data for absorption at 1 bar and desorption at 4 bar

MGT	$LaNi_5$	$LaNi_{4.9}Al_{0.1}$	$LaNi_{4.85}Al_{0.15}$	$LaNi_{4.75}Al_{0.25}$	$FeTi_xMn_y$
T_{abs} in °C	*8*	**17.5**	**22**	34	*12*
T_{des} in °C	*50*	*59*	**71**	82	*58*

is slightly too high. However, since the absorption characteristics seem quite promising, it still remains the object of consideration.

As presented in subsection 3.1.1 the desorption process is dependent on the temperature range of the water-heat-exchanger's waste heat. Since the work frame is fixed, an accurate selection is limited to the given settings. However, if higher waste heat temperatures could be employed, wider materials options could be obtained. In this case, though, what needs to be taken into account is the influence of the machine's efficiency when the temperature settings for the MGT would change.

For subsequent analysis, $LaNi_{4.85}Al_{0.15}$ remains the only option that fully satisfies the criteria. Additionally, the PCIs of $LaNi_{4.75}Al_{0.25}$ and $LaNi_{4.9}Al_{0.1}$ will be examined as representatives of the upper and the lower range of absorption and desorption, respectively, missing the requirements by a slight margin but both having either promising absorption or desorption conditions.

LTS

The required parameter settings for the LTS application are $T_{\mathrm{abs}} = 15 - 30$ °C at $p_{\mathrm{abs}} = 1.5 - 2$ bar and $T_{\mathrm{des}} = 60 - 80$ °C at $p_{\mathrm{des}} = 8 - 10$ bar.

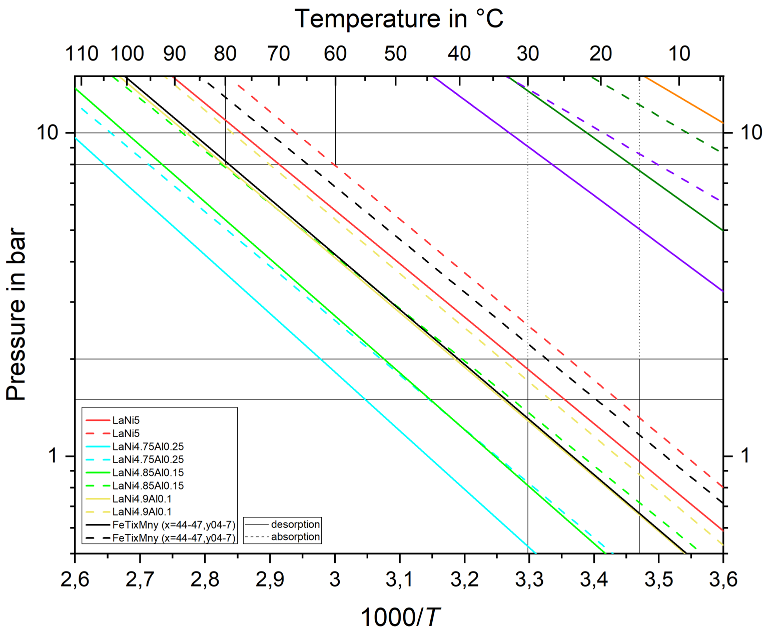

Figure 3.6: Van't Hoff diagram for the LTS application

Analogous to the MGT application, the required data to determine a suitable material was obtained from the intersections of the black lines, representing the application's operational scope, with the Van't Hoff curves, as shown in figure 3.6. The absorption and desorption pressures and temperatures from that analysis are displayed in table 3.6. However, since LTS provides an additional pressure range, two values are noted, the first one for the lower limit and the second for the upper limit.

Table 3.6: LTS temperature data for absorption at $1.5 - 2$ bar and desorption at $8 - 10$ bar

LTS	$LaNi_5$	$LaNi_{4.9}Al_{0.1}$	$LaNi_{4.85}Al_{0.15}$	$LaNi_{4.75}Al_{0.25}$	$FeTi_xMn_y$
T_{abs} in °C	**18-24**	**27**-34	32-39	45-52	**21-28**
T_{des} in °C	**70-77**	**80**-88	92-100	105-114	**79**-86

LTS *absorption* temperatures are the same as for MGT. However, since pressure ranges are more flexible, a broader spectrum of materials is available for selection. For LTS, the argument regarding the seasonal temperature change, is also considered in the following discussion.

As presented in table 3.6, operating within the upper and lower limit, there is the red line, representing $LaNi_5$, and the black line for $FeTi_xMn_y$. $LaNi_{4.9}Al_{0.1}$ starts to absorb in the range, however, exceeding the temperature limit before reaching the pressure limit. Taking into account the seasonal discussion and optimal applicability, out of those three options, $FeTi_xMn_y$ seems to be the most promising option since it covers the specific application requirements, and even in a higher range than $LaNi_5$.

$LaNi_{4.85}Al_{0.15}$ starts absorbing at 32 °C and $LaNi_{4.75}Al_{0.25}$ at 45 °C. Although being higher than the boundary conditions $LaNi_{4.85}Al_{0.15}$ and $LaNi_{4.75}Al_{0.25}$ can still be considered an option, since higher absorption temperatures are desired.

The only material starting and ending in the *desorption* range is $LaNi_5$ from $70 -$ 77 °C. Right at the upper limit of 80 °C lie $FeTi_xMn_y$ and $LaNi_{4.9}Al_{0.1}$ with 81 °C. $LaNi_{4.85}Al_{0.15}$ start desorbing at 92 °C and $LaNi_{4.75}Al_{0.25}$ at 105 °C which is too high for the requirements.

The additional heat for the metal hydride for LTS is intended to be provided by the waste heat of the fuel cell or the ambient. The waste heat of fuel cells operate in stricter ranges and as written above, higher temperatures mean additional energy consumption, influencing the efficiency. Therefore, it is more desirable to utilize the heat of the ambient as well. Hence, temperatures at the lower desorption range are desirable. However, for reasons such as plateau slope, slightly above requirement desorbing options should still be considered.

Taking all the arguments in account, for the LTS application $LaNi_5$, $LaNi_{4.9}Al_{0.1}$ and $TiFe_xMn_y$ will be further discussed.

sLH2

Referring to subsection 3.1.3, the parameter range for sLH2 was established to be $T_{\text{abs}} = 15 - 30$ °C at a pressure $p_{\text{abs}} = 10 - 16$ bar and $T_{\text{des}} = 60 - 80$ °C at a pressure $p_{\text{des}} = 40 - 50$ bar. The pressure range of sLH2 varies significantly from the previous use cases, thus, different materials have to be considered. However, although the pressure range is considerably higher, since the ratios $\frac{p_{\text{des}}}{p_{\text{abs}}}$, presented in table 3.4, all vary around 4, similar ΔT are necessary to overcome the pressure ratio. The new conditions are illustrated in figure 3.7 and intersections with the boundary conditions are summarized in table 3.7.

Hydralloy C5, provides the best alignment with the *absorption* requirements. It even exceeds the limits by 5 K, absorbing hydrogen at 16 bar at 35 °C. Although it absorbs higher than the boundary conditions, in analogy to the other use cases, since it covers a wide fraction of the range and higher absorption conditions are desirable, Hydralloy C5 seems like a promising material. In contradiction, Hydralloy C1 exhibits absorption temperatures between -22 °C and -3 °C, which is below the range, thus excluding it from further discussion. Hydralloy C2 absorbs at low temperatures as well, however, not as severe as those of Hydralloy C1. The corresponding temperature for $p_{\text{abs}} = 16$

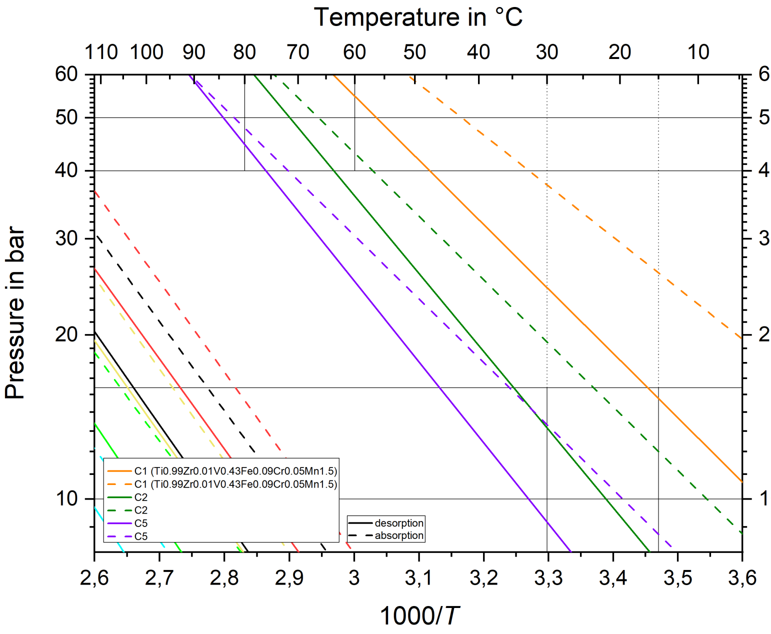

Figure 3.7: Van't Hoff diagram for the sLH2 application

bar, is 23 °C, which lies within the given scope. However, comparing Hydralloy C2 and C5, regarding their absorption conditions, the higher temperatures of C5 would be preferred.

Table 3.7: sLH2 temperature data for absorption at 10 – 16 bar and desorption at 40 – 50 bar

sLH2	C1	C2	C5
T_{abs} in °C	-22 to -3	9-**23**	**20**-35
T_{des} in °C	48-56	**63-71**	**77**-84

The pressure limits for the *desorption* are relatively strict within the range, since it has to meet the pressure of the gas pipelines of $40 - 50$ bar. The desorption temperatures of C2 are $T_{\text{des}} = 63 - 71$ °C, which match the boundary conditions perfectly, even covering the lower part of the range, which is preferred when discussing the desorption. Hydralloy C5 only meets the range between 77 °C and 80 °C. At 50 bar T_{des} is 84 °C, which is slightly above requirements, but still potentially manageable.

Therefore, concluding this section, for further discussions, Hydralloys C2 and C5 are selected.

Especially when comparing the material selection of LTS and MGT it becomes evident that the material selection is very sensitive to actual boundary conditions, as even with a slightly different pressure range for same temperatures, different materials become more suitable.

An overview of the interim results based on the Van't Hoff material selections is given in table 3.8. Based on these findings, in the following subsection, the detailed PCIs are analysed.

Table 3.8: Preliminary material selection based on the Van't Hoff curves

	$LaNi_5$	$LaNi_{4.9}Al_{0.1}$	$LaNi_{4.85}Al_{0.15}$	$LaNi_{4.75}Al_{0.25}$	$FeTi_xMn_y$
MGT	x	✓	✓	✓	x
LTS	✓	✓	x	x	✓
	C1	C2	C5		
sLH2	x	✓	✓		

3.2.2 PCI discussion

Although Van't Hoff graphs are sufficient for a preliminary selection of materials, as described in section 2.4.1, because of plateau slope, the actual absorption and desorption pressures differ from the Van't Hoff graph. Therefore, in this subsection, the more detailed PCIs of the materials presented in table 3.8 are analysed. The different graphs are marked with stars and lines in two colours: red and blue for absorption and desorption, respectively. The location of the tags are selected based on the start/end of the material's plateau. For an absorption, the majority of the H_2 should be converted, implying, high reacted fractions should be reached. Therefore, a point at the end of the plateau, before the pressure starts rising exponentially, is selected. The same applies to the desorption in reverse: when the pressure reaches the plateau and most of the hydrogen is released, the mark is set. The blue and red lines are auxiliary marks to indicate the corresponding pressures to the star marks. The given temperature ranges in all applications are 15 − 30 °C and 60 − 80 °C, however, not for all boundary conditions available PCIs are reported. For these cases, the data as close as possible to the desired temperature are evaluated and based on that, statements about the desired temperatures are derived.

In general, when comparing the data from PCIs to corresponding Van't Hoff diagrams, the realistic absorption pressure, that is the point when most of the H_2 is converted, is higher than the plateau mid-point pressure in the Van't Hoff. For the desorption the corresponding value is lower. The difference in both cases depends on the intensity of the plateau slope.

MGT

Material selections, based on the Van't Hoff discussions, are $LaNi_{4.75}Al_{0.25}$, $LaNi_{4.85}Al_{0.15}$ and $LaNi_{4.9}Al_{0.1}$. They are evaluated in the following examination using the corresponding PCIs.

The data of the PCIs reported for **$LaNi_{4.75}Al_{0.25}$** by Koller [29] show a quite steep plateau slope that increases with temperature. For lower temperatures, relevant for the absorption, depicted in figure 3.8a, the plateaus for 20 °C and 50 °C start in the low pressure area at 0.4 bar and 0.9 bar and end at around 1.4 bar and 5 bar, respectively. This results in a pressure range of the plateau slope of $\Delta p = 1.4 - 5$ bar, which is quite high. The MGT application needs materials which can absorb at room temperature under the ambient pressure of 1 bar. The isothermic curves have similar distances between their 10 K temperature steps, therefore, an ambient pressure absorption can be approximated at around 10 − 15 °C, which is too low.

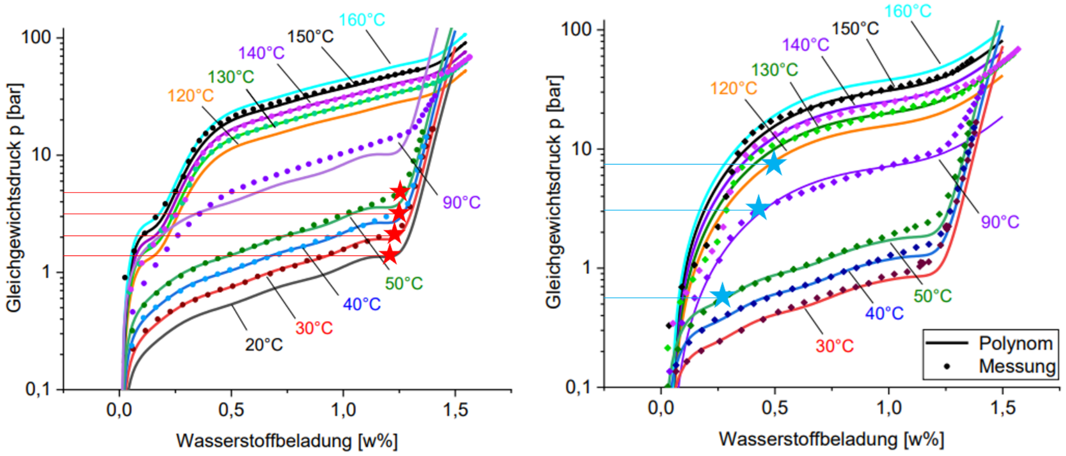

(a) PCI Absorption $LaNi_{4.75}Al_{0.25}$ **(b)** PCI Desorption $LaNi_{4.75}Al_{0.25}$

Figure 3.8: PCI of $LaNi_{4.75}Al_{0.25}$ taken from Koller [29]

In analogy to the absorption, the desorption in figure 3.8b, the slope is significantly high, even more so, due to the characteristics of a logarithmic scale. In the extreme for 160 °C, the difference between beginning and end of desorption is already approximately $\Delta p = 40$ bar, with a Van't Hoff plateau mid-point at 33 bar, resulting in a difference of 13 bar between the Van't Hoff and the PCI data. With ±10 °C the boundary conditions, for the values 90 °C and 50 °C, that difference is 4 bar and 2 bar. The majority of hydrogen is released at 3 bar and 0.55 bar, respectively. This is too low compared to the desired pressure of 4 bar for MGT. If higher temperatures, around 100 °C could be provided, the application could be realized with $LaNi_{4.75}Al_{0.25}$.

For **$LaNi_{4.85}Al_{0.15}$**, two figures from different publications are available which show data for different temperatures. For the lower absorption temperatures, figure 3.9a taken from

Kölbig [22] is used for the analysis.

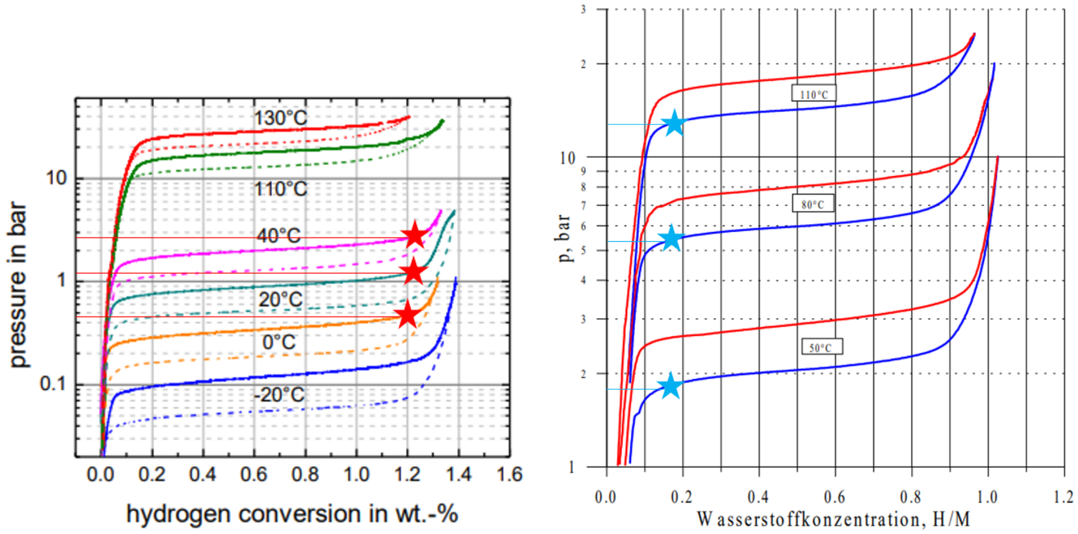

(a) PCI $LaNi_{4.85}Al_{0.15}$ [22]

(b) PCI $LaNi_{4.85}Al_{0.15}$ [30]

Figure 3.9: PCI of $LaNi_{4.85}Al_{0.15}$ taken from Kölbig [22] and Willers [30]

Although the plateau slope is not ideal, it is significantly better than that of $LaNi_{4.75}Al_{0.25}$. Therefore, the values should be similar to the corresponding Van't Hoff data. According to the data in figure 3.9a, the absorption at 20 °C is close to complete at approximately 1.1 bar. These are more optimal absorption conditions compared to $LaNi_{4.75}Al_{0.15}$, however, they are still in the lower absorption spectrum, which is less desirable.

The desorption conditions can be seen in figure 3.9b [30]. At 50 °C the desorption is mostly finished at 1.8 bar and at 80 °C at 5.1 bar. This implies that at 70 °C the desorption could be interpolated to approximately 4 bar, which is a good fit for MGT.

At last, the PCI of $\mathbf{LaNi_{4.9}Al_{0.1}}$ is analysed and depicted in figure 3.10 taken from [6]. With its flat plateau slope, the graph of $LaNi_{4.9}Al_{0.1}$ should not differ severely from the Van't Hoff data.

At 25 °C the absorption is almost finished at a pressure of 1.5 bar. Which is already too high for the MGT application. However, the absorption temperature for 1 bar, taken from the corresponding Van't Hoff plot, lies approximately at 17.5 °C. Therefore, taking to account slightly higher pressures for the absorption, the one bar mark could be reached at around $T_{\text{abs}} = 15$ °C.

Referring to figure 3.10, the desorption pressure corresponding to temperatures of 85 °C and 50 °C ends at approximately 8.1 bar and 3.2 bar, respectively. Therefore, for lower temperatures, within the desorption boundary conditions, a pressure of 4 bar is realistic.

Based on the selection of materials with the PCI plots, $LaNi_{4.85}Al_{0.15}$ and $LaNi_{4.9}Al_{0.1}$

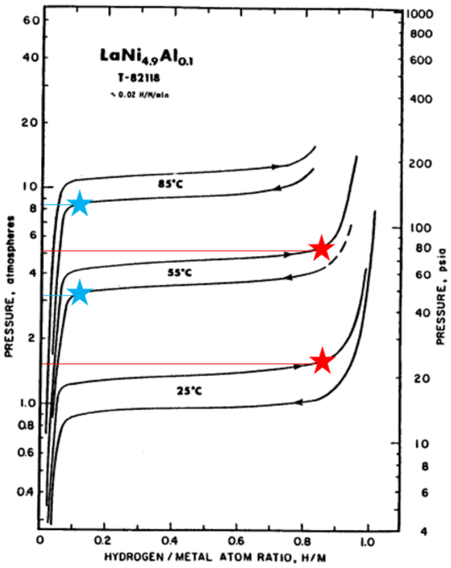

Figure 3.10: PCI of $LaNi_{4.9}Al_{0.1}$ taken from NASA [6]

were chosen as suitable options for MGT, with $LaNi_{4.85}Al_{0.15}$ having better fitting absorption and $LaNi_{4.9}Al_{0.1}$ better desorption conditions.

LTS

For the LTS application, the materials $LaNi_5$, $LaNi_{4.9}Al_{0.1}$ and $FeTi_xMn_y$ are chosen for further examination.

For **$LaNi_5$** only a small amount of temperature curves are available. However, general statements can be deduced from the given data. $LaNi_5$ has a small plateau slope. For example, for 30 °C, taken from the Van't Hoff data, the equilibrium pressure is 2.8 bar. Taking the value at 30 °C from the PCI, the pressure when the majority of H_2 is converted is around 3.1 bar. It follows that the discrepancies between the realistic absorption pressures and those predicted by the Van't Hoff diagram are only minimal.

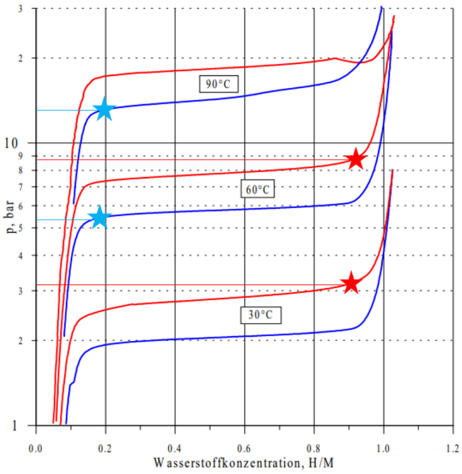

Figure 3.11: PCI of $LaNi_5$ taken from Willers [30]

Therefore, the range presented in table 3.6 can be taken as a good approximation, with slight adjustments to lower temperatures for the given pressures due to the slope.

For the desorption, the same applies in reverse: given the pressure range, the temperatures for the desorption pressures from the Van't Hoff plot are higher than that of the PCI. This makes $LaNi_5$ a good fit for the LTS application covering a broad range of the boundary conditions, however, in the less desired upper temperature range of the desorption and lower temperature range of the absorption.

An analysis of **$\mathbf{LaNi_{4.9}Al_{0.1}}$** was already undertaken in the section covering the PCIs for MGT. However, due to differing pressure ranges, the check for applicability has to be renewed, the graph is depicted anew in figure 3.12 [6].

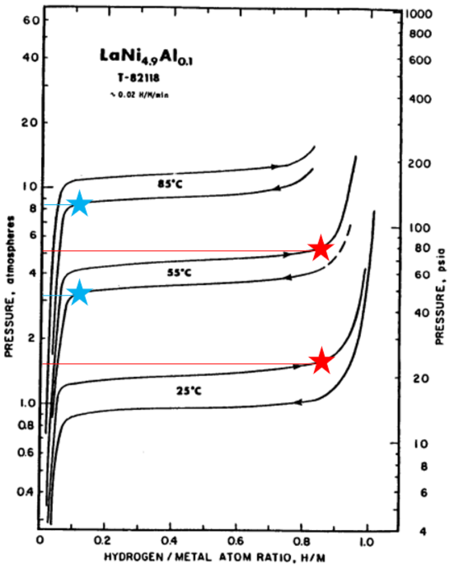

Figure 3.12: PCI of $LaNi_{4.9}Al_{0.1}$ taken from NASA [6]

In comparison to the MGT application, where the absorption temperatures were too low, they now seem to be a good fit for LTS. $p_{\mathrm{abs}}(25\ °\mathrm{C}) = 1.5$ bar lies directly within the boundary conditions and pressures till 30 °C are most likely to be within the ranges as well, making the absorption conditions meeting the requirements quite perfectly, especially when regarding the discussions about temperature changes during the year in subsection 3.2.1.

For the desorption, despite the pressure of 8.1 bar for 85 °C being close to the range, the values are too high. If increased temperature levels were available, $LaNi_{4.9}Al_{0.1}$ could be a good match for LTS.

$\mathbf{FeTi_xMn_y}$ is the last MH evaluated for the LTS application, depicted in figure 3.13 [31]. Especially eye-catching is the plateau slope for absorption and desorption. For example, for 90 °C the difference between beginning and end of the desorption plateau is up to 45 bar.

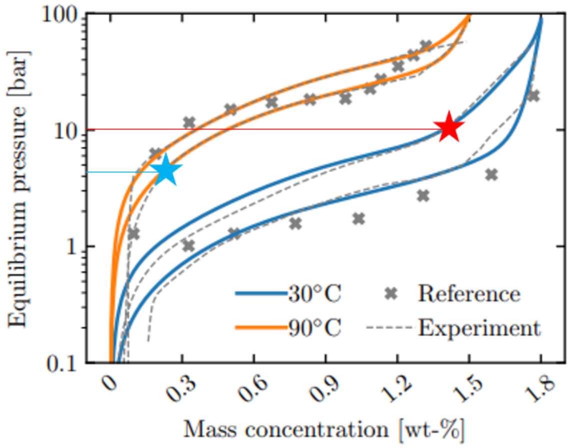

Figure 3.13: PCI of FeTi$_x$Mn$_y$ taken from Bedrunka [31]

The absorption at 30 °C is mostly finished at around 10 bar, which seems promising, however, because of the immense slope, the desorption for 90 °C starts at around 35 bar, but ends at around 4.3 bar. Therefore, the absorption ends at a higher pressure than the desorption, making the reaction an expansion. For that reason, and in contrast to the results of the Van't Hoff discussions, FeTi$_x$Mn$_y$ is not suitable for LTS.

Summarizing the results of the PCI discussion for LTS, based on the examined materials, LaNi$_5$ is the best fit, however, still not meeting the optimal conditions, with its absorption temperatures lower and desorption temperatures higher than anticipated.

sLH2

For the sLH2 application, the Hydralloys C2 and C5 have been selected for further consideration.

The PCI of Hydralloy **C2** measured by Weckerle [32] is presented in figure 3.14.

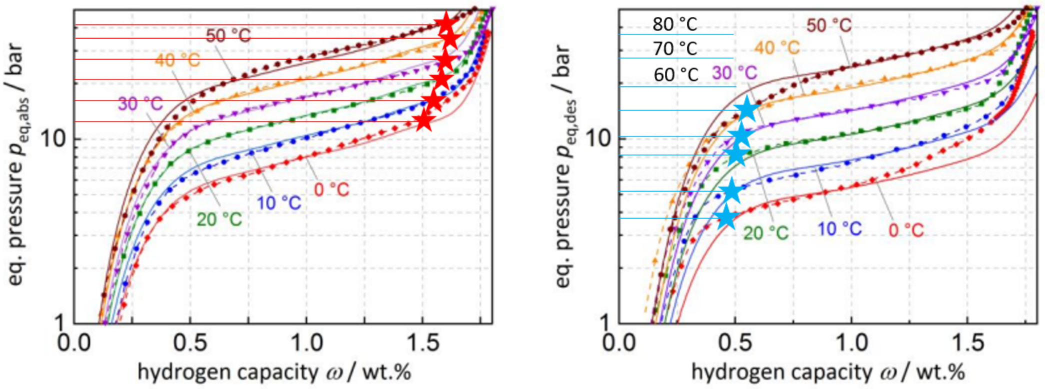

(a) Absorption **(b)** Desorption

Figure 3.14: PCI of Hydralloy C2 taken from Weckerle [32]

The absorption plateau for Hydralloy C2 in 3.14a is significantly curved upwards, leading to a low pressure start of the absorption. However, until the fully absorbed state, for example at 0 °C there is a difference of approximately 10 bar. That difference increases with higher temperatures. For example, for 50 °C, it already has reached a 20 bar difference, which is approximately 5 bar higher, than the corresponding Van't Hoff value. The absorption pressures close to the temperature range are: $p_{\text{abs}}(10\ °\text{C}) = 16$ bar to $p_{\text{abs}}(30\ °\text{C}) = 38$ bar. Therefore, the pressure conditions are only met in the lower than 10 °C area, manifesting Hydralloy C2s incompatibility with the sLH2 application and excluding it from further discussions.

Hydralloy **C5s** PCIs are depicted in figure 3.15 [33]. Similar to Hydralloy C2, a steep absorption plateau slope, increasing with temperature, can be observed.

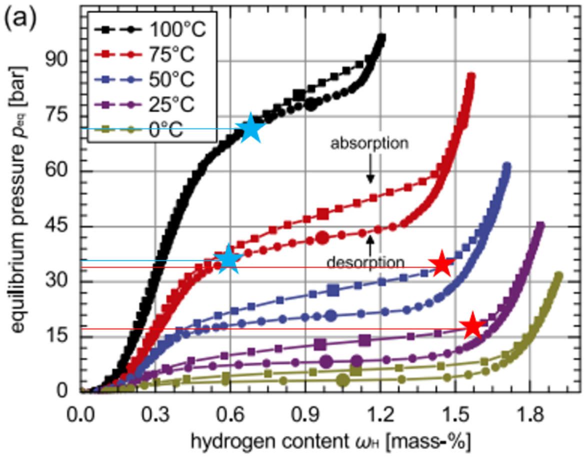

Figure 3.15: PCI of Hydralloy C5 taken from Herbrig [33]

The absorption pressure for 25 °C is around 17 bar and for $p_{\text{abs}}(0\ °\text{C}) = 9$ bar. 17 bar is marginally above the desired pressure range, however, both values imply that for temperatures less than 25 °C, pressures within the desired 10 bar to 16 bar range will be met. Interpolated for 15 °C the corresponding value is around 14 bar. That means, Hydralloy C5s' absorption characteristics meet the temperature requirements in a range from $14 - 16$ bar.

Up to 75 °C, the desorption characteristics are less influenced by the plateau slope. For 100 °C, however, a clear steep up-curving can be seen. The corresponding pressure to the 75 °C curve is 36 bar, showing that higher temperatures need to be provided to reach the $40 - 50$ bar range.

In conclusion, C5 is a better fit for sLH2 than C2, although the temperatures provided for the desorption supposedly need to be higher for a real-life application.

3.2.3 Summary of Material Selection

For further experimental implementation in the following chapter, one out of the three use cases is selected as a representative. The chosen application for this thesis is LTS, with $LaNi_5$ as the selected material. The reason for this decision are the broad temperature ranges and pressure ratios associated with the LTS application that can be examined. In particular, the pressure ratio alternates around 4, embodying the ratios of the other use cases. With regard to the material selection, $LaNi_5$ is thoroughly understood, and examined several times at DLR. Consequently, reactors that only require reactivation are available for the following experimental study.

4 Experimental Setup and Method

This chapter deals with the experimental setup and methods for a thermal compression using metal hydrides. First, a description of the main experimental components: the material $LaNi_5$, the reactor and the water-glycol mixture, and of the test rig will be given. This is followed by the experimental design, where the pressure and temperature ranges for the compression will be presented. Lastly, the analysis method for all the collected data will be explained based on a reference experiment.

4.1 Main experimental components

4.1.1 MH - $LaNi_5$

The reason for the selection of the material, based on the PCI and the Van't Hoff diagram, was already discussed in section 3.2. In this subsection, in table 4.1 general material properties of $LaNi_5$ are presented and following that the characteristics of $LaNi_5$ will be explained in detail.

Table 4.1: Material properties of $LaNi_5$

Designation	Symbol	Value	Unit
Metal Hydride		$LaNi_5$	
Material Form		Powder	
Max. Theoretical Capacity	$w\%_{\mathrm{max}}$	1.399	%
Absorption Enthalpy [30]	$\Delta_{\mathrm{R}}H$	-31.81	$\frac{\mathrm{J}}{\mathrm{mol \cdot K}}$
Absorption Entropy [30]	$\Delta_{\mathrm{R}}S$	112.66	$\frac{\mathrm{J}}{\mathrm{K}}$
Desorption Enthalpy [30]	$\Delta_{\mathrm{R}}H$	31.64	$\frac{\mathrm{J}}{\mathrm{mol \cdot K}}$
Desorption Entropy [30]	$\Delta_{\mathrm{R}}S$	-109.49	$\frac{\mathrm{J}}{\mathrm{K}}$

$LaNi_5$ is a low temperature metal hydride with an equilibrium temperature of 8 °C at 1 bar [30] and is of the structure AB_5. It forms the metal hydride $LaNi_5H_6$. It was already intensively investigated [18] and shows the good properties of AB_5 intermetallic compounds such as little hysteresis, flat plateau, and easy activation [15], making it a good material for hydrogen uptake and compression.

4.1.2 Reactor

The reactor, with the number 4, for the present experiments is shown in figure 4.1 and was designed and produced during a former work at DLR [34]. It consists of 3 tubes in a bundle made of $AlSi_{10}Mg$. Reasons for that are lower density and high thermal conductivity compared to other commonly used materials and, more importantly, a good compatibility with the 3D-print manufacturing process. To separate the MH from the hydrogen gas, an axial filter tube was directly integrated into the three reactor tubes. It can be seen in picture 4.1b at the centre of each tube and in 4.1a extracted from the reactor. To enlarge the surface for heat transfer, additional pins on the outside of the individual tubes, were installed, as shown in figure 4.1b. A screw connection was selected as the type of metal hydride closure and for the H_2 inlet, Swagelok © came to be the best solution. The reactor with all its connections can be seen in figure 4.1c. The hydride material was chosen to be $LaNi_5$ for reasons illustrated in 3.2.2. It was added to the reactor in powder form, outside a glove box. That was possible as the material was not yet activated at the time of insertion, securing safety during the filling procedure. Activation of this material can be performed by cycling the material inside the reactor at moderate conditions of 0 °C at 8 bar. This procedure has already been performed previously to the present thesis.

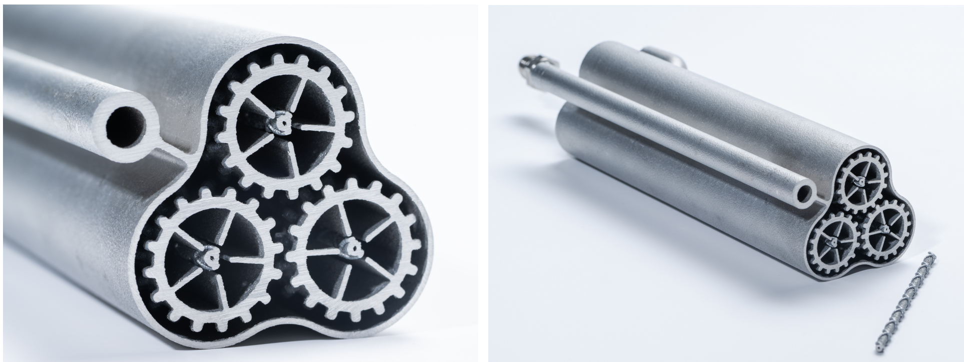

(a) Front-view of the reactor's inlay with filter **(b)** Side-view of the reactor with filter laying in front

(c) Top-view of the reactor with visible fluid and H_2 connections

Figure 4.1: Three different views of the reactor designed by [34]

4.1.3 Heat Transfer Fluid

For the heat transfer fluid, a 50:50 mixture of purified water and mono-ethylene glycol was used. The interpolated data for heat capacity and density are taken from Keller [35].

$$c_{p,\text{fluid}}(T) = (0.0037 \cdot \frac{T}{°\text{C}} + 3.1877)\,\frac{\text{J}}{\text{kg} \cdot \text{K}} \tag{4.1}$$

$$\rho(T) = (-0.0018 \cdot \frac{T^2}{°\text{C}^2} - 0.4757 \cdot \frac{T}{°\text{C}} + 1091.7)\,\frac{\text{kg}}{\text{m}^3} \tag{4.2}$$

Glycol is provided with 98 % purity. It is commonly used in the automotive industry and, referring to appendix A.1, it can be used within a range of approximately −40 °C and unpressured up to 100 °C for a volume fraction of 52 % mono-ethylene glycol.

4.2 Test rig

The test rig was already set up during previous works at DLR and was adjusted to meet the requirements for the demonstration of a thermal compression using metal hydrides in this thesis. In figure 4.2 a picture of the test rig is presented, annotated with essential features, before it was insulated. Figure 4.3 shows the flow chart of the test rig. The reactor is connected to two separated cycles: a gas- and a fluid-cycle, H_2- and water-glycol-cycle, respectively. The data was monitored using a Siemens SPS and illustrated by a WinCC User Interface (UI), which can be seen in figure 4.4. The complete test rig is the same for activation and compression.

The *gas cycle* can be supplied by Argon, and with 30 bar and 300 bar H_2. The gas flow needs to be enabled manually by opening the hand valve of the desired working gas. For the purpose at hand, the 300 bar supply was used. After initiating the stream, another valve V02 needs to be opened, by clicking on the respective button on the WinCC UI, depicted in figure 4.4. V02 works as a second regulator for starting the process, but also as a security to inhibit unwanted gas flow. With the mass flow controller MFC11 hydrogen supply can either be set to a certain pressure, so that only as much gas will be provided to maintain the set pressure. Or it can be set to a constant mass flow, although the flow can not exceed $50\frac{\text{NL}}{\text{min}}$ and can not be less than $1\frac{\text{NL}}{\text{min}}$. Right after the MFC11, a pressure sensor DS2 is attached, measuring pressure levels of the gas within the system. When MFC11 is set on 0 bar or $0\frac{\text{NL}}{\text{min}}$ the controller is closed. The gas temperature within the tubes is measured by thermocouple T08. The connection of the reactor to the gas tubes is regulated by two other hand valves, HV2 and HV_R1.

Figure 4.2: An image of the test rig

For safety purposes, a pressure relief valve ÜV2 is installed between the manual valves, releasing gas when 16 bar is exceeded. It was built after the spring principle, meaning, if the pressure exerted exceeds the spring's force, the valve opens. Opening HV_R1 is the last step to include the reactor in the gas system. This valve needs to be open at all times when the reactor is inserted into the test rig. It can only be closed when the reactor is removed to protect the material from air. A second mass flow controller MFC12 regulates the outflow of gas, in analogy to MFC11, either using a set pressure or operating in mass flow control mode. It is closed when set at 160 bar or $0\,\frac{\mathrm{NL}}{\mathrm{min}}$. After passing another hand-operated valve HV_MFC12, hydrogen is released to the ambient. The vacuum pump VP is all in all shut-off and is only used during flushing or gas change processes. It is linked to the system by a hand valve HV_VP, and pressure levels are measured by pressure sensor DS3. Valve V01, pressure relief valve ÜV 94 bar, mass flow controller MFC13 and hand valve HV_MFC13 are not relevant for the procedure.

During the experiments conducted in this thesis, mass flow controller MFC11 and MFC12 are set to desired absorption and desorption pressures, respectively, so that, when the temperature changes, H_2 is supplied automatically on low pressure levels and released to the ambient on the high pressure level.

The *fluid cycle* consists of two individual water-glycol systems, for heating and cooling purposes. Each consists of one thermostatic bath and is linked to the reactor by outflow valve V03, and inflow valve V05. The temperature of the process fluid is measured close to the reactor outlet and inlet by thermosensors with integrated PT100 elements T101_Aus (=out) and T100_Ein (=in). In the reactor, a thermocouple T10_Tinnen is installed to measure the metal hydrides' temperature. On the outside, two more thermocouples, T12 and T13, are attached to monitor the fluids' temperature in the

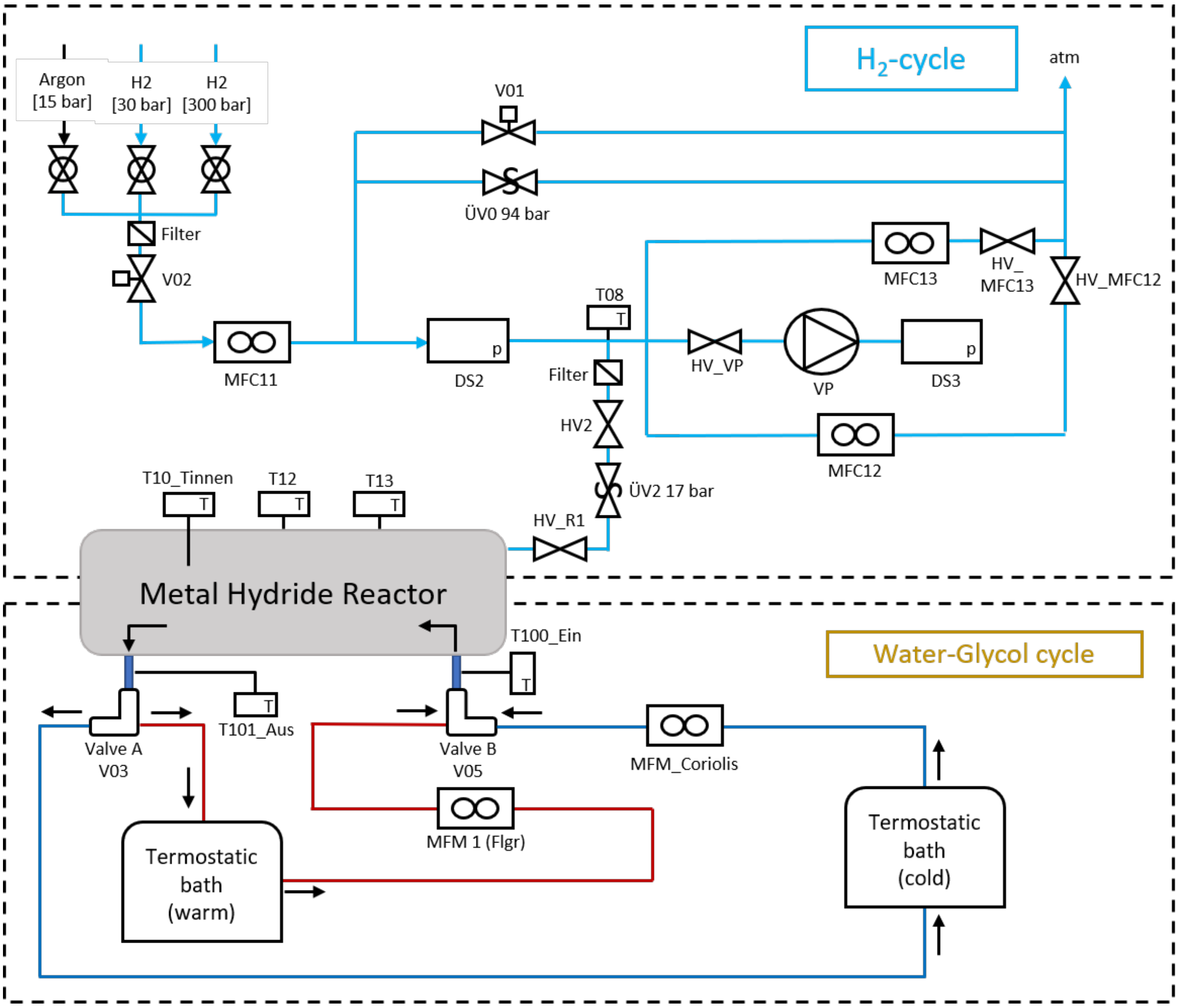

Figure 4.3: Flowchart of the test rig for a thermally driven metal hydride compression

reactor. The cooling bath TT 2200 from the company LAUDA regulates the absorption process and the mass flow is measured by MFC_Coriolis. To change between baths, the three-way valves V03 and V05 need to be switched. The hot bath is a PROLINE AP 890 provided by LAUDA as well, and the mass flow is logged by a mass flow meter MFM 1 (Flgr = impeller). The pump level can be adjusted at the bath, and was set to level four out of eight. Trials of increasing the flow rate, by setting the level to eight, were conducted, however, despite there being a small increase, the change was still too insignificant. In figure 4.2 MFM1 and MFC_Coriolis cannot be seen, since they are installed under the table. This circumstance is marked by a dashed line. Additional technical data regarding the baths are provided in table 4.2.

The lower part of figure 4.4 showcases a representative instance of the WinCC user interface of two desorption/absorption cycles performed in this thesis, with graphs for all measured parameters, starting with the desorption phase.

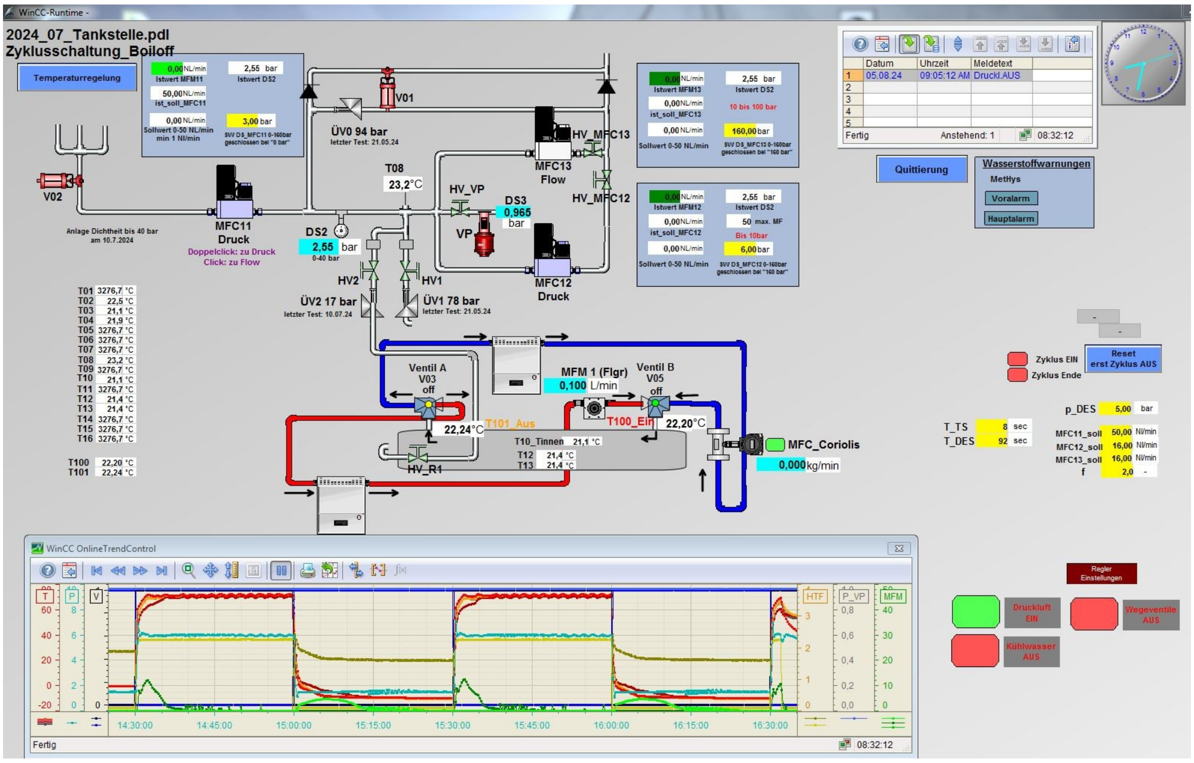

Figure 4.4: WinCC user interface for metal hydride compression test rig

Table 4.2: Additional data regarding the thermostat baths

Abs/Des	Absorption	Desorption
Warming / Cooling process	Cooling bath	Heating bath
Product company	LAUDA	
Product name	TT 2200	PROLINE AP 890
Filling Fluid	50:50 DeMi-Water/Ethylenglycol	
Filling Volume in l	6.5	8
Operating temperature in °C	-35 - 105	-35 - 105

Insulation

After conducting a series of non insulated experiments to get accommodated with the system, a loss of thermal energy to the ambient was observed. Hence, to minimize external, additional energy input, or loss, the reactor and surrounding tubes were covered with insulation materials, including insulation mats, glue and insulating adhesive tape. The new structure of the reactor can be seen in figure 4.5.

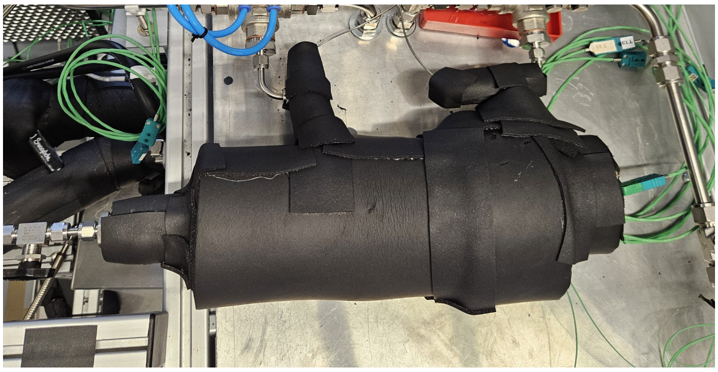

Figure 4.5: MH reactor with added insulation

4.3 Design of Experiments

To ensure experimental reproducibility, the next section outlines the detailed experimental design and preparation for the test runs. To this end, the activation procedure, preliminary tests, insulation measurements and the choice of temperature range and pressure ratio are provided.

Activation

A primary activation was already undertaken when the reactor was first filled in a previous work. However, since the reactor has previously not been in use, a check of the extent of activation to provide optimal, reproducible results of the absorption and desorption processes was conducted. For that purpose, a temperature of $T_{\mathrm{act}} = 0$ °C and the pressure $p_{\mathrm{act}} = 8$ bar chosen, since they provide a flawless absorption. After comparing the results to former works and ensuring the successful completion of the activation, preliminary tests were carried out.

Preliminary test

After assuring reproducible results, first Abs/Des-cycles for the thermal compression were conducted. With the parameter settings of $T_{\mathrm{abs}} = 20$ °C and $p_{\mathrm{abs}} = 3$ bar to $T_{\mathrm{des}} = 70$ °C and $p_{\mathrm{des}} = 6$ bar, 20 min intervals were defined. However, this time frame could not provide a full absorption or desorption for the given settings. Therefore, for the following tests, at least 30 minutes cycle time were determined, to grant comparability between the data while enabling full absorption and desorption potential.

Experimental Design for the Compression

As the goal of the experimental study in this thesis is to provide a proof of concept and to demonstrate a thermal compression using $LaNi_5$ for a boil-off recovery, a variety of experiments have been performed. Figure 4.6a indicates the measured points for the absorption and desorption. Furthermore, the conditions derived from the LTS application in subsection 3.1.2 are included. In order to prove the general concept and the possibilities a thermally driven metal hydride compression can enable, data points outside the given range were tested, based on the BALIS requirements, with different temperature settings and pressure ratios, and will be the focus of the analysis of this study.

In figure 4.6b the minimal ΔT_{min} required to surpass a pressure ratio of 3 is depicted graphically, which is 38 K. In contrast, the actual temperature difference of an example measurement from the experiments, using 70 K, established for the same pressure ratio, is visualized as well, showing the discrepancy between the ideal and real process.

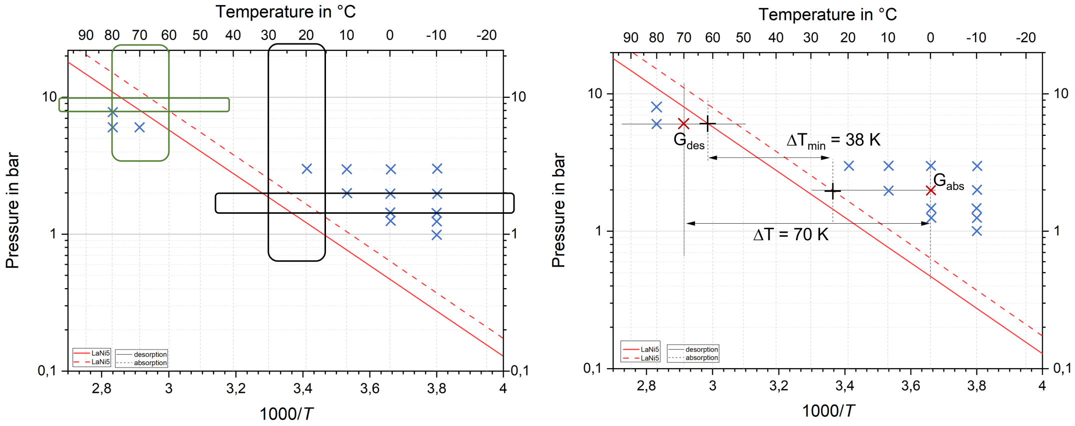

(a) **(b)**

Figure 4.6: Van't Hoff graph of $LaNi_5$ with marked temperature and pressure ranges, black for absorption, green for desorption, for the LTS scenario, with the data points measured in the experimental part in figure 4.6a and the minimal ΔT for a given pressure ratio vs. the actual used ΔT in figure 4.6b

Time ranges were set to 30 minutes for the desorption and depending on the dynamics either 30 or 45 minutes for the absorption. One full cycle includes one absorption and one desorption, one experiment comprises two full cycles. For the analysis, the second cycle is chosen, so that the initial conditions match the experimental conditions. Appendix A.2 contains a matrix detailing the experiments.

To determine the void volume of the reactor, a run of the system using argon was carried out.

4.4 Reference Experiments

In the following section, using a reference experiment, an example of how the data measured in the experiments is analysed is given. Main focus will be on the directly measured parameters: pressure p, mass flow rate $\dot{m}$ and temperature T. Derived from those, the indirect parameters in and out flowing hydrogen mass m, the conversion rate w_t and the thermal energy put in the fluid and based on the hydrogen reaction, Q_{fluid} and

Q_{H_2} , are calculated. Following that, an explanation of how insulated and non insulated experiments are to be compared is given. Furthermore, the concept of a metal hydride compression resulting from heat change is examined against a thermal compression of Argon.

4.4.1 Reference Run

The parameter for the reference run were selected on the basis of good functionality and reproducible data. The settings $T_{\text{abs}} = 0$ °C at $p_{\text{abs}} = 2$ bar and $T_{\text{des}} = 70$ °C at $p_{\text{des}} = 6$ bar represent distances not too close and not too far from the Van't Hoff equilibrium graph, respectively. Relevant data for the calculations are noted in table 4.3 and corresponding graphs are presented in figure 4.8.

Table 4.3: Relevant data and parameter for the analysis

Designation	Symbol	Value	Unit
Reactor			
Mass of the empty Reactor [34]	m_{reactor}	0.325	kg
Mass of the filled reactor with connections [34]	m_{system}	1.029	kg
Void Volume - Total	V_{total}	$1.58 \cdot 10^{-4}$	m^3
Void Volume - Tubes	V_{tubes}	$8.41 \cdot 10^{-5}$	m^3
Void Volume - Reactor	$V_{\text{void, reactor}}$	$7.39 \cdot 10^{-5}$	m^3
MH - $LaNi_5$			
Mass of MH [35]	m_{LaNi_5}	0.345	kg
Absorption Enthalpy [30]	$\Delta_R H$	-31.81	$\frac{J}{mol \cdot K}$
Absorption Entropy [30]	$\Delta_R S$	112.66	$\frac{J}{K}$
Desorption Enthalpy [30]	$\Delta_R H$	31.64	$\frac{J}{mol \cdot K}$
Desorption Entropy [30]	$\Delta_R S$	-109.49	$\frac{J}{K}$
Other data			
Molar Mass H_2	M_{H_2}	2.016	$\frac{g}{mol_{H_2}}$
Ideal Gas Constant	R	8.314	$\frac{J}{mol \cdot K}$

To demonstrate the effect of the *temperature induced compression*, the temperature curves of T10_Innen in the reactor, that of the out-going fluid T101, that of the incoming fluid T100, and the pressure are shown in graph 4.7. The sequence of reactions in figure 4.7a is as followed: first the temperature of the fluid rises induced by switching the three-way valves of the fluid circuit, and as a result, the pressure as well as the temperature in the reactor rise. This process aligns with the principles of metal hydride reactions outlined in the section 2.4: if heat is induced to a MH, the stored hydrogen is being compressed and after adding the reaction heat, H_2 is released. Since the desorption is endothermic and therefore requires heat input, which is taken from the fluid, the curve of the inner temperature T10_Innen, is less than that of the fluid. The graph of the in-flowing temperature is significantly higher than that of the out-flowing fluid, and even higher than that of the metal hydride. The difference of temperature results from the heating process after switching the valve and the endothermic properties of a MH desorption.

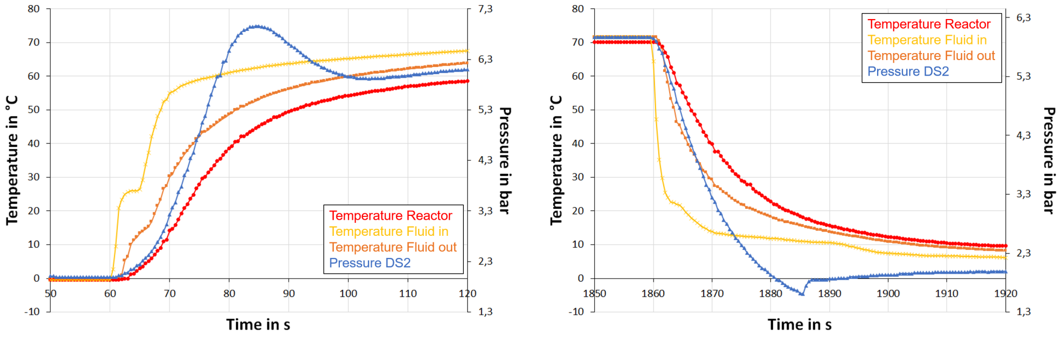

(a) Desorption **(b)** Absorption

Figure 4.7: Pressure and temperature curve of reference run plotted versus each other to show temperature induced compression

In reverse, the same applies during the absorption process presented in figure 4.7b: following the temperature change of the fluid, the temperature of the MH decreases, initiating the absorption process and therefore the pressure in the system decreases. However, because the exothermic absorption releases heat to the ambient, the temperature in the reactor shows a delayed onset of cooling.

The graph of the in-flowing fluid shows a dent during the first 10 seconds of desorption and absorption. This is a result of the reaction time of the regulator of the warming and cooling bath and is not related to the reaction.

Direct Parameter

One full cycle of desorption and absorption starts in the fully absorbed state at $T_{\mathrm{abs}} = 0$ °C and $p_{\mathrm{abs}} = 2$ bar. Switching between the two baths, from cold to warm at $T_{\mathrm{des}} = 70$ °C, initiates the *desorption cycle*. The temperature curve can be seen in figure 4.8a. The pressure rise depicted in 4.8b indicates the immediate pressure increase after the temperature switch. As soon as the pressure exceeds 6 bar, it results in the automatic opening of the mass flow regulator MFC12, depicted in 4.8c, which is set to release hydrogen at $p_{\mathrm{des}} = 6$ bar. Before MFC12 reacts to the increase in pressure, the data captured by pressure sensor DS2, shown in 4.8b, exceeds 6 bar expressed in a sharp peak. After that, the pressure stabilizes around 6 bar. In the first 410 seconds, the majority of H_2 is continually released at the constant desired pressure of 6 bar. This aligns with the time in 4.8a that it takes for the MH to reach the set temperature. Subsequently, when the reactor starts to release the residue, MFC12 is only opened to release in batches, ultimately reaching a mass flow of $0 \frac{\mathrm{NL}}{\mathrm{min}}$. In figure 4.8b that behaviour is reflected by an unstable pressure curve, fluctuating around 6 bar. The *absorption cycle* is initialized

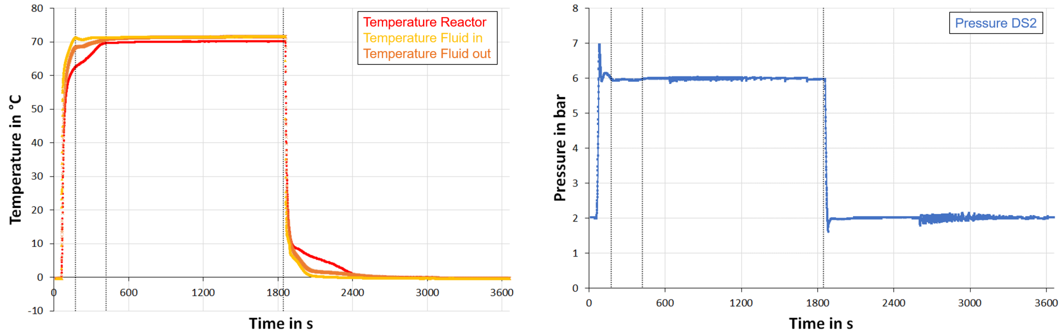

(a) Temperature **(b)** Pressure

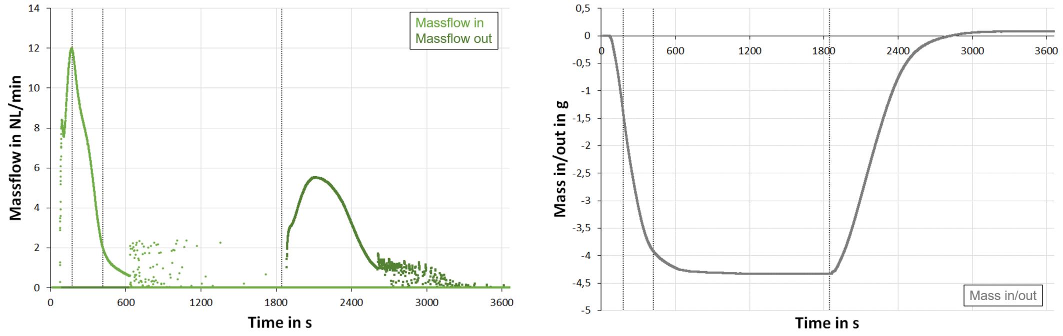

(c) Mass flow **(d)** Integral of mass flow rate

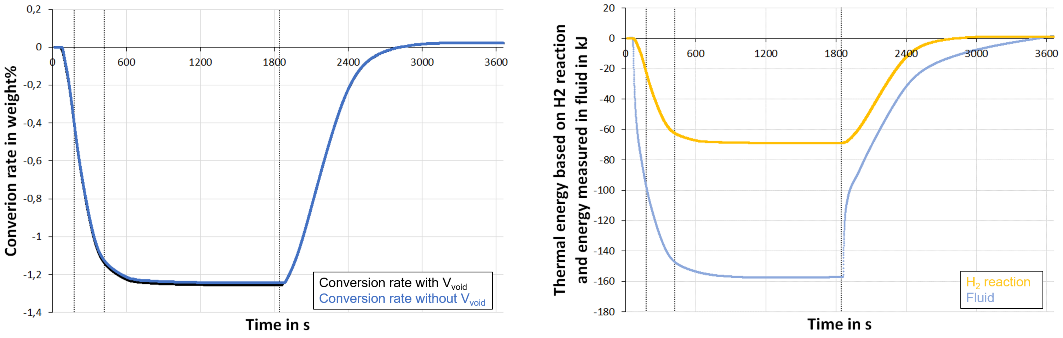

(e) Conversion rate **(f)** Energy Fluid and H_2 reaction

Figure 4.8: Graphs of the direct and indirect parameter for the reference experiment for the parameter settings of $T_{\mathrm{des}} = 70$ °C, $p_{\mathrm{des}} = 6$ bar and $T_{\mathrm{abs}} = 0$ °C $p_{\mathrm{abs}} = 2$ bar

by a switch of the fluid cycle to the cold bath at $T_{\mathrm{abs}} = 0$ °C. Consequently, first, the desorbed hydrogen in the void volume of the system is absorbed by the hydride, leading to a drop in pressure. When the set pressure of 2 bar is reached, MFC11 opens its valve, generating a constant mass flow rate of H_2 to maintain the pressure. When hydrogen is nearly fully absorbed, similar to the desorption process, the valve stops to remain open, due to technical reasons, and the pressure in 4.8b starts fluctuating.

Indirect Parameter

Derived from the direct parameters, the hydrogen mass $m_{\mathrm{H_2,abs}}$ entering and leaving the system, the conversion rate $w\%$, and the thermal energy transferred to the fluid, Q_{fluid}, as well as released by the hydrogen reaction, $Q_{\mathrm{H_2}}$, are calculated.

The conversion rate is determined by the ratio of the mass of the absorbed hydrogen to that of the metal hydride, presented in equation 4.3. The data are plotted in figure 4.8e.

$$w\% = \frac{m_{\mathrm{H_2,abs}}}{m_{\mathrm{MH}}} \cdot 100\% \tag{4.3}$$

To determine the value of $m_{\mathrm{H_2,abs}}$, depicted in figure 4.8d, the mass of hydrogen in the void volume is subtracted from the total mass of hydrogen presented in equation 4.4.

$$m_{\mathrm{H_2,abs}} = m_{\mathrm{H_2,tot}} - m_{\mathrm{H_2,void}} \tag{4.4}$$

The mass of hydrogen in the void volume of the reactor is calculated using the ideal gas law with the fixed value of the void volume of the reactor, which is calculated with equation 4.5.

$$V_{\mathrm{void,reactor}} = V_{\mathrm{void,tot}} - V_{\mathrm{void,tubes}} \tag{4.5}$$

For the given reactor, that value is $V_{\mathrm{void,reactor}} = 8.2 \cdot 10^{-5}\ \mathrm{m}^3 = 82\ \mathrm{mL}$. With that value given, the calculation of $m_{\mathrm{H_2,abs}}$ in equation 4.4 has all required variables.

Equation 4.6 provides the calculation for the maximum theoretical capacity.

$$w\%_{\mathrm{max}} = \frac{m_{\mathrm{H_2}}}{m_{\mathrm{MH}}} \cdot 100\% = \frac{n_{\mathrm{H_2}}}{n_{\mathrm{MH}}} \cdot \frac{M_{\mathrm{H_2}}}{M_{\mathrm{MH}}} \cdot 100\% \tag{4.6}$$

For $LaNi_5H_6$ the maximal theoretical capacity is:

$$\begin{aligned} w\%_{\mathrm{max}} &= \frac{n_{\mathrm{H_2}}}{n_{\mathrm{MH}}} \cdot \frac{3 \cdot M_{\mathrm{H_2}}}{M_{\mathrm{La}} + 5 \cdot M_{\mathrm{Ni}}} \cdot 100\% \\ &= \frac{1\ \mathrm{mol}}{1\ \mathrm{mol}} \cdot \frac{3 \cdot 2.016\ \frac{\mathrm{g}}{\mathrm{mol}}}{138.91\ \frac{\mathrm{g}}{\mathrm{mol}} + 5 \cdot 58.69\ \frac{\mathrm{g}}{\mathrm{mol}}} \cdot 100\ \% \\ &= 1.399\ \% \end{aligned}$$

As a concluding step, the energy content of both the fluid and H_2 are quantified. The means to calculate the fluid's energy are provided in equation 4.7 and for the hydrogen reaction in equation 4.8. The $c_{p,\mathrm{fluid}}$-value of the fluid is taken from the equation presented in 4.1.3.

$$\dot{Q}_{\text{fl}} = \dot{m}_{\text{fl}} \cdot c_{p,\text{fl}} \cdot \Delta T_{\text{fl}} = \dot{m}_{\text{fl}} \cdot c_{p,\text{fl}} \cdot (T_{\text{fl, out}} - T_{\text{fl, in}}) \tag{4.7}$$

The summed up transferred thermal energy, Q_{fl}, in the fluid is shown in figure 4.8f as the blue graph.

The energy released by the reaction of hydrogen can be derived from equation 4.8 using the definition of the amount of substance and the enthalpy of the reaction. The summed up reaction energy is depicted in figure 4.8f as the yellow graph.

$$\dot{Q}_{\text{H}_2} = \dot{n}_{\text{H}_2,\text{abs}} \cdot \Delta H_{\text{abs}} = \frac{\dot{m}_{\text{H}_2,\text{abs}}}{M_{\text{H}_2}} \cdot \Delta H_{\text{abs}} \tag{4.8}$$

All graphs 4.8d - 4.8f during the first 410 seconds of the desorption follow a steep, nearly constant slope, reaching its inflection point when the mass flow is on its peak at 175 s. When the mass flow becomes sporadic, the curves slowly concave up, reaching a plateau.

When the absorption starts after 1845 s, for figure 4.8d, 4.8e and the energy of hydrogen in figure 4.8f, a curvature upwards with a turning point at the mass flow peak is seen. When the mass flow becomes less, the curves concave down, reaching the point they started, the absorbed state, here corresponding to the x-axis with a value of 0.

The energy measured within the fluid, in figure 4.8f, shows a profoundly steep gradient for the first 30 s after the switch occurs to the cold bath with the absorption temperatures. When the heat is decreased to the point where the absorption starts, the energy curve's incline decreases to a lower positive slope. The reason for that can be found in the exothermic behaviour of the absorption. Added to the cold thermal energy of the fluid, is the heat of the absorption, resulting in the decreased incline, and ending the Abs/Des cycle at 0 kJ after 3600 s. A more detailed explanation of the gap between the energy based on the H_2 reaction and that of the fluid is provided in subsection 4.4.3.

4.4.2 Insulation effect

Upon the conclusion of the first experiments, an insulation was applied to the reactor and the surrounding tubes, to mitigate heat dissipation. Figure 4.9 illustrates the discrepancies observed following the installation of the insulation. The most significant impact was made regarding the energy in the fluid, depicted in figure 4.9c. While the graph of the non insulated run continues to fall when the desorption pressure is reached, meaning, more energy is put into the system, the insulated graph reaches a plateau and stays constant until the absorption starts.

The total difference in heat loss can be observed at the end of the absorption cycle.

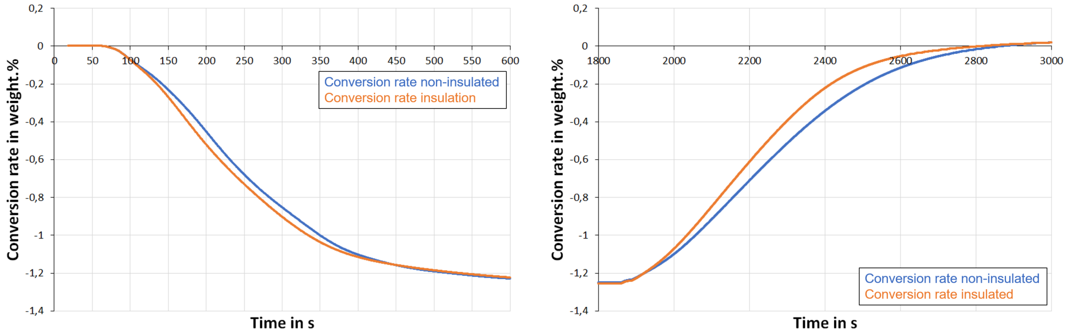

(a) Conversion rate of the desorption insulated and non-insulated

(b) Conversion rate of the absorption insulated and non-insulated

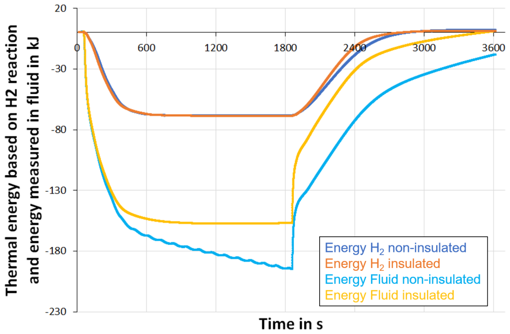

(c) Energy in the fluid and the gas insulated and non-insulated

Figure 4.9: Difference of the graphs before and after applying insulation

While the insulated graph reaches 0 kJ, implying, that the same amount of energy was supplied during the desorption as gained during the absorption, the non-insulated graph does not return to the x-axis, indicating energy loss during the process. Another small impact was made regarding the dynamics of the desorption and absorption, depicted in figure 4.9a and 4.9b, respectively. The incline of the graph for the insulated run, is slightly steeper than that of the non-insulated, signifying enhanced dynamics of the process. Because of the insulation, the reactor heats up faster to the target temperature, resulting in the explained behaviour.

The comparison of insulated and non-insulated experiments has shown that despite improvements in the dynamics, the differences are not significant. Therefore, a comparison of insulated and non-insulated runs is possible. This excludes a thermal analysis, since the losses are too severe.

4.4.3 Argon effect

An explanation of the principle of a thermal compression using metal hydrides was given in section 2.4. To illustrate that the rise in pressure was not a response to the effect of the ideal gas law, equation 4.9:

$$pV = nRT \tag{4.9}$$

the graphs of the compression resulting from the temperatures $T_{\text{abs}} = 0$ °C and $T_{\text{des}} = 70$ °C or Argon and for the MH are compared. They are both depicted in figure 4.10a.

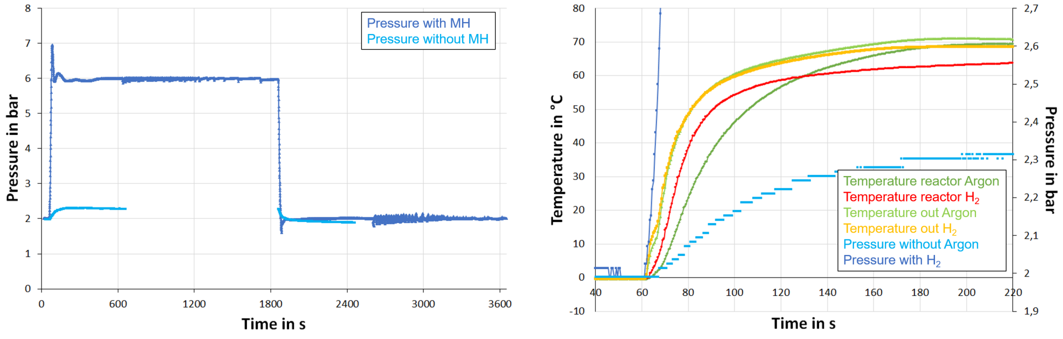

(a) **(b)**

Figure 4.10: In 4.10a: the comparison of a thermal compression with Argon and a metal hydride at the temperatures of $T_{\text{abs}} = 0$ °C and $T_{\text{des}} = 70$ °C and in 4.10b: the pressure and temperature curve of the reference run plotted next to the run using argon

The desorption pressures stabilize at $p_{\text{des, Argon}} = 2.31$ bar and $p_{\text{des, H}_2} = 6$ bar, visualizing evidently, that for H_2 a compression outside the ideal gas law took place.

This claim can be supported with calculations using the ideal gas law. Derived from equation 4.9, an equation with that the pressure of every ideal gas at a given temperature and vice versa can be calculated.

$$\frac{p_2}{p_1} = \frac{T_2}{T_1} \tag{4.10}$$

For the case at hand, using equation 4.10 with the parameter of $T_1 = 0$ °C, $T_2 = 70$ °C and the known pressure $p_1 = 2$ bar that value is as follows:

$$\begin{aligned} p_2 &= \frac{p_1}{T_1} \cdot T_2 = \frac{2 \cdot 10^5 \text{ Pa}}{273.15 \text{ K}} \cdot 343.15 \text{ K} \\ &= 2.51 \text{ bar} \end{aligned}$$

The calculated value differs approximately 0.2 bar from the measurement. This is based on the temperature differences of the pipes and the reactor. The pipes have a constant temperature of approximately 23 °C. This differs from the temperatures of the reactor. However, the pressure is measured in the tubes, therefore, the pressure of the ambient temperature H_2 and that of the metal hydride reaction H_2 is measured. This results in a lower pressure, than in an ideal situation, where all H_2 is on a temperature of 70 °C.

Especially interesting is a more narrow comparison of the temperature and pressure curves of argon and the reference experiment. The comparison can be seen in figure 4.10b. While in the long run, the temperatures in and out for both gases converge to the same value of 70 °C, with a small tolerance of 0.02 K resulting from the calibration, a clear discrepancy between the curves gradients of the temperature within the reactor can be seen. While the temperature for the argon run, in red, approaches a similar value as the fluids' temperatures, the darker green curve starts with a higher positive gradient. However, within the examined frame, it does not reach the desorption temperature of 70 °C, ending at a temperature of 64 °C. This difference can be explained with the principles of the endothermic metal hydride desorption process.

The gap between the energy in the fluid and that of the hydrogen reaction results from the heat energy needed to change the temperature of the MH, the fluid, and the reactor, with and without the connections. A graphic visualization of those calculations is given in figure 4.11a. In total, the approximated ideal amount of energy needed to heat the system with connections by ΔT = 70 K, is 80 kJ. A similar value is measured when running the experiment with argon, where no energy resulting from the H_2 reaction is measured. Ideally the value of the maximum energy put into the fluid should be equal to the calculated results, however, since the exact reaction enthalpies are not known, values differing within a 10 % range are a good estimation.

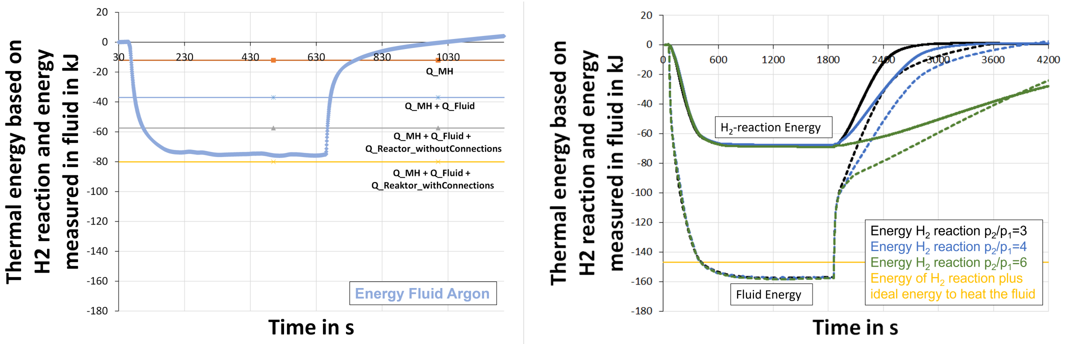

(a) Heat energy needed to change the fluids' temperature from 0 °C to 70 °C, with different heat consuming factors

(b) Energy in the fluid and that of the hydride reaction for the temperatures from 0 °C to 70 °C

Figure 4.11: Thermal energy of the argon run and corresponding H_2 reaction with a ΔT of 70 K at variable pressure ratios

Depicted in figure 4.11b are the graphs of the thermal energy of the experiments with a ΔT = 70 K. Additionally, plotted is a yellow line marking the summed up maximal thermal energy of the hydrogen reaction plus the calculated value of 80 kJ, which is necessary to heat up the system. As before, the line is not identical with the measured graphs of the fluid, however, it is still in a sufficient range, where differences can be well explained, with thermal losses during the process.

5 Results and Discussion

This chapter reviews and analyses the results of the experiments carried out as part of this thesis. Especially the influence of different pressure ratios, $\frac{p_{\text{des}}}{p_{\text{abs}}}$, for constant absorption and desorption temperatures, the impact of different absorption and desorption temperatures for a constant pressure ratio $\frac{p_{\text{des}}}{p_{\text{abs}}}$, and the demonstration of a H_2 absorption below 1 bar as a result of a constant mass flow are discussed. The results section concludes a discussion of the energy balance of the thermal compression using metal hydrides, and a small cost analysis based on the cycling time.

5.1 Constant Temperature

In the following section, experiments with constant absorption and desorption temperatures and therefore non-changing ΔT values are discussed. The changing variables are the absorption and desorption pressures and therefore the pressure ratios $\frac{p_{\text{des}}}{p_{\text{abs}}}$. For each temperature difference, the graph of the pressure, mass flow, conversion rate and the energy is presented and analysed in the following. To distinguish the different runs, they are colour coded. Thus, all graphs with the same colour, or different shade of the colour, regardless of the line structure, belong to one measurement.

5.1.1 T_{des} = 70 °C and T_{abs} = -10 °C

In figure 5.1, the graphs of mass flow, pressure, conversion rate and that of the energy from the hydrogen reaction and of the fluid are shown for the parameter settings of $T_{\text{des}} = 70$ °C, $T_{\text{abs}} = -10$ °C with $\Delta T = 80$ K. The desorption pressure is identical for all runs, that is $p_{\text{des}} = 6$ bar. The changing factor in this run is the absorption pressure and therefore the pressure ratio, covering ratios between 2 and 6.

In diagram 5.1a, the **mass flow** graphs for one cycle are depicted. When the 3-way valve is switched to access the warm bath, the desorption process starts and the pressure in the system starts rising. When exceeding the 6 bar mark, mass flow regulator MFC12 is opened and the accumulated H_2 is released, resulting in a steep incline of the graph with a sharp peak. After the first amount is discharged, the mass flow decreases, since only the remaining H_2 from the reactor is being desorbed. When the reactor is becoming empty, the pressure in the system only rises marginally, keeping it stable at around 6 bar, and therefore, there is no need for the valve to be constantly open. Hence, the

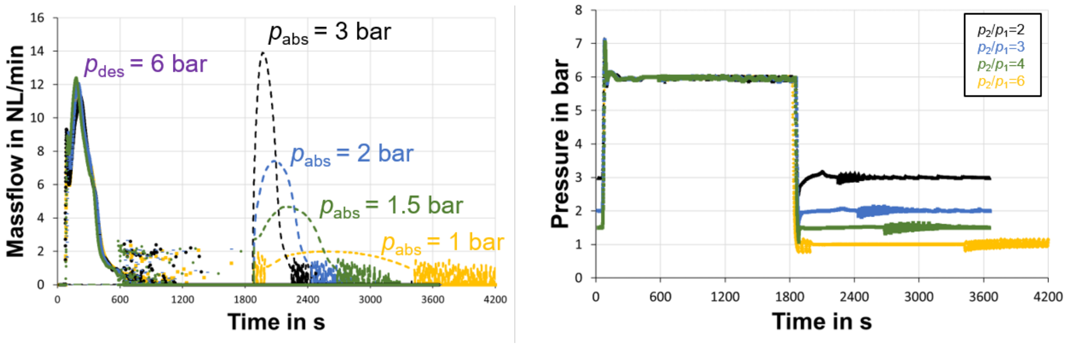

(a) Mass flow

(b) Pressure

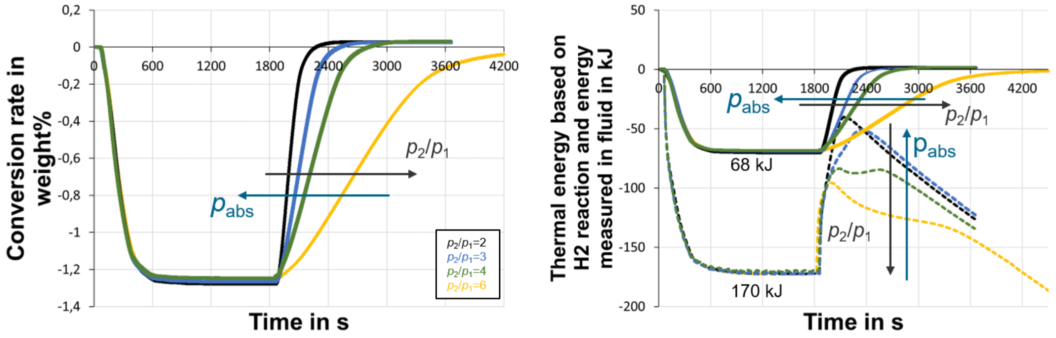

(c) Conversion rate

(d) Energy: H_2-reaction and fluid

Figure 5.1: Graphs of the direct and indirect parameters for $T_{des} = 70$ °C, $T_{abs} = -10$ °C and $\Delta T = 80$ K

fluctuations in the mass flow rate indicate a nearly empty reactor and therefore the end of the desorption process. The desorption graphs demonstrate consistent behaviour for identical conditions, indicating high reproducibility in dynamics. The peak height on average is $12\frac{\text{NL}}{\text{min}}$ and the flows start fluctuating at approximately 600 s.

The difference in peak height and the dynamic behaviour of the absorption runs, depend heavily on the absorption pressure and the distance of the set point to the Van't Hoff equilibrium curve. For increasing absorption pressures, that distance gets higher, leading to more optimal absorption conditions and therefore to higher peaks and enhanced dynamic behaviour. In accordance to that, the mass flow fluctuations in figure 5.1a of high peaks start earlier than those for lower ratios, indicating increased dynamics and an earlier end of the absorption process.

In real life applications, where symmetrical processes are preferred, the peaks of desorption and absorption should be of the same height to provide identical dynamics. For the given temperature setting, this appears to happen for an absorption pressure between 2 and 3 bar.

The first thing that can be seen quite well in the diagram depicting the measured **pressures**, figure 5.1b, is that all the desired pressures are reached with the given pressure and temperature settings. Especially for the desorption, the patterns of the graph are overlapping well. The pressure fluctuations all start at the same time at approximately 600 s, matching the mass flow fluctuations well. The foremost difference between the graphs is the start of the pressure fluctuations during the absorption. With lower absorption pressures, the instabilities appear later than for the higher ones. This is consistent with the graphs of the mass flow in figure 5.1a and the dynamic behaviour of the reaction explained above.

As for the **conversion rate** in figure 5.1c, again, similar patterns in terms of dynamics and reproducibility are observed. At first, according to the constant mass flow, the desorption graphs show a steep decline, and end at the constant value of 1.25 % at 600 s. Until the absorption starts, no significant change can be observed. The absorption patterns of the graph differ depending on the ratios: low ratios result in faster absorption than higher ratios. The end of the absorptions are indicated by the graph reaching 0 %. The conversion rate therefore clearly illustrates the end of the desorption and absorption, compared to the mass flow and pressure graphs. Moreover, visualizing the dynamic differences between the ratios evidently.

The desorption patterns of the **thermal energy** based on the H_2 reaction and that measured in the fluid in figure 5.1d perfectly align. The energy increases up until 600 s reaching a constant value of 68 kJ for the energy of the H_2 reaction, the straight lines, and 170 kJ in the fluid, the dashed lines. Therefore, for the same temperature difference, ΔT = 80 K, the thermal energy needed to change the temperature of the system is ΔQ = 102 kJ. The thermal energy of the H_2 reaction shows, as expected, similar absorption patterns as the conversion rate. The pattern of the fluid's thermal energy, requires more investigation. When the absorption starts at 1800 s, it starts as expected with an incline, since the system is being cooled. However, depending on the ratio, for higher ratios sooner or for lower ratios later, the inclining graph shows a sudden change in slope. Moreover, for higher ratios, the loss is more significant than for lower ones. This is a result of the absorption temperature being below 0 °C. The influence of the surrounding room temperature appears to have an increased impact on the energy balance of negative temperatures. Since runs with high absorption pressures are of enhanced dynamics, that influence of the environment impact the fluid later and is decreased compared to low pressure runs.

5.1.2 T_{des} = 70 °C and T_{abs} = 0 °C

In the following, the results of the measurements at T_{des} = 70 °C, T_{abs} = 0 °C with ΔT = 70 K, covering the pressure ratios of 3, 4, and 6 are discussed. The corresponding graphs can be seen in figure 5.2. As expected, the graphs show similar behaviour as the graphs discussed in subsection 5.1.1. Therefore, no detailed explanation will be given for the analogous patterns.

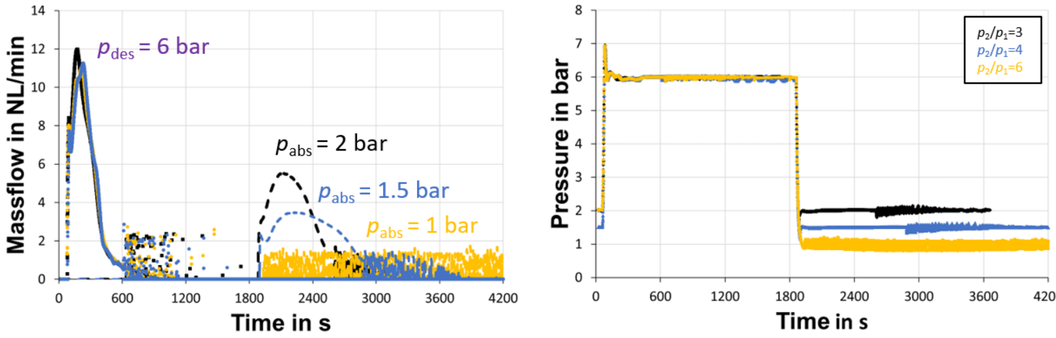

(a) Mass flow **(b)** Pressure

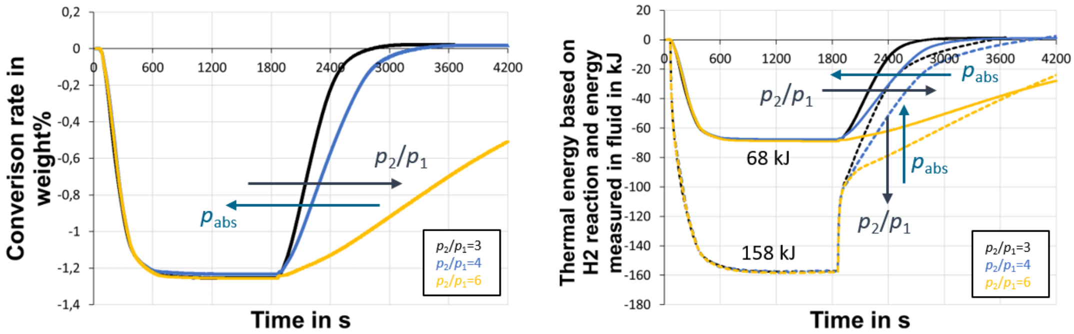

(c) Conversion rate **(d)** Energy: H_2-reaction and fluid

Figure 5.2: Graphs of the direct and indirect parameters for $T_{\text{des}} = 70$ °C, $T_{\text{abs}} = 0$ °C and $\Delta T = 70$ K

Figure 5.2a visualizes the graph of the **mass flow**. The desorption conditions are the same as those above, however, the average peak height is slightly less than $12\frac{\text{NL}}{\text{min}}$ and the beginning of the mass flow fluctuations are a little later than 600 s. The small difference can be explained to the cyclical behaviour of the experiments.

The main difference can be observed in the yellow graph of the absorption run. Absorption pressures of 2 and 1.5 bar already show smaller peaks than the runs at −10 °C, however, for the absorption pressure of 1 bar at 0 °C, no constant mass flow was measured at all, showing the graph fluctuating only. The reason why an absorption, even though with slow dynamics, was possible at −10 °C and not at 0 °C is the increased absorption temperature. The distance of the set point to the equilibrium curve is decreased, resulting in reduced dynamics. For the same reason, the comparatively smaller peaks can be explained.

The same phenomenon during the absorption can be seen in figure 5.2b for the yellow graph with a **pressure** ratio of 6. As expected, the beginning of the pressure fluctuations align with those of the mass flow, showing the different dynamics of the runs. Since the absorption conditions for the yellow graph are not suitable for the given material, no constant pressure was able to be reached.

The desorption patterns of the **conversion rate** in figure 5.2c show again that, for the same temperature difference, the graphs overlap well and have the same maximum conversion rate of approximately 1.24 %. However, for ΔT = 70 K it is slightly less than for ΔT = 80 K, showing the importance of the absorption conditions. The absorption dynamics show the expected behaviour, where increased p-ratios result in reduced dynamics.

The results of the **thermal energy** of the H_2 reaction, the straight lines in figure 5.2d, align with the conversion rate. Since the same reactor is used, the same amount of hydrogen can be absorbed, resulting in the same value of 68 kJ.

Since the ΔT is reduced, the amount of energy that is transferred into the fluid to heat the system is less as well, approximately 160 kJ. The biggest visual difference can be seen in the change of slope during the absorption. For 0 °C, the influence of the environment appears not to be significant enough to result in a thermal loss, having a good impact on the energy balance.

Concluding, for the given material choice, −10 °C appears to be the upper limit to conduct an absorption at 1 bar and ΔT = 80 K still enables fast dynamics for a pressure ratio of 4.

5.1.3 T_{des} = 80 °C and T_{abs} = -10 °C

In the following, the results of the measurements at T_{des} = 80 °C, T_{abs} = −10 °C with the highest ΔT of 90 K, covering the highest and lowest pressure ratios of 2 and 6 are discussed. The corresponding graphs can be seen in figure 5.3.

In figure 5.3a, the impact of different desorption conditions on the **mass flow** are obvious. The black graph, with p_{des} = 6 bar, shows fluctuations significantly earlier than 600 s compared to the runs at 70 °C presented in the subsections before. With regard to the different desorption pressures, the higher the desorption pressure, the closer the set point to the equilibrium curve, the poorer the dynamics and the smaller the peak. The same applies to the absorption vice versa, as explained above.

For different desorption and absorption conditions, the desired **pressures**, depicted in figure 5.3b are reached perfectly. Even though, as expected, the fluctuations start earlier with a lower pressure ratio.

The **conversion rate**, in figure 5.3c for the desorption differs for the different reaction conditions. The black graph, p_{des} = 6 bar, shows enhanced dynamics and a higher conversion rate of 1.29 % than the blue graph, p_{des} = 8 bar, with $w\%_{\mathrm{max}}$ = 1.25 %. For the absorption dynamics, the same can be said: the reaction of the blue graph ends significantly later than for the black graph. Even though both graphs show larger conversion

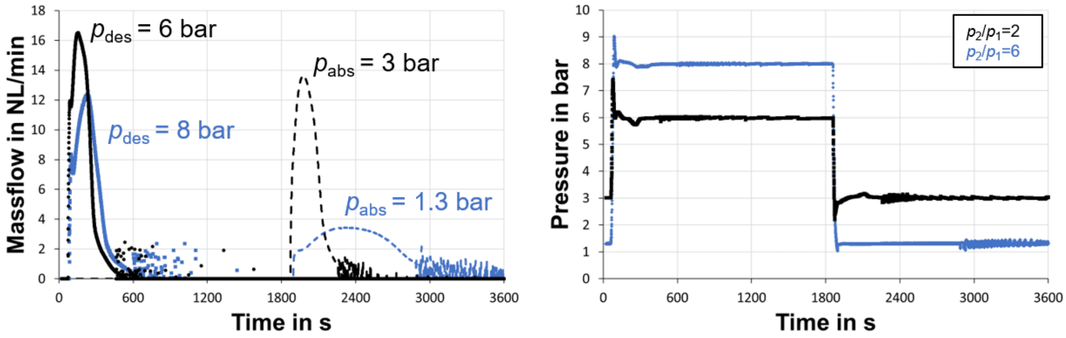

(a) Mass flow

(b) Pressure

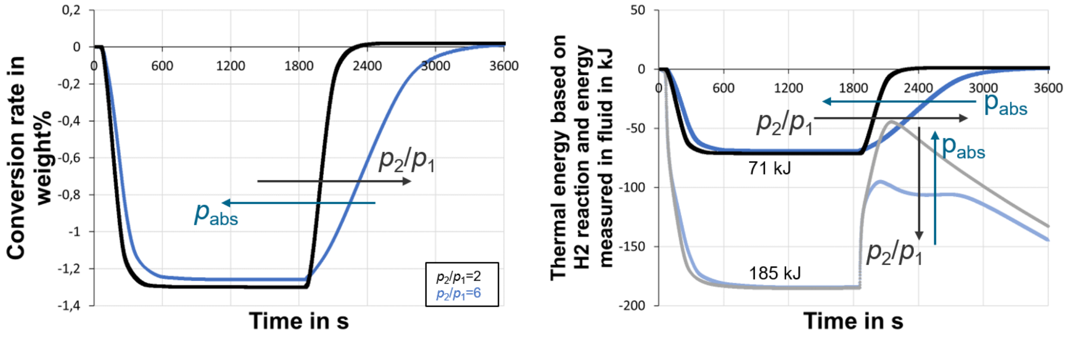

(c) Conversion rate

(d) Energy: H_2-reaction and fluid

Figure 5.3: Graphs of the direct and indirect parameters for the T_{des} = 80 °C, T_{abs} = −10 °C and ΔT = 90 K

rates than the runs described before, the black graph, with the highest ΔT and the lowest pressure ratio, enables maximal conversion due to optimal reaction conditions.

Aligning with the increased hydrogen mass due to the maximal conversion rate and the temperature difference of 90 K, the **thermal energy** from the H_2 reaction increases to 71 kJ and that of the fluid to 185 kJ. As seen in subsection 5.1.1, the same phenomenon for temperatures below 0 °C runs during the absorption can be observed.

5.1.4 T_{des} = 70 °C and T_{abs} = 10 °C

In this subsection, the results of the measurements at T_{des} = 70 °C, T_{abs} = 10 °C with a ΔT of 60 K, covering the pressure ratios of 2 and 3, are discussed. In contrast to the other runs, this run is non-insulated. Since the energy input is influenced by losses, the graph of the thermal energy will not be presented. The corresponding graphs can be seen in figure 5.3.

As expected, the peaks of the **mass flow** in figure 5.4a are of similar behaviour as before. The desorption peak is $12 \frac{\text{NL}}{\text{min}}$ and the fluctuations start approximately at 600 s. For the absorption, the higher the pressure the higher the peak and the dynamics. The blue graph of the desorption shows a small kink, however, this can be explained with

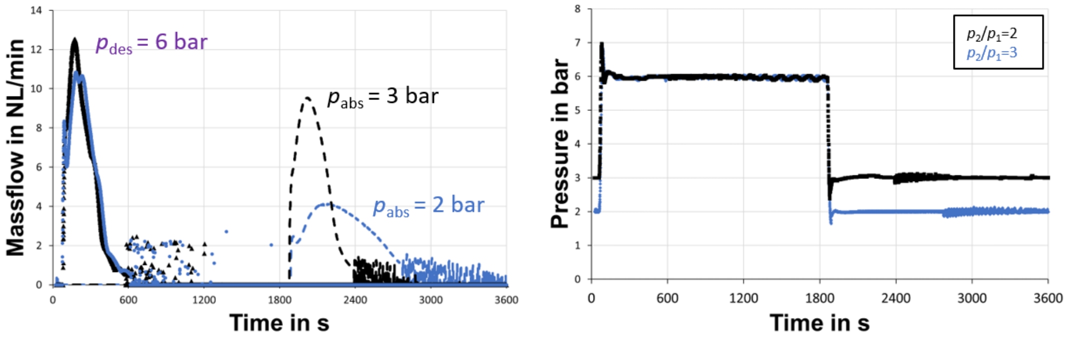

(a) Mass flow **(b)** Pressure

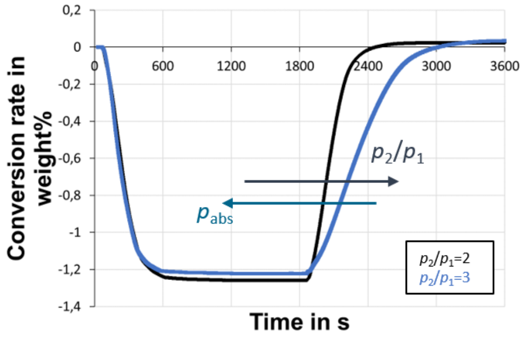

(c) Conversion rate

Figure 5.4: Graphs of the direct and indirect parameters for the $T_{\text{des}} = 70$ °C, $T_{\text{abs}} = 10$ °C and $\Delta T = 60$ K

random errors.

The foreseen patterns can be observed for the **pressure** graph in figure 5.4b.

Due to the error and the reduced dynamics of the blue graph, with a ratio of 6, the **conversion rate** in figure 5.4c has a smaller maximal value, than the black graph with $\frac{p_{\text{des}}}{p_{\text{abs}}} = 2$, 1.22 % and 1.25 % respectively. However, even though the system was not insulated, no major differences to insulated runs, excluding the thermal energy, can be observed.

Concluding this subsection, it can be stated that in this setup, a temperature difference of 60 K is sufficient for a pressure ratio smaller than 3.

5.1.5 Temperature analysis

For one representative run with the constant temperatures of 70 °C and −10 °C, a detailed analysis of the temperature profiles, shown in figure 5.5, is presented.

It can be observed that the desorption temperatures for the out-flowing fluid and in the MH, in figure 5.5a, show the same characteristics as the graph in the reference run, discussed in section 4.4. Moreover, since the conditions for the desorption are the same,

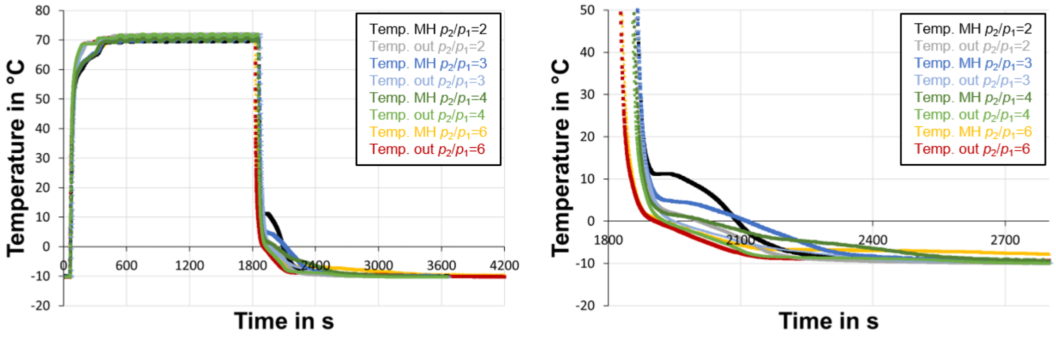

(a) Full graph **(b)** Absorption

Figure 5.5: Temperature graphs of the run with $T_{\mathrm{des}} = 70$ °C, $T_{\mathrm{abs}} = -10$ °C and $\Delta T = 80$ K

at $T_{\mathrm{des}} = 70$ °C, $p_{\mathrm{abs}} = 6$ bar, the behaviour of the endothermic kink is, as expected, identical for all the pressure ratios, showing a very good reproducibility.

However, regarding the absorption process in figure 5.5b, differences in the pattern of the kink depending on the absorption pressure can be identified. The lower the pressure ratio, and thus higher the absorption pressure, the higher the temperature at which the exothermic kink appears and the more distinctive the pattern. This distinctiveness is related to the distance of the Van't Hoff equilibrium curve to the given absorption temperature and pressure.

The reason why the black graph starts at a higher temperature than the others is based on the distance to the equilibrium curve. When the equilibrium graph is surpassed, the absorption starts, however, relatively slow. Only after a certain distance to the equilibrium is exceeded, the dynamics are high enough and the absorption process is fully enabled. For higher absorption pressures, that point is reached at higher temperatures than for lower pressures, resulting in the explained phenomenon.

Concluding the aspects influencing the absorption, it can be deducted that at constant temperatures for higher absorption pressures the driving force is increased and therefore, the dynamics are faster, leading to an earlier start and end of the absorption.

5.2 Constant Pressure Ratio

Analogous to section 5.1, the graphs of temperature, mass flow, conversion rate and the energy for a constant pressure ratio $\frac{p_{\mathrm{des}}}{p_{\mathrm{abs}}}$ with different temperatures will be compared and analysed. Some of the graphs presented in this section already appeared in the graphs above. However, in this case, they will be analysed in the different context of pressure ratios. The rules of the colour code will be the same above in section 5.1.

5.2.1 p_{des} = 6 bar and p_{abs} = 2 bar

This subsection deals with the results of the measurements at $p_{des} = 6$ bar, $p_{abs} = 2$ bar with the ratio of $\frac{p_{des}}{p_{abs}} = 3$, covering temperature differences between 70 K and 80 K. The desorption temperature remains at 70 °C, therefore, the changing variable here is the absorption temperature. The corresponding graphs can be seen in figure 5.6.

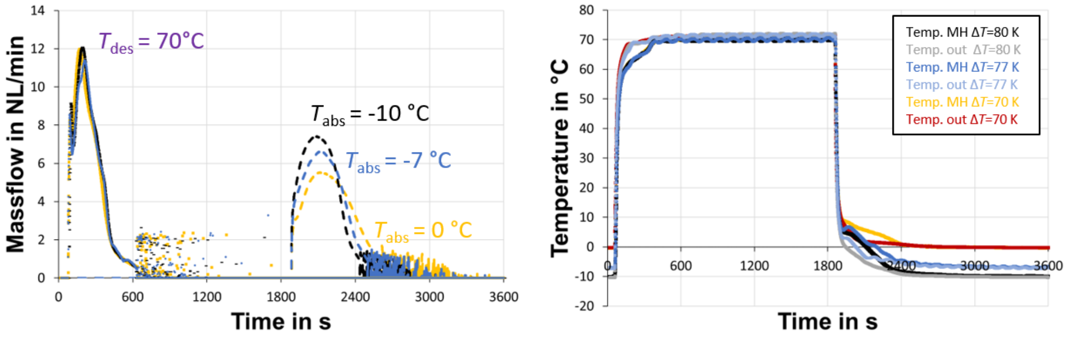

(a) Mass flow **(b)** Temperature

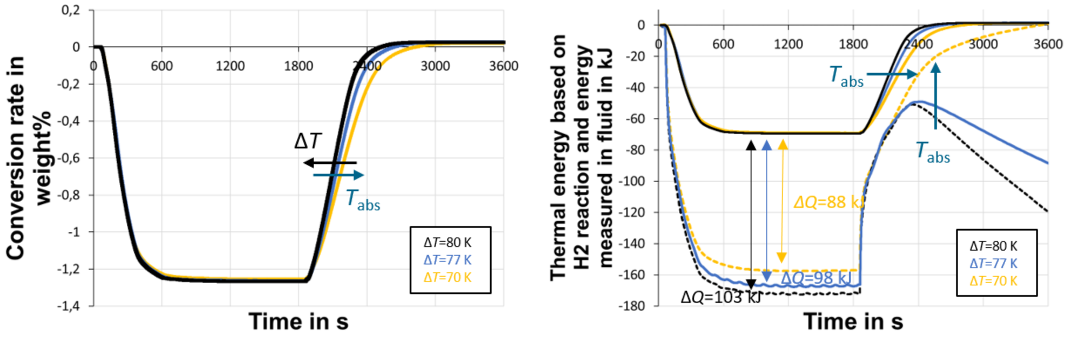

(c) Conversion rate **(d)** Energy: H_2-reaction and fluid

Figure 5.6: Graphs of the direct and indirect parameters for the $p_{des} = 6$ bar, $p_{abs} = 2$ bar and a ratio of 3

Since the desorption conditions are identical to those in subsection 5.1.1, 5.1.2, and 5.1.4, the patterns of the **mass flow** in figure 5.6a are the similar as above. Regarding the absorption behaviour, with decreasing absorption temperature, higher mass flow peaks and an earlier beginning of the fluctuations can be observed. The reason can be explained by the Van't Hoff curve. As for the absorption, the lower the temperature, the further away from the equilibrium curve the set point is located. This results in enhanced dynamics, leading to the observations at hand. This shows that, for constant pressures, the same rules as for constant temperatures in regard to reproducibility apply.

The same patterns for the desorption can be observed in the **temperature** graph in figure 5.6b. During the absorption, the fundamentals explained in subsection 5.1.5 regarding the temperature and distinctiveness of the kink apply. However, in this case the start of the exothermic kink is nearly identical, as the pressure and thus the equilibrium temperature is the same. However, the intensity of it is driven by the distance of the temperature to the equilibrium curve. The greater the distance, the more distinct the kink.

The dynamics of the desorption are identical, resulting in perfectly overlapping graphs in the diagram of the **conversion rate** in figure 5.6c. A slight discrepancy between the maximal conversion rate is observed, the yellow graph with the highest absorption temperature appears to have a lower maximum rate than the other two runs and the slowest dynamics.

In figure 5.6d, the dependency of the **thermal energy** measured in the fluid is observed. The lower the absorption temperature and therefore higher the temperature difference, the higher the required thermal energy input. The change in slope of the graphs occur due to low temperatures during the absorption. Therefore, the losses are the most significant for the dashed black graph with $T_{\text{abs}} = -10$ °C and are reduced for increasing temperatures. The energy from the H_2 reaction remains the same at approximately 69 kJ.

5.2.2 p_{des} = 6 bar and p_{abs} = 3 bar

In the following, the results of the measurements at $p_{\text{des}} = 6$ bar, $p_{\text{abs}} = 3$ bar with the smallest ratio of $\frac{p_{\text{des}}}{p_{\text{abs}}} = 2$, covering temperature differences between the highest ΔT of 90 K, to the lowest ΔT of 50 K, are discussed. The corresponding graphs can be seen in figure 5.7.

In figure 5.7a which depicts the **mass flow**, the impact of the desorption temperature on the dynamics can be observed. Although the runs with $p_{\text{des}} = 6$ bar and $T_{\text{des}} = 70$ °C show the expected patterns, the difference of 10 K, to $T_{\text{des}} = 80$ °C, has an immense impact on the peak height and the dynamics. For the desorption temperature, higher temperatures are preferred for the same reason as the absorption explained in subsection 5.2.2, that is distance to the Van't Hoff equilibrium curve.

In this run, both desorption and absorption temperatures are different. However, in the **temperature** graph in figure 5.7b, identical patterns for the same desorption conditions are observed. For enhanced measurement conditions, the exo- and endothermic kinks are more distinctive and merge with the graphs of the fluid's temperature earlier.

With regard to the **conversion rate** in figure 5.7c, higher dynamics and a higher maximal conversion rate can be observed for an increasing ΔT, as well as for absorption and desorption. The difference between the yellow and the black graph is particularly significant, while the maximal conversion rate is 1.19 % and 1.29 %, respectively.

In the **energy** graph in figure 5.7d, the different amount of required energy input depending on the ΔT, can be seen evidently, differing from 66 kJ for ΔT of 50 K and up

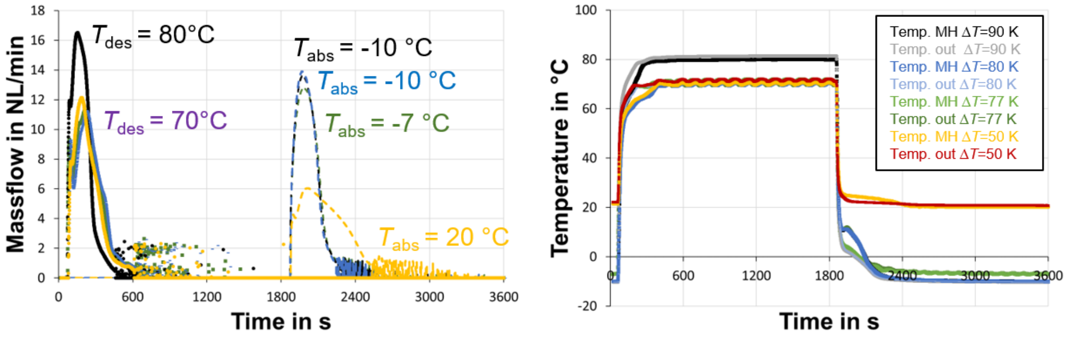

(a) Mass flow **(b)** Temperature

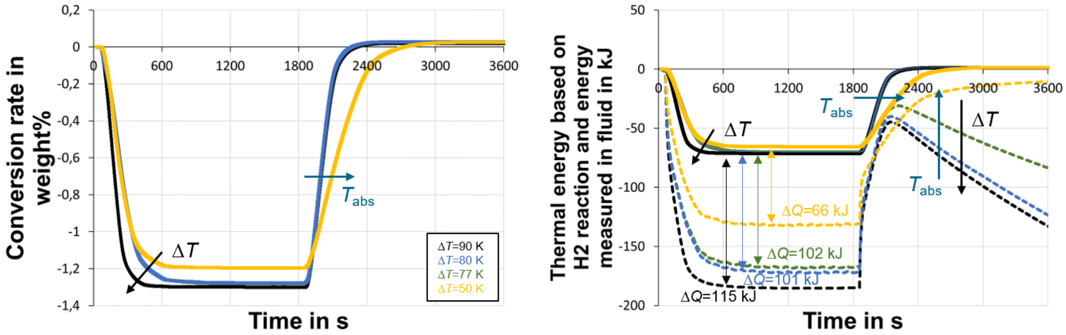

(c) Conversion rate **(d)** Energy: H_2-reaction and fluid

Figure 5.7: Graphs of the direct and indirect parameters for the $p_{des} = 6$ bar, $p_{abs} = 3$ bar and a ratio of 2

to 115 kJ for 90 K

The graphical results of the measurements for $p_{des} = 6$ bar and $p_{abs} = 1.5$ bar are attached to this study in appendix A.3.

5.3 Absorption below 1 bar

Due to technical limitations, it is not feasible with the current setup to reach absorption pressures below 1 bar. However, it is possible that boil-off hydrogen is released below 1 bar. To show that those absorptions are indeed possible, a mass flow controlled run is conducted, and the results are discussed in the following part. The temperature conditions are $T_{des} = 70$ °C, $T_{abs} = -10$ °C with $\Delta T = 80$ K and a desorption pressure of 6 bar. The corresponding graphs are shown in figure 5.8.

For this run, instead of setting mass flow controller MFC11 to a certain absorption pressure, it is adjusted to maintain a desired mass flow of $1 \frac{\text{NL}}{\text{min}}$. As seen in figure 5.8a, the flow is constant throughout the absorption. The absorption pressure of the run is plotted in figure 5.8b, showing evidently that pressures of below 1 bar can be reached. After 1740 s, for the given temperature settings, that pressure is stabilizing at approximately 0.75 bar.

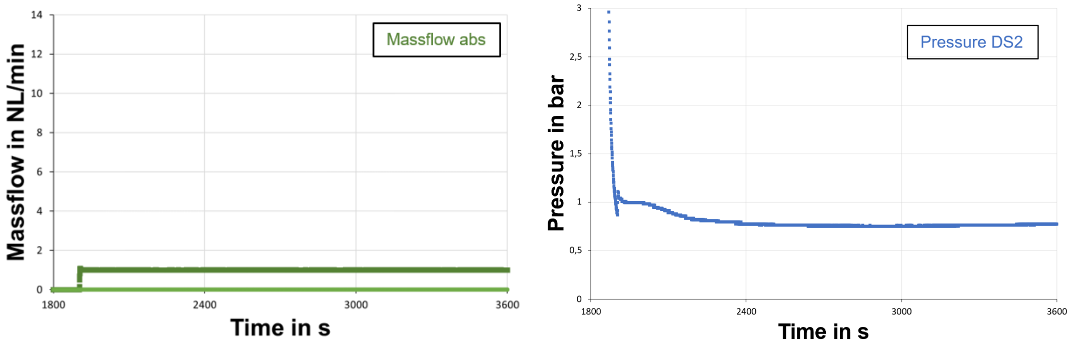

(a) Mass flow

(b) Pressure

Figure 5.8: Graphs of the direct and indirect parameters for a constant mass flow of $1\frac{\text{NL}}{\text{min}}$

In conclusion, absorptions below 1 bar are indeed possible, enabling thermal compressions even from ambient pressure conditions or H_2 uptake from gas mixtures.

5.4 Summary of Experimental Results

This section presents a summary of the experimental results. For certain pressure ratios and temperature differences, distinct boundaries were determined. For $\Delta T = 90$ K a pressure ratio of 6 was achieved. With $\Delta T = 80$ K the pressure ratio was 4, while for $\Delta T = 60$ K it was 3. For $\Delta T = 50$ K the highest pressure ratio established was 2. The desorption at 6 bar requires a minimal desorption temperature of 70 °C. At 60 °C (not presented in the results) the desorption was already too slow. It is possible to reach 8 bar for $T_{\text{des}} = 80$ °C. For the absorption the boundaries are as follows, with $T_{\text{abs}} = -10$ °C a minimum pressure of 1.3 bar was reached, 0 °C was still sufficient for an absorption pressure of 1.5 bar, and 10 °C for 2 bar. For 20 °C a minimum pressure of 2 bar is required. In summary, it can be stated, that absorption dynamics are enhanced with higher pressures and lower temperatures. The same principle applies in reverse for desorptions. Higher temperatures and lower pressures are desirable to ensure optimal dynamics. However, in order to overcome certain pressure ratios, it is necessary to make trade-offs regarding the reaction conditions and the dynamics.

Following the completion of the experiments, it was evident that the material properties of $LaNi_5$ were too high for the given boundary conditions of the LTS application, and additional cooling was required to remove the absorption heat. Moreover, although the reactor was insulated properly, the thermal energy necessary to change the temperature of the system remains quite high. Therefore, for a practical implementation of a MH reactor, the material choice have to be renewed and the design of the reactor has to be adjusted to minimize the required thermal energy to change the system's temperature.

5.5 Balance and Cost

Concluding the results section, a short discussion of the energy balance and the thermal efficiency of the studied metal hydride based H_2 compression is presented. The corresponding graphs are seen in subsection 5.5.1. Moreover, an analysis of cost efficiency and payback time, is presented in subsection 5.5.3.

5.5.1 Energy balance of thermal compression with MH

In this subsection, an analysis of the thermal efficiency of the thermal compression with metal hydrides is given, in comparison to the Lower Heating Value (LHV) of hydrogen. Comparative calculations for the reaction heat based on the MH reaction and the ideal minimum energy required to overcome a certain pressure ratio are done and additionally the real heat required for a measurement with $\Delta T = 70$ K is taken for comparison to determine the fraction of thermal energy required for the reaction.

The calculations for the thermal energy are based on the 0.345 kg $LaNi_5$ MH-system, used during this study, with a desorption enthalpy of 31.61 kJ and a maximum conversion rate of 1.27 % [30]. In figure 5.9 and 5.10 those calculations are visualized graphically.

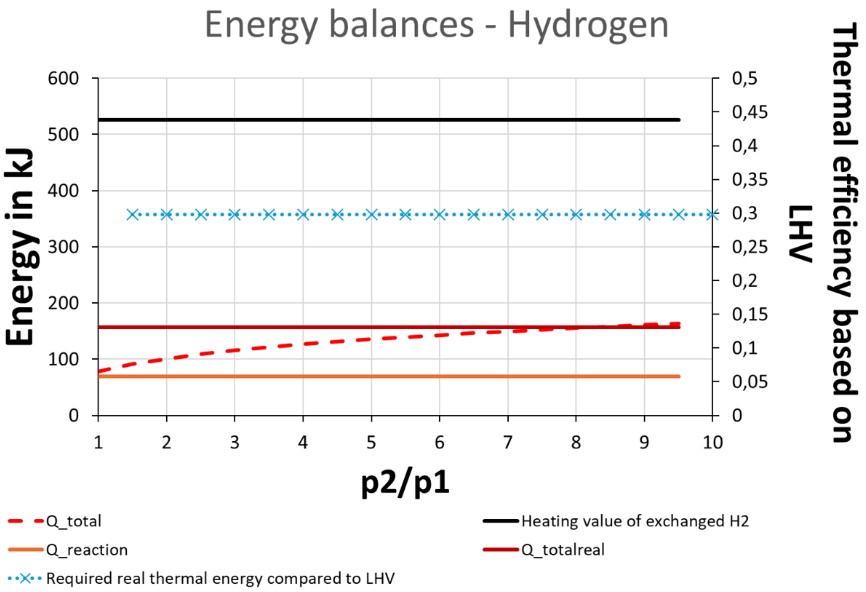

Figure 5.9: Energy balance and thermal efficiency of H_2 based on the lower heating value

Following the experimental results in subsection 5.1 and 5.2, the orange graph shows the heat required for the H_2 desorption. For a hydrogen mass of $m = 0.0043815$ kg the required is 69 kJ. Added to that is the energy required to heat the system by an ideal minimal ΔT_{ideal} that is required to overcome a certain pressure ratio, depicted by the dashed red line. This ΔT_{ideal} can be determined graphically by analysing the Van't Hoff graph: For each absorption and desorption pressure and its corresponding ratio, certain equilibrium temperatures are required to enable the reaction. The distance between these two temperatures is the minimal ΔT_{ideal}. Aligning with the Van't Hoff graph, for higher pressure ratios, a higher temperature, and hence a higher energy input is required. The dark red line shows the summed up total energy required for the reference reaction presented in subsection 4.4.1, where the system is heated by 70 K.

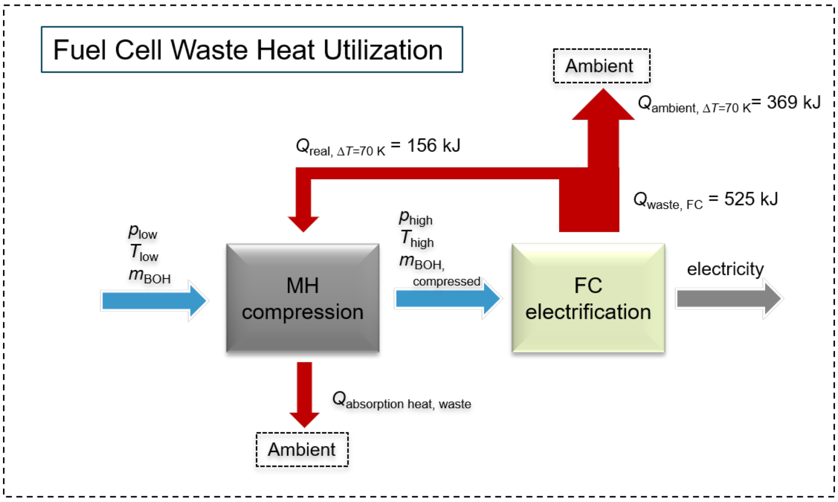

Figure 5.10: Energy balance based on a fuel cell

The thermal efficiency calculations are based on the lower heating value LHV of hydrogen and a fuel cell with an efficiency of 50 %. With an LHV of $120\frac{\text{MJ}}{\text{kg}_{\text{H}_2}}$ the value for the exchanged H_2 mass is 525 kJ, shown by the black line. To calculate the efficiency, the light blue line, the ratio of energy required to the available energy, is determined. For 70 K, that ratio is 30 %. This means that from the amount of energy based on the LHV of hydrogen, only 30 % is required to provide all the necessary thermal energy that is needed for the desorption. This has a great effect on the total energy balance of the potential application of thermal compression with metal hydrides.

5.5.2 Effect of cold H2 compression

When considering thermal compression of BOH with MH, the question arises, how the system would be influenced by the temperature of the incoming hydrogen. Since boil-off hydrogen is most likely to accumulate in liquid hydrogen environments, the temperature of it is supposedly correspondingly low at approximately 20 K. Therefore, primarily, the cold gaseous hydrogen has to be heated up to room temperature. In order to estimate the effect of the cold H_2 on the system performance and functionality, two rough calculations have been done. First, the energy required to heat up the hydrogen that is related to the energy that would be released by the reaction. Second, the maximum temperature decrease in the MH, when cold H_2 is provided to the material without reaction.

The necessary parameter and boundary conditions of the calculations are as followed:

$$\dot{m} = 1\frac{\text{g}}{\text{s}} \qquad M(H) = 1.008\frac{\text{g}}{\text{mol}} \qquad M(H_2) = 2.016\frac{\text{g}}{\text{mol}}$$

$$T_1 = 20.324\ \text{K} \qquad T_2 = 272.96\ \text{K} \qquad \Delta T = 252.639\ \text{K}$$

To determine the energy required to heat hydrogen, equation 5.1 and for the reaction energy equation 5.2 are applied. The ratio x in equation 5.3 gives the fraction of reaction energy required for heating up the gas.

$$\dot{Q}_{\text{heat up}} = \int_{T_1}^{T_2} \dot{m} \cdot c_p(T)dT \tag{5.1}$$

$$\dot{Q}_{\text{reaction}} = \dot{m} \cdot \Delta H \tag{5.2}$$

$$x = \frac{\dot{Q}_{\text{heat up}}}{\dot{Q}_{\text{reaction}}} \tag{5.3}$$

Since the specific heat capacity is dependent on the temperature, $c_p(T)$, as the first step, using MATLAB, the value for c_p is determined. Those calculations are presented in equations 5.5 and 5.4.

$$A = \int_{20.324\ \text{K}}^{272.96\ \text{K}} c_p(T)dT = 6.2982 \cdot 10^3 \frac{\text{J}}{\text{mol}} \tag{5.4}$$

$$c_p = \frac{A}{\Delta T} = \frac{6.2982 \cdot 10^3 \frac{\text{J}}{\text{mol}}}{252.639\ \text{K}} = 24.9\frac{\text{J}}{\text{mol} \cdot\ \text{K}} \tag{5.5}$$

Using equation 5.1, 5.2 and 5.3, $\dot{Q}_{\text{heat up}}$, $\dot{Q}_{\text{reaction}}$ and x are calculated.

$$\begin{aligned}\dot{Q}_{\text{heat up}} &= \dot{m} \cdot c_p \cdot \Delta T \\ &= \frac{1\frac{\text{g}}{\text{s}}}{2.016\frac{\text{g}}{\text{mol}}} \cdot 24.9\frac{\text{J}}{\text{mol} \cdot\ \text{K}} \cdot 252.639\ \text{K} \\ &= 3.120\ \text{kW}\end{aligned} \qquad \begin{aligned}\dot{Q}_{\text{reaction}} &= \dot{m} \cdot \Delta H \\ &= \frac{1\frac{\text{g}}{\text{s}}}{2.016\frac{\text{g}}{\text{mol}}} \cdot 31\frac{\text{kJ}}{\text{mol}} \\ &= 15.377\ \text{kW}\end{aligned}$$

$$x = \frac{\dot{Q}_{\text{heat up}}}{\dot{Q}_{\text{reaction}}} = \frac{3.120\ \text{kW}}{15.377\ \text{kW}} = 20.29\ \%$$

In total, 20.29 % of the reaction energy is required to heat up hydrogen to room temperature. Since the system needs to be cooled during the absorption, this effect could actually help increase the cooling efficiency. However, it needs to be avoided that the MH is too cold to be able to react with hydrogen. In the worst case, the BOH meets the reactor at 20 K, therefore, in the following estimation, the minimum temperature of the MH is determined. The calculations for 1 g_{H_2} and 100 g_{MH} are presented:

$$
\begin{aligned}
-Q_{\text{heat up, H}_2} &= Q_{\text{cool down, MH}} && (5.6)\\
&= m_{\text{MH}} \cdot c_{p_{\text{MH}}} \cdot \Delta T_{\text{MH}} && (5.7)
\end{aligned}
$$

Solving the equation for $\Delta T_{\text{MH, 2}}$ the following equation is derived:

$$
\begin{aligned}
T_{\text{MH,2}} &= -\frac{Q_{\text{heat up, H}_2}}{m_{\text{MH}} \cdot c_{p_{\text{MH}}}} + T_{\text{MH,1}}\\
&= -\frac{3.1241 \text{ kJ}}{100 \text{ g} \cdot 500 \frac{\text{J}}{\text{kg} \cdot \text{K}}} + 273.15 \text{ K}\\
&= 210.67 \text{ K}
\end{aligned}
$$

The metal hydride would be cooled down by 62.48 K to a temperature of 210.67 K. Following this calculation, it could be possible that the cold incoming H_2 cools down the MH to temperatures, where kinetics are influenced. So far, it was only proven that kinetics are not influenced down to temperatures of −40 °C [35]. However, as this is a worst case scenario, less cooling is expected in a real system. Nevertheless, for future system design, the incoming H_2 temperature must be considered for pre-testing and evaluation.

5.5.3 Effect of the cycling time on the system cost

For the cost efficiency of a metal hydride based thermal compressor, first a small analysis based on the MH-mass in the reactor and cycle times is conducted. The cost for a final thermal compressor consists of investment cost for the mass of metal hydride, as well as of payback money for the hydrogen that has been reintegrated into the process. This payback money scales linearly with the hydrogen flow rate. The mass of metal hydride required for a specific flow rate, however, depends on the cycling time, as can be seen in graph 5.11a. Furthermore, as a rough estimation, with increasing mass, investment cost will rise.

As a consequence, one could assume that the system should be operated with short cycle times. However, this is not trivial, as the possible cycle time strongly depends on operating parameters and reactor design. This can be seen in the experiments, where absorption and desorption cycle times can vary from 600 s to more than, 2400 s

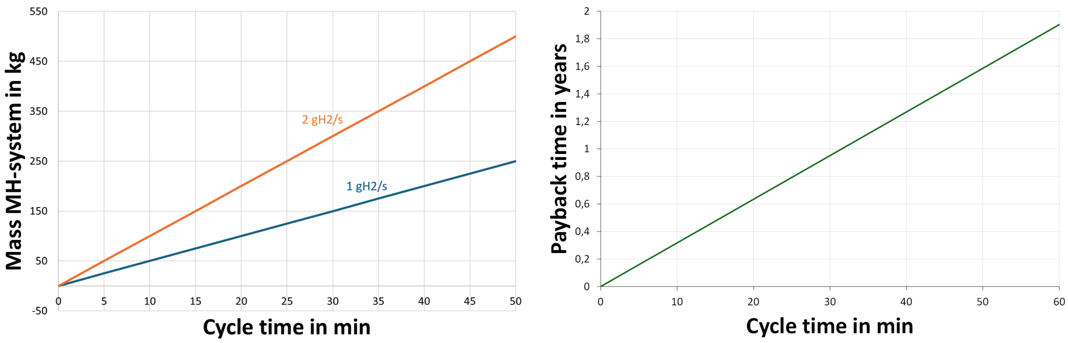

(a) **(b)**

Figure 5.11: Cost efficiency of the MH reactor based on size and cycle times in figure 5.11a and the corresponding payback time in years in figure 5.11b with an estimated cost of the metal hydride and hydrogen of $50\frac{\text{€}}{\text{kg}_{\text{MH}}}$ and $1\frac{\text{€}}{\text{kg}_{\text{H}_2}}$

depending on the ratio. With a different reactor or an enhanced reactor design, shorter cycle times can be achieved.

In conclusion, the cycle time influences the payback time of the reactor, as seen in figure 5.11b. However, since the cycle time itself depends on the reactor design and set parameter, an optimum has to be found.

6 Conclusion and Perspective

The aim of this work was to identify boil-off sources in real life applications to determine potential use cases of a thermal compression using metal hydrides for hydrogen supply at lower pressure conditions.

The three use cases identified for a thermal compression with metal hydrides were a microturbine application, a long-term storage application, and a high pressure storage application, using sLH2. In all identified applications, one or more BOH-sources were found during the process chain. However, for the experimental phase, the LTS application was selected since it appeared to be the most representative and the most suitable for the laboratory-scale-testing.

The LH2 storage tank releases approximately 1 % of BOH per day on a pressure level of $1.5-2$ bar on room temperature of $15-30$ °C. The boil-off is compressed to a pressure of $8-10$ bar, for further utilization in a fuel cell. The waste heat of the fuel cell can be recycled to provide for the desorption and compression process. The temperatures provided from the waste heat are $60-80$ °C. The conditions result in a pressure ratio of $4-6.67$ and an available temperature range of $\Delta T = 30-65$ K.

Following an analysis of Van't Hoff diagrams and the corresponding PCIs of metal-hydrides available at DLR, $LaNi_5$ that was identified to be most suitable for the requirements of the LTS application.

Several experiments with different parameter settings of temperature and pressure were conducted to show the possibilities and boundaries of thermal compression using metal hydrides. The pressure ratios covered were $2-6$ and a temperature ranges $\Delta T = 50-90$ K. The analysis was conducted by comparing the runs with identical temperature differences and pressure ratios.

The dynamics of the reaction strongly depend on the distance of the measured points from the Van't Hoff equilibrium graph, meaning, the further the temperature and pressure from the equilibrium temperature and pressure, the higher the mass flow peaks and therefore the dynamics. For $\Delta T = 90$ K a maximum pressure ratio of 6 was reached and for $\Delta T = 50$ K a ratio of 2 was still possible. The maximal conversion rate that was achieved in this study is $w_{t,\,\mathrm{max}} = 1.29$ %, under boundary conditions of $T_{\mathrm{des}} = 80$ °C, $T_{\mathrm{abs}} = -10$ °C with the highest ΔT of 90 K and a pressure ratio of 2, for $p_{\mathrm{des}} = 6$ bar and $p_{\mathrm{abs}} = 3$ bar. Moreover, to show that absorptions below 1 bar are also possible, an experiment with set incoming hydrogen mass flow was carried out and after some time, pressures below 1 bar were monitored.

From the experiments, characteristic values were derived, which were used for an initial evaluation. For a representative fuel cell with an efficiency of 50 % and the lower heating value of hydrogen of $120\frac{\mathrm{MJ}}{\mathrm{kg}_{\mathrm{H}_2}}$ the amount of thermal energy that can be provided by the waste heat for the compression with the reactor at hand was calculated. It was found, that the waste heat is 525 kJ. For the compression and desorption for a 70 K temperature difference, however, only 156 kJ of heat needs to be provided. This is merely 30 % of the total amount, evidently showing, that the waste heat of a fuel cell can be utilized to fuel the desorption reaction.

For real applications, a more suitable material has to be chosen, since the properties of $LaNi_5$ were too high. In addition to proper insulation, the design of the reactor has to be improved and adjusted to minimize the energy that is necessary to change the heat of the system. Despite place for improvement, it can be concluded that thermal compressions using metal hydrides are a promising option for capturing and upgrading hydrogen boil-off.

Bibliography

[1] Jörg Adolf, Christoph H. Balzer, Jurgen Louis, Uwe Schabla, Manfred Fischedick, Karin Arnold, Andreas Pastowski, and Dietmar Schüwer. Shell hydrogen study energy of the future, 2017.

[2] Bundesministerium für Wirtschaft und Energie. Die nationale wasserstoffstrategie, 2020. URL `https://www.bundesregierung.de/breg-de/suche/die-nationale-wasserstoffstrategie-1759080`.

[3] Gestis - Stoffdatenbank. Wasserstoff, 22.02.2024. URL `https://gestis.dguv.de/data?name=007010`.

[4] Guillaume Petitpas. Boil-off losses along lh2 pathway. Technical Report LLNL-TR-750685, U.S. Department of Energy by Lawrence Livermore National Laboratory, 2018. URL `https://www.osti.gov/biblio/1466121`.

[5] R. Morales-Ospino, A. Celzard, and V. Fierro. Strategies to recover and minimize boil-off losses during liquid hydrogen storage. *Renewable and Sustainable Energy Reviews*, 182:113360, 2023. ISSN 1364-0321. doi: https://doi.org/10.1016/j.rser.2023.113360. URL `https://www.sciencedirect.com/science/article/pii/S1364032123002174`.

[6] M. J. Rosso and P. M. Golben. Capture of liquid hydrogen boil-off with metal hydride absorbers. *Journal of the Less Common Metals*, 131(1-2):283–292, 1987. ISSN 00225088. doi: 10.1016/0022-5088(87)90527-3.

[7] T. Fuura, S. Tsunokake, R. Hirotani, T. Hishimoto, M. Akai, S. Watanabe, H. Enoki, and E. Akiba. Development of a lh2 vehicle tank boil-off gas recovery system using hydrogen storage alloys. In *YDROGEN, 15th World Hydrogen Energy Conference*, 2004.

[8] E. L. Huston and G. D. Sandrock. Engineering properties of metal hydrides. *Journal of the Less Common Metals*, 74(2):435–443, 1980. ISSN 00225088. doi: 10.1016/0022-5088(80)90182-4.

[9] Tongtong Zhang, Joao Uratani, Yixuan Huang, Lejin Xu, Steve Griffiths, and Yulong Ding. Hydrogen liquefaction and storage: Recent progress and perspectives. *Renewable and Sustainable Energy Reviews*, 176:113204, 2023. ISSN 1364-0321. doi: https://doi.org/10.1016/j.rser.2023.113204. URL `https://www.sciencedirect.com/science/article/pii/S1364032123000606`.

[10] S.A. Sherif, N. Zeytinoglu, and T.N. Veziroğlu. Liquid hydrogen: Potential, problems, and a proposed research program. *International Journal of Hydrogen Energy*, 22(7):683–688, 1997. ISSN 0360-3199. doi: https://doi.org/10.1016/S0360-3199(96)00201-7. URL `https://www.sciencedirect.com/science/article/pii/S0360319996002017`.

[11] Jonathan K. Partridge. Fractional consumption of liquid hydrogen and liquid oxygen during the space shuttle program. *AIP Conference Proceedings*, 1434(1): 1765–1770, 06 2012. ISSN 0094-243X. doi: 10.1063/1.4707112. URL `https://doi.org/10.1063/1.4707112`.

[12] James E. Fesmire and Adam Swanger. Overview of the new lh2 sphere at nasa kennedy space center. In *DOE/NASA Advances in Liquid Hydrogen Storage Workshop*, August 2021. Online workshop.

[13] Lutz Decker. Linde, liquid hydrogen distribution technology. In *HYPER closing seminar*, December 2019. Accessed: 30.10.2024.

[14] W Notardonato, Adam Swanger, James Fesmire, K Jumper, W Johnson, and T Tomsik. Zero boil-off methods for large-scale liquid hydrogen tanks using integrated refrigeration and storage. *IOP Conference Series: Materials Science and Engineering*, 278:012012, 12 2017. doi: 10.1088/1757-899X/278/1/012012.

[15] Gary Sandrock. A panoramic overview of hydrogen storage alloys from a gas reaction point of view. *Journal of Alloys and Compounds*, 293-295:877–888, 1999. ISSN 0925-8388. doi: https://doi.org/10.1016/S0925-8388(99)00384-9. URL `https://www.sciencedirect.com/science/article/pii/S0925838899003849`.

[16] H. Buchner. *Energiespeicherung in Metallhydriden.* Innovative Energietechnik. Springer Wien, Wien, 2013. ISBN 9783709186725.

[17] Qiwen Lai, Mark Paskevicius, Drew A. Sheppard, Craig E. Buckley, Aaron W. Thornton, Matthew R. Hill, Qinfen Gu, Jianfeng Mao, Zhenguo Huang, Hua Kun Liu, Zaiping Guo, Amitava Banerjee, Sudip Chakraborty, Rajeev Ahuja, and Kondo-Francois Aguey-Zinsou. Hydrogen storage materials for mobile and stationary applications: Current state of the art. *ChemSusChem*, 8(17):2789–2825, 2015. doi: https://doi.org/10.1002/cssc.201500231. URL `https://chemistry-europe.onlinelibrary.wiley.com/doi/abs/10.1002/cssc.201500231`.

[18] Poojan Modi and Kondo-Francois Aguey-Zinsou. Room temperature metal hydrides for stationary and heat storage applications: A review. *Frontiers in Energy Research*, 9, 2021. doi: 10.3389/fenrg.2021.616115.

[19] M. V. Lototskyy, V. A. Yartys, B. G. Pollet, and R. C. Bowman. Metal hydride hydrogen compressors: A review. *International Journal of Hydrogen Energy*, 39 (11):5818–5851, 2014. ISSN 03603199. doi: 10.1016/j.ijhydene.2014.01.158.

[20] Ted B. Flanagan and J.D. Clewley. Hysteresis in metal hydrides. *Journal of the Less Common Metals*, 83(1):127–141, 1982. ISSN 0022-5088. doi: https://doi.org/10.1016/0022-5088(82)90176-X. URL https://www.sciencedirect.com/science/article/pii/002250888290176X.

[21] R Balasubramaniam. Hysteresis in metal–hydrogen systems. *Journal of Alloys and Compounds*, 253-254:203–206, 1997. ISSN 0925-8388. doi: https://doi.org/10.1016/S0925-8388(96)02894-0. URL https://www.sciencedirect.com/science/article/pii/S0925838896028940.

[22] Mila Kölbig. *Coupled metal hydride reactions for preheating vehicle components at low temperatures*. Dissertation, Universität Stuttgart, Stuttgart, 2018.

[23] T. Nishizaki, K. Miyamoto, and K. Yoshida. Coefficients of performance of hydride heat pumps. *Journal of the Less Common Metals*, 89(2):559–566, 1983. ISSN 00225088. doi: 10.1016/0022-5088(83)90372-7.

[24] Zhuoya Peng, Quan Li, Liuzhang Ouyang, Wenbin Jiang, Kang Chen, Hui Wang, Jiangwen Liu, Zhinian Li, Shumao Wang, and Min Zhu. Overview of hydrogen compression materials based on a three-stage metal hydride hydrogen compressor. *Journal of Alloys and Compounds*, 895:162465, 2022. ISSN 0925-8388. doi: https://doi.org/10.1016/j.jallcom.2021.162465. URL https://www.sciencedirect.com/science/article/pii/S0925838821038755.

[25] DLR. Balis: Emissionsfrei fliegen, 2023. URL https://www.dlr.de/de/tt/forschung-transfer/projekte/abgeschlossene-projekte/2023/balis.

[26] Simon Dr. Schäfer and Daniel Duschek. Key features of fuel connectors and fuelling protocols for cryo-compressed and liquid hydrogen. Presentation, CEP - Clean Energy Partnership, December 2021.

[27] Daimer Truck. Sicher, schnell und einfach: Daimler truck und linde setzen mit slh2-technologie neuen standard für flüssigwasserstoff-betankung. https://www.daimlertruck.com/newsroom/pressemitteilung/sicher-schnell-und-einfach-daimler-truck-und-linde-setzen-mit-slh2-technolo
2024. Online; accessed 17.10.2024.

[28] Enrico Pizzutilo, Thomas Acher, Benjamin Reuter, Christian Will, and Simon Schäfer. Subcooled liquid hydrogen technology for heavy-duty trucks. *World Electric Vehicle Journal*, 15:22, 01 2024. doi: 10.3390/wevj15010022.

[29] Daniel Koller. Thermodynamische charakterisierung und modellierung thermodynamische charakterisierung und modellierung von metallhydriden für die fahrzeugklimatisierung. Masterarbeit, Universität Stuttgart, Stuttgart, 31.08.2018.

[30] Eike Willers. *Multi-Hydrid-Sorptionsanlage zur kombinierten Heizung und Kühlung*. Dissertation, Universität Stuttgart, Stuttgart, 22.03.2022.

[31] Mario Bedrunka, Nils Bornemann, Gerd Steinebach, and Dirk Reith. Reaction behavior modeling of metal hydride based on fetimn using numerical simulations. Preprint submitted to Journal of Elsevier, 01 2021.

[32] Christoph Weckerle. *A metal hydride air-conditioning system for fuel cell vehicles*. Dissertation, Stuttgart, Stuttgart, 2020.

[33] Kai Herbrig, Lars Röntzsch, Carsten Pohlmann, Thomas Weißgärber, and Bernd Kieback. Hydrogen storage systems based on hydride–graphite composites: computer simulation and experimental validation. *International Journal of Hydrogen Energy*, 38(17):7026–7036, 2013. ISSN 03603199. doi: 10.1016/j.ijhydene.2013.03.104.

[34] Carolin Kretschmer. Entwicklung von metallhydrid-reaktoren mittels 3d-druck und charakterisierung dieser für die anwendung als vorheizer in einem brennstoffzellenbetriebenem lastenfahrrad. Masterarbeit, Universität Stuttgart, 05 2019.

[35] Alina Keller. Untersuchung und bewertung eines metallhydrid-basierten vorheizers für den kaltstart ab -40 °c in der luftfahrtanwendung. Master's thesis, Universität Stuttgart, 2023. URL `https://elib.dlr.de/195043/`.

[36] Gernot Krakat. *D4.2 Thermophysikalische Stoffwerte von Fluiden für Kältebäder, von wässrige Lösungen und Glykolen*, pages 531–549. Springer Berlin Heidelberg, Berlin, Heidelberg, 2019. ISBN 978-3-662-52989-8. doi: 10.1007/978-3-662-52989-8_23. URL `https://doi.org/10.1007/978-3-662-52989-8_23`.

[37] Manfred Klell. *Storage of Hydrogen in the Pure Form*, chapter 1, pages 1–37. John Wiley I& Sons, Ltd, 2010. ISBN 9783527629800. doi: https://doi.org/10.1002/9783527629800.ch1. URL `https://onlinelibrary.wiley.com/doi/abs/10.1002/9783527629800.ch1`.

[38] Linde plc. Extending the reach of the hydrogen value chain. `https://assets.linde.com/-/media/global/engineering/engineering/home/products-and-services/plant-components/le_lh2_technologies_brochure_rz_view_51906.pdf`, 2021. Accessed: 09.11.2024.

Appendix

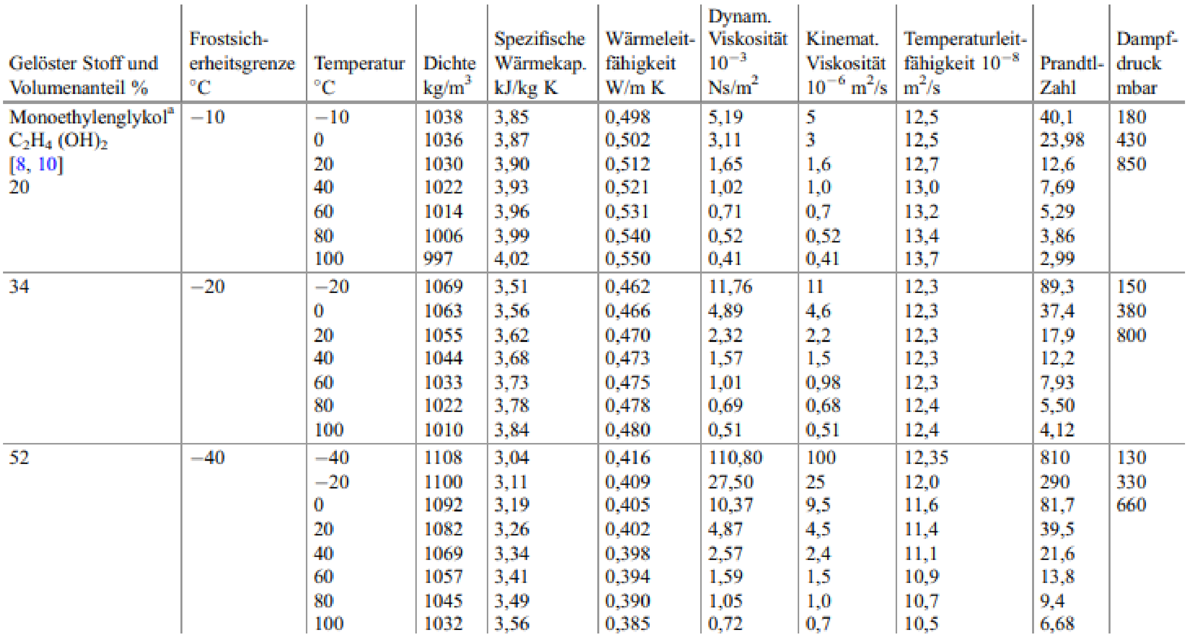

Gelöster Stoff und Volumenanteil %	Frostsicherheitsgrenze °C	Temperatur °C	Dichte kg/m^3	Spezifische Wärmekap. kJ/kg K	Wärmeleitfähigkeit W/m K	Dynam. Viskosität 10^{-3} Ns/m^2	Kinemat. Viskosität 10^{-6} m^2/s	Temperaturleitfähigkeit 10^{-8} m^2/s	Prandtl-Zahl	Dampfdruck mbar
Monoethylenglykol[a] $C_2H_4\,(OH)_2$ [8, 10] 20	−10	−10	1038	3,85	0,498	5,19	5	12,5	40,1	180
		0	1036	3,87	0,502	3,11	3	12,5	23,98	430
		20	1030	3,90	0,512	1,65	1,6	12,7	12,6	850
		40	1022	3,93	0,521	1,02	1,0	13,0	7,69	
		60	1014	3,96	0,531	0,71	0,7	13,2	5,29	
		80	1006	3,99	0,540	0,52	0,52	13,4	3,86	
		100	997	4,02	0,550	0,41	0,41	13,7	2,99	
34	−20	−20	1069	3,51	0,462	11,76	11	12,3	89,3	150
		0	1063	3,56	0,466	4,89	4,6	12,3	37,4	380
		20	1055	3,62	0,470	2,32	2,2	12,3	17,9	800
		40	1044	3,68	0,473	1,57	1,5	12,3	12,2	
		60	1033	3,73	0,475	1,01	0,98	12,3	7,93	
		80	1022	3,78	0,478	0,69	0,68	12,4	5,50	
		100	1010	3,84	0,480	0,51	0,51	12,4	4,12	
52	−40	−40	1108	3,04	0,416	110,80	100	12,35	810	130
		−20	1100	3,11	0,409	27,50	25	12,0	290	330
		0	1092	3,19	0,405	10,37	9,5	11,6	81,7	660
		20	1082	3,26	0,402	4,87	4,5	11,4	39,5	
		40	1069	3,34	0,398	2,57	2,4	11,1	21,6	
		60	1057	3,41	0,394	1,59	1,5	10,9	13,8	
		80	1045	3,49	0,390	1,05	1,0	10,7	9,4	
		100	1032	3,56	0,385	0,72	0,7	10,5	6,68	

Figure A.1: VDI Heat Atlas information about mono-ethylene glycol [36]

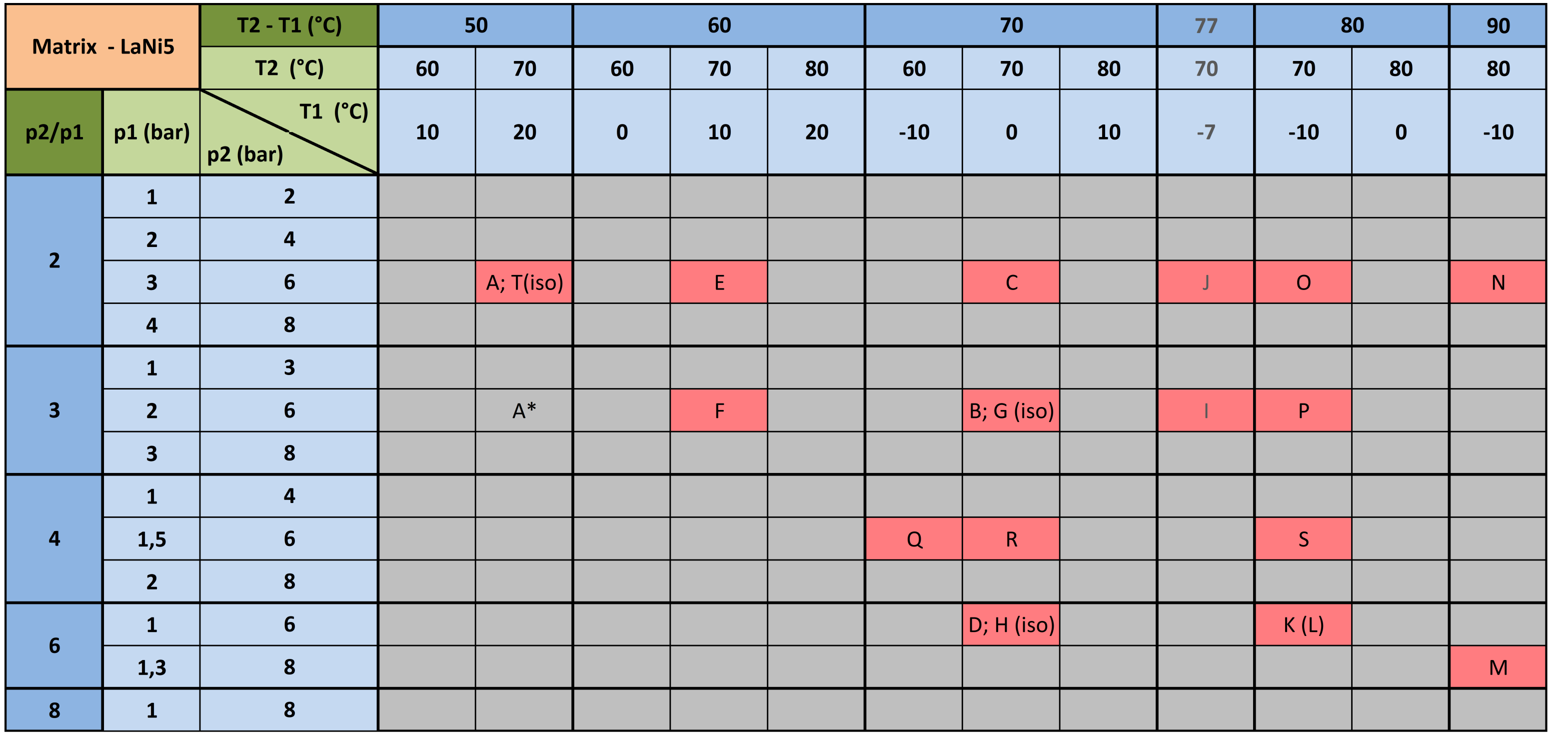

Matrix - LaNi5		T2 - T1 (°C)	50		60			70			77	80		90
		T2 (°C)	60	70	60	70	80	60	70	80	70	70	80	80
p2/p1	p1 (bar)	T1 (°C) p2 (bar)	10	20	0	10	20	-10	0	10	-7	-10	0	-10
2	1	2												
	2	4												
	3	6		A; T(iso)		E			C		J	O		N
	4	8												
3	1	3												
	2	6		A*		F			B; G (iso)		I	P		
	3	8												
4	1	4												
	1,5	6						Q	R			S		
	2	8												
6	1	6							D; H (iso)			K (L)		
	1,3	8												M
8	1	8												

Figure A.2: Design of Experiments: Matrix

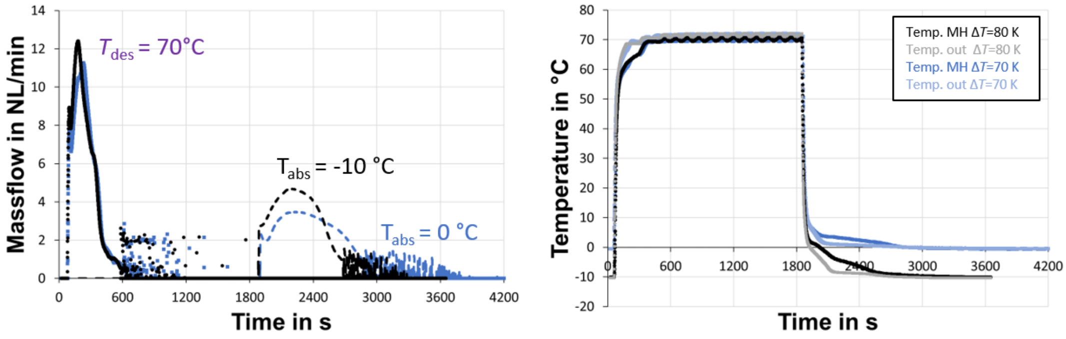

(a) Mass flow **(b)** Temperature

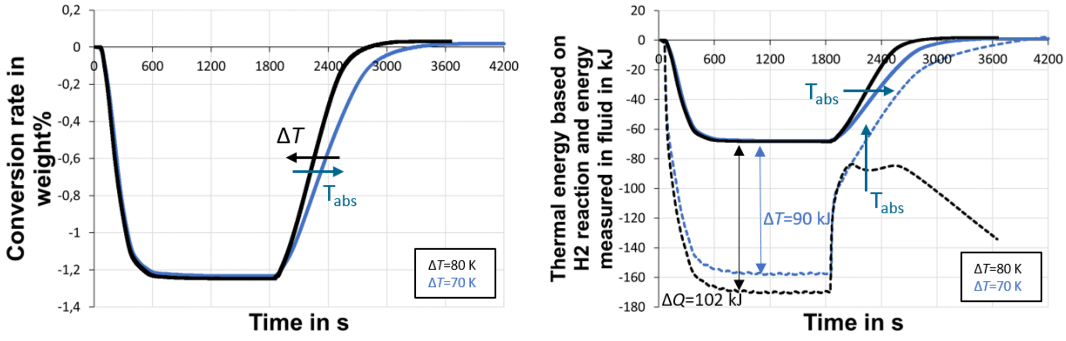

(c) Conversion rate **(d)** Energy: H_2-reaction and fluid

Figure A.3: Graphs of the direct and indirect parameter for the $p_{\mathrm{des}} = 6$ bar and $p_{\mathrm{abs}} = 1.5$ bar and a ratio of 4

Table A.1: Reported hydrogen Boil-off of several storage applications

Source	Tank size in m^3	Tank form	BOH rate in kg/day	BOH rate in %/day	Mitigation Measurments	Affiliation	Notes
[5]	3200	spherical	563	0.25	inner and outer sphere	NASA, KSC	
[5]	540-640	spherical		< 0.2	Inner and outer wall; Double hulled tank; vacuum interspace		
[5]	total vol: 11,200; storage capacity: 10,000			$<= 0.1$			
[5]	1250; 116 m long; 8000 t	cylindrical			single-stage turbo compressor to ensure liquid form; double jacketed; vacuum-insulated	Kawasaki Heavy Industries	in-situ liquefaction; marine tank
[5]	50	spherical		0.3-0.5	vacuum, insulated, double walled dewars		
[5]	103	spherical		0.2	vacuum, insulated, double walled dewars		
[5]	19000	spherical		0.06	vacuum, insulated, double walled dewars		
[5]	300	cylindrical		< 0.3		LINDE	
[5]	1100–2300	spherical		< 0.1		LINDE	
[37]	17600 l = 17.6 m^3; storage capacity 1000 kg		0.5 kg/h = 12 kg/d	1-1.2			HyCentA Research GmbH, Graz
[13]	71 ; storage capacity 4600 kg	cylindrical	< 44	< 0.95	vacuum-perlite insulation; cryogenic valves	LINDE	Typical industrial applications; high H_2 demand
[13]	11.5 ; storage capacity: 900 kg	cylindrical	< 5.5	< 0.6	cryogenic valves; multi layer insulation in vacuum space	LINDE	Fueling stations; low to medium H_2 demand
[13]	6; storage capacity 400 kg	cylindrical	< 2	< 0.5	cryogenic valves; insulation material in vacuum space	LINDE	fueling stations; low H_2 demand
[13]	300 (storage capacity: 19.3 t)	cylindrical	< 58	< 0.3		LINDE	larger capacities for bulk storage
[13]	1100-2300 (storage capacity: 70.2-145 t)	spherical	< 70–145	< 0.1		LINDE	larger capacities for bulk storage
[13]	capacity: 50 kg/h; bulk storage capacity: 400 kg	cylindrical	< 4	1		LINDE	liquid hydrogen fueling station; type CP90
[38]	capacity up to 26 t_{H_2}	cylindrical		0.25–0.95	vacuum insulation with perlite, super insulation or gas bubbles	LINDE	storage application
[12]	4732 (ullage volume $> 10\%$)	spherical	0.048		passive: glass bubbles thermal insulation system (evacuated); active: integrated refrigeration and storage (IRAS) heat exchanger	NASA	no venting of boil of gas; bubbles -> 50% less BOH
[11]	3,220,000 l + 230,00 l ullage	spherical	1200 l/d		double walled tanks insulated with perlite in a vacuum	NASA, KSC	evaporation loss 12% of total loss in 30 years span; LC-39A
[11]	3,220,000 l +230,00 l ullage	spherical	2700 l/d		double walled tanks insulated with perlite in a vacuum	NASA, KSC	LC-39B